Novel Approaches in Quantum Chemistry:
Self-Consistent Density-Functional Embedding and Polaritonic Coupled-Cluster Theory

Dissertation

zur Erlangung des Doktorgrades
an der Fakultät für Mathematik, Informatik und Naturwissenschaften
Fachbereich Physik der Universität Hamburg

vorgelegt von

Uliana Mordovina

Hamburg
2020

Gutachter*innen der Dissertation:	Prof. Dr. Angel Rubio Prof. Dr. Daniela Pfannkuche
Zusammensetzung der Prüfungskommission:	Dr. Heiko Appel Prof. Dr. Arwen Pearson Prof. Dr. Daniela Pfannkuche Prof. Dr. Angel Rubio Prof. Dr. Michael Thorwart
Vorsitzende der Prüfungskommission:	Prof. Dr. Arwen Pearson
Datum der Disputation:	27.04.2020
Vorsitzender Fach-Promotionsausschusses PHYSIK:	Prof. Dr. Günter Hans Walter Sigl
Leiter des Fachbereichs PHYSIK:	Prof. Dr. Wolfgang Hansen
Dekan der Fakultät MIN:	Prof. Dr. Heinrich Graener

Zusammenfassung

Die durch Korrelationen entstehenden Feinheiten in der Elektronenstruktur von Molekülen sind weitgehend für das Auftreten vieler chemischer Phänomene verantwortlich. Werden diese Korrelationen stark, resultieren daraus wichtige Mechanismen wie das Aufbrechen molekularer Bindungen oder Ladungsmigration. Diese Effekte korrekt zu beschreiben fällt oft sogar den er- folgreichsten theoretischen Methoden wie der Dichtefunktionaltheorie schwer. Dies liegt oft an der Art der verwendeten Approximationen, was die Entwicklungen neuartiger Herangehensweisen erforderlich macht. Des Weiteren zeigen jüngste Experimente im Bereich der quantenelektrodynamischen Chemie eindrucksvoll, dass wichtige Mechanismen wie die zuvor genannten durch den Einsatz photonischer Umgebungen stark modifiziert werden können, was ein weites Feld für neue Anwendungen eröffnet. Theoretische Werkzeuge, die solche Situationen basierend ausschließlich auf grundlegenden physikalischen Prinzipien beschreiben können, kommen erst jetzt auf den Markt.

Für die erste der genannten Herausforderungen, wird eine selbstkonsistente Dichtefunktional-Embedding-Methode entwickelt, die von den üblichen Approximationen des Energiefunktionals absieht und stattdessen direkt die exakte Dichte-Potenzial-Abbildung der Dichtefunktionaltheorie. Inspiriert durch die Density-Matrix Embedding Theory, wird das zu untersuchende Gesamtsystem auf einen Satz von Fragmenten projiziert, welche dann sehr präzise beschrieben werden können. Durch stetiges Zusammenführen der Einzelergebnisse wird das Kohn-Sham Potenzial des Gesamtsystems aktualisiert, welches dann wiederum zu Konstruktion besserer Projektionen für die Fragmente verwendet wird. Die Methode wird anhand einfacher Zwei-Elektron-Modellsysteme getestet, die jedoch für übliche Dichtefunktional- Approximationen herausfordernd sind. Dabei liefert die entwickelte Embeddingstrategie präzise Ergebnisse. Unter anderem werden Signaturen starker Korrelationen, die in anderen Methoden fehlen, hier mit bemerkenswerter Genauigkeit reproduziert. Daher bietet das vorgestellte Konzept einen vielversprechenden Ansatz für die Funktionalentwicklung in der Dichtefunktionaltheorie und ihren Erweiterungen, wie der quantenelektrodynamischen Dichtefunktionaltheorie.

Als vielversprechendes Instrument für polaritonische Chemie wird eine Coupled-Cluster Theorie für stark gekoppelte Elektron-Photon Systeme konzipiert. Mit der entwickelten Methode werden unter anderem Absorptionsspektren von Modellmolekülen in optischen Resonatoren berechnet und mit numerisch exakten Ergebnissen verglichen. Dabei werden alle wesentlichen Merkmale der Referenzspektren für alle ausgewählten Kopplungsstärken mit der erweiterten Coupled-Cluster Theorie reproduziert, einschließlich der Rabi-Aufspaltungen der Absorptionspeaks und der Multiphoton-Prozesse, wobei Letztere bisher mit keiner anderen Ab-initio-Methode gezeigt wurden. Dies eröffnet Anwendungsperspektiven, die sowohl über die der Quantenoptik hinausgehen, da nun die Elektronenstruktur explizit miteinbezogen wird, als auch über die der vorhandenen Ab-initio-Methoden. Die vorgestellte konzeptionelle Erweiterung der Coupled-Cluster Theorie hat das Potential einfach in bestehende quantenchemische Computerprogramme integriert zu werden um damit Experimenten auf dem Gebiet der polaritonischen Chemie zu interpretieren und präzise zu modellieren.

Abstract

Subtleties in molecular electronic structure that arise from electronic correlations dictate most of chemistry. Important processes such as molecular bond breaking or charge migration are direct consequences of these correlations becoming dominant. Even the most successful theoretical approaches, such as density functional theory, however, still often struggle to describe these effects due to the nature of employed approximations and therefore require additional developments. Moreover, recent experiments in the field of quantum electrodynamical chemistry show that important chemical mechanisms such as those described above can be drastically modified by using photonic environments, which opens a whole new field of possible applications. Theoretical tools that address these situations from first principles are only now being developed.

To address the first of the outlined challenges, we present a novel self-consistent density-functional embedding technique, which directly targets at approximating the density-potential mapping of exact density functional theory and therefore leaves the realm of standard energy-functional approximations. Inspired by the density-matrix embedding theory, we project the full system onto a set of small interacting fragments that can be solved accurately. Based on the rigorous relation of density and potential in density functional theory, we then invert the fragment densities to local potentials. Combining these results in a continuous manner provides an update for the Kohn-Sham potential of the full system, which is then used to update the projection. We benchmark our approach for notoriously difficult examples of molecular bond stretching in one and two dimensions and show that in these cases the scheme provides accurate approximations for densities and the Kohn-Sham potentials. We demonstrate that signatures of strong correlations present in the exact exchange-correlation potential, even those that so far have been missing in all approximate approaches, are reproduced by our method with remarkable accuracy. Therefore, the methods provides a promising new path for functional development in density functional theory and its extensions, such as quantum electrodynamical density functional theory.

To provide a theoretical tool for quantum electrodynamical (or polaritonic) chemistry, we develop a coupled-cluster theory for systems of electrons strongly coupled to photons. We show benchmark results for ground and excited state properties of a model molecule in high-Q optical cavities. By comparing to full configuration interaction results, we demonstrate that our method quantitatively captures all key features present in the exact reference, including Rabi splittings and multi-photon processes in all considered coupling regimes. Therefore, not only does our method go beyond standard quantum optical approaches, since it includes an accurate treatment of electronic structure, it also goes beyond existing *ab intio* methods in terms of accuracy. A clear path on how to incorporate the developed extension of coupled-cluster theory into existing quantum chemistry programs is provided, paving the way for high-accuracy modeling and interpretation of experiments in the field of polaritonic chemistry with a perspective of application to all types of fermion-boson coupled systems.

List of publications

Results of my research as a PhD candidate have been published prior to this thesis. Following research papers are part of this thesis:

- U. Mordovina, T. E. Reinhard, I. Theophilou, H. Appel, and A. Rubio, *Self-Consistent Density-Functional Embedding: a Novel Approach for Density-Functional Approximations*, J. Chem. Theory Comput. **15**, 5209 (2019),
- U. Mordovina, C. Bungey, H. Appel, P. J. Knowles, A. Rubio, and F. R. Manby, *Polaritonic Coupled-Cluster Theory*, arXiv:1909.02401 (2019), submitted to Phys. Rev. Research.

Following publication is not part of this thesis:

- T. E. Reinhard, U. Mordovina, C. Hubig, J. S. Kretchmer, U. Schollwöck, H. Appel, M. A. Sentef, and A. Rubio, *Density-Matrix Embedding Theory Study of the One-Dimensional Hubbard-Holstein Model*, J. Chem. Theory Comput. **15**, 2221 (2019).

Contents

1 Introduction

"Chemistry is dead. Long live chemistry!" – P. M. A. Dirac[1]

With the formulation of the Schrödinger equation and its successful application to the hydrogen atom [2] and the hydrogen molecule [3], *Quantum Chemistry* was born. This field focuses on applying principles of quantum mechanics to describe the behavior of atomic, molecular, or even solid state systems. Given the fact that underlying equations can (almost) never be solved exactly, approximate mathematical and computational tools have to be developed. Following Pople [4], these tools ideally should assist the interpretation of observed phenomena on the one hand and predict outcomes of new experiments on the other hand. In this spirit, reliable predictive modeling is vital for the design of novel compounds, the optimization of chemical processes, or even the discovery of new physical phenomena.

On the journey towards predictive modeling, an extensive toolbox was developed over the past decades [5], with methods varying in range of applicability, accuracy, and computational cost. These span from the almost exact full configuration interaction (FCI) calculations for diatomic molecules [6] to combined quantum-mechanics/molecular-mechanics (QM/MM) approaches for enzymatic reactions in biological systems [7]. And, in order to cover an increasing range of applications, this toolbox is constantly extended and improved.

We can identify two fundamental types of challenges that drive method development in quantum chemistry: first being posed by the limitations of established theoretical methods and second resulting from experimental insights, both exemplified in the following.

New approach within an established method

Over the past decades, Density Functional Theory (DFT) has become a very successful method able to accurately describe molecular and condensed matter systems. The theory is based on an exact reformulation of the electronic Schrödinger equation, where all observables become unique functionals of the low-dimensional electronic density [8] instead of the high-dimensional electronic wave function. DFT is usually employed in its Kohn-Sham version, where the density of the targeted interacting system is calculated via an auxiliary non-interacting system [9], making the method very computationally efficient. All interactions and correlations present in the system are mimicked by the so-called exchange-correlation (xc) potential which is usually determined as the derivative of the xc energy functional $E_{\mathrm{xc}}[n]$. This functional is unknown and has to be approximated in practice [9–11]. Hence, method development in DFT usually boils down to construction of new functionals.

The approximate character of $E_{\mathrm{xc}}[n]$ is both blessing and curse of DFT. For instance, the theory is often believed to be incapable of describing strong electronic correlation, a drawback that is indeed not intrinsic to the theory itself, but caused solely by the currently employed approximations to the exact energy functional. Additionally, a recent study showed that modern functionals that produce better energies do not automatically serve as better approximations to the exact functional [12], encouraging the quest for radically new strategies within the DFT framework [13].

[1] paraphrased from [1]

Methods that explicitly target electronic correlations can provide strategies for novel developments within the DFT framework. For small systems, correlations are considered by directly targeting the wave function by means of e.g. FCI [14], coupled-cluster theory [15], or density-matrix renormalization group (DMRG) [16]. A strategy for using these insights on a larger scale is provided by embedding theories, such as dynamical-mean-field theory (DMFT) [17–19] and density-matrix-embedding theory (DMET) [20–22]. These approaches that combine accurate calculations of parts of a system with computationally cheap treatment of the rest.

In part II of this thesis, we propose a DMET-inspired density-functional embedding approach that does not construct yet another approximate energy functional but targets directly the mapping between the electronic density and the Kohn-Sham potential. We also do not derive an explicit expression of this potential but rather employ a direct numerical construction based on local approximations to the density-potential mapping that are obtained from interacting fragment wave functions.

Established method addressing new challenges

Driven by experimental progress in the design and control of nanostructures, an exciting field of applications has emerged at the interface between quantum optics, quantum chemistry and material sciences. Through the collective coupling of many emitters to a cavity mode [23] or by placing single molecules in plasmonic nanostructures [24], the interaction strength between light and matter can be increased to a hundredfold or more of its free-space analog, the fine structure constant $\alpha \approx 1/137$. Hybrid light-matter states, called *polaritons*, emerging as a consequence of this strong light-matter coupling can substantially change chemical and physical properties of molecular systems [25–28], examples being altered chemical reactions [29, 30] or modifications of intersystem crossings [31].

Understanding these polariton-mediated phenomena requires theoretical approaches, where both, light and matter, are treated on an equal quantum mechanical footing [32–34]. An extension of existing quantum chemical methods to include photons provides a natural route in this direction, on which several electronic structure methods embarked in the recent years [35–45]. Surprisingly, one of the most accurate and reliable methods available in quantum chemistry, the coupled-cluster (CC) theory, is so far not among the aforementioned methods. In part III of this thesis, we are aiming on closing this gap.

CC theory is based on an *ansatz* for the electronic wave function that allows for an approximate incorporation of all electronic configurations arising from a given mean-field reference state into the ground state. That the requirements for a computationally tractable CC theory can be met also for bosonic degrees of freedom was demonstrated by its application to molecular vibrations [46]. Through fermionization of bosonic excitations we are able to extend the theoretical framework of CC theory such that coupled electron-photon systems can be addressed. We illustrate the potential of such an approach to describe the behavior of polaritonic molecular systems with a computational cost that scales polynomially in system size.

Physical sciences are at their heart experimental disciplines, meaning that a theory is not worth much if it is not verified by an experiment. Same applies to every approximate method developed within an established theory: in the end, its predictions have to be checked against experimental findings.

However, it can take an enormous amount of effort either to implement a new method efficiently so that it can simulate an experiment, or to design and perform an experiment that in principle can exhibit the theoretically proposed features. Instead, we provide a simple proof of concept for both introduced approaches by testing them against more accurate theoretical methods, serving as an intermediate step towards their final verification.

Part I:

Theoretical foundations

In this part of the thesis, we introduce the main concepts of the quantum many-body problem of molecular physics, name important state-of-the-art approaches to solve it, and briefly explain their benefits and shortcomings. We further extend the many-body problem to electronic systems coupled to photons, which require novel approaches to treat both, light and matter, on equal quantum mechanical footing.

2 Quantum many-body problem

We begin by introducing the many-body problem of atomic, molecular and condensed matter physics, which will be further reduced to an electron-only problem. We further regard only systems, where relativistic effects do not play a role. Also, only closed systems, i.e. systems that exchange neither particles nor energy with their environment, are considered. In case of more than one electron, we will only deal with systems that have the same amount of spin-up and spin-down electrons and, hence, an even number of particles. Those systems are called closed-shell systems.

2.1 Schrödinger equation

In standard quantum mechanics, a closed system at a given time t is uniquely described by a vector $|\Psi(t)\rangle$[1] in an abstract complex Hilbert space $\mathscr{H}$ that we will discuss in section 2.2 in greater detail. Here, we just establish the fact that to this space we can assign a dual space $\mathscr{H}^*$ (also a Hilbert space), such that elements of this dual space $\langle\Psi| \in \mathscr{H}^*$ are linear functionals that map vectors from $\mathscr{H}$ onto complex numbers [47, 48]

$$\mathscr{H}^* = [\langle\Psi|;\ \langle\Psi| : \mathscr{H} \longrightarrow \mathbb{C};\ \langle\Psi|\ \text{linear}] \tag{2.1}$$

The main principle in physics is that information about a system is gained by measuring it and we call every measurable quantity an observable. In quantum mechanics, an observable O is represented by a linear self-adjoint[2] operator $\hat{O}$ on $\mathscr{H}$ and it's measured value is given by

$$\langle O\rangle = \frac{\langle\Psi|\hat{O}|\Psi\rangle}{\langle\Psi|\Psi\rangle}, \tag{2.2}$$

if the system is in state $|\Psi(t)\rangle \neq 0$. The states are usually normalized $\langle\Psi|\Psi\rangle = 1$.

Perhaps the most important observable of a system is the energy. The corresponding operator is called the Hamiltonian $\hat{H}$ of the system. It fully determines the dynamics of a system for a given initial state $|\Psi(t_0)\rangle$ via the *time-dependent Schrödinger equation*

$$i\hbar\frac{\partial}{\partial t}|\Psi(t)\rangle = \hat{H}|\Psi(t)\rangle. \tag{2.3}$$

Specifically, for *time-independent* Hamiltonians the time-dependent Schrödinger equation can be solved by separating a solution $|\Psi_j(t)\rangle$ in its spatial and temporal part and considering the temporal part first. The state

$$|\Psi_j(t)\rangle = e^{-i\frac{E_i}{\hbar}t}|\Psi_j\rangle \tag{2.4}$$

is a solution, which is easily verified by inserting it into Eq. (2.3)

$$i\hbar\frac{\partial}{\partial t}|\Psi_j(t)\rangle = e^{-i\frac{E_i}{\hbar}}E_j|\Psi_j\rangle = e^{-i\frac{E_i}{\hbar}}\hat{H}|\Psi_j\rangle. \tag{2.5}$$

[1] We will often drop the functional dependence on time, if it is not particularly important.
[2] For $\mathscr{H}$ finite the attribute self-adjoint is equivalent to hermitian.

In this way we have eliminated the time-dependence from Eq. (2.3). The remaining part is the *time-independent Schrödinger equation*

$$\hat{H}|\Psi_j\rangle = E_j|\Psi_j\rangle, \tag{2.6}$$

which we from now on simply call Schrödinger equation. The states $|\Psi_j\rangle$ are called eigenstates of $\hat{H}$. The lowest eigenstate, if it exists, is the ground-state of the system $|\Psi_0\rangle$ with the energy E_0.

To solve Eq. (2.6) for a certain set of systems is the major task in electronic structure theory. It is a high-dimensional problem and requires approximations in most cases, some of which we will introduce in section 3.1. But first, we will discuss underlying Hilbert spaces $\mathscr{H}$ and Hamiltonians in the rest of this chapter.

2.2 Spaces in quantum mechanics

2.2.1 One-particle Hilbert space

We begin the investigation of spaces in quantum mechanics with the simplest case of one (spinless) particle moving in some external potential $v(\boldsymbol{r})$. In position space it is described by a complex-valued $\varphi(\boldsymbol{r})$, which is called (position-space) wave function. It is related to the state $|\varphi\rangle$ via

$$\varphi(\boldsymbol{r}) = \langle \boldsymbol{r}|\varphi\rangle \qquad \text{or} \qquad |\varphi\rangle = \int d\boldsymbol{r}\varphi(\boldsymbol{r})|\boldsymbol{r}\rangle. \tag{2.7}$$

Here, the Hilbert space is spanned by position vectors $|\boldsymbol{r}\rangle$ and $\varphi(\boldsymbol{r})$ are the expansion coefficients of the state $|\varphi\rangle$ in this space[3]. The scalar product in this case simplifies to the L^2-scalar product

$$\langle\varphi'|\varphi\rangle = \int d\boldsymbol{r}\int d\boldsymbol{r}'\varphi'^*(\boldsymbol{r}')\varphi(\boldsymbol{r})\underbrace{\langle\boldsymbol{r}'|\boldsymbol{r}\rangle}_{\delta(\boldsymbol{r}'-\boldsymbol{r})} = \int d\boldsymbol{r}\varphi'^*(\boldsymbol{r})\varphi(\boldsymbol{r}). \tag{2.8}$$

The Hamiltonian is obtained by promoting the canonical coordinate $\boldsymbol{r}$ and momentum $\boldsymbol{p}$ in the corresponding classical Hamiltonian (sum of kinetic energy T and potential energy V) [47]

$$H = \frac{\boldsymbol{p}^2}{2m} + v(\boldsymbol{r}) \tag{2.9}$$

to operators $\hat{\boldsymbol{r}}$ and $\hat{\boldsymbol{p}}$. In real-space these operators are [49]

$$\hat{\boldsymbol{p}} = -i\hbar\nabla \qquad \hat{\boldsymbol{r}} = \boldsymbol{r} \tag{2.10}$$

Hence, we obtain the following one-particle Hamiltonian in real-space representation[4]

$$\hat{h} = -\frac{\hbar^2\nabla^2}{2m} + v(\boldsymbol{r}). \tag{2.11}$$

The eigenstates of this Hamiltonian that follow from

$$\hat{h}\varphi_i(\boldsymbol{r}) = \varepsilon_i\varphi_i(\boldsymbol{r}) \tag{2.12}$$

[3] Note that also the state $|\varphi\rangle$ is often called wave function as well as any other representation of $|\varphi\rangle$ such as the momentum-space representation $\varphi(\boldsymbol{p})$.

[4] We use lowercase symbols like $\hat{h}$ for operators that contain only one coordinate at a time (one-body operators) and uppercase symbols like $\hat{H}$ for operators that depend on more than one coordinate (many-body operators), respectively.

are complex functions that span the full Hilbert space $\mathscr{H}^{(1)}$ of the problem. Examples are plane waves[5] $\psi(\boldsymbol{r}) = e^{\frac{i}{\hbar}\boldsymbol{p}\cdot\boldsymbol{r}}$ with fixed momenta that are solutions of the one-body Schrödinger equation for $v(\boldsymbol{r}) = 0$ or hydrogen atomic orbitals for the electrostatic potential of one proton. In the continuum, the number of these eigenfunctions is uncountably infinite. In practice, however, their amount is reduced to a finite number.

To make the description of an electron complete, we need to add a spin that is accounted for by a two-dimensional space. Non-relativistic one-particle Hamiltonians without magnetic fields do not contain spin-dependent terms, so their spectra are not affected by the spin. Hence, one-electron wave-functions can simply be written as a product of a spatial and a spin wave function

$$\psi(\boldsymbol{x}) = \begin{cases} \varphi(\boldsymbol{r})\sigma(\chi) \equiv \psi^{\sigma}(\boldsymbol{r}), \\ \varphi(\boldsymbol{r})\sigma'(\chi) \equiv \psi^{\sigma'}(\boldsymbol{r}), \end{cases} \tag{2.13}$$

where $\sigma^{(\prime)}$ are two orthonormal functions accounting either for spin up ($\uparrow$) or for spin down ($\downarrow$). The wave function ψ is called a *spin orbital*. For the sake of convenience, we will use a combined variable $x = (\boldsymbol{r}, \sigma)$ and denote a spin orbital simply by $\psi(\boldsymbol{x})$. We will refer to spin orbitals also as one-particle basis functions of the Hilbert space. The dimension of the one-particle Hilbert space equals to the number of considered spin orbitals that we denote by $2N$, with N being the number of spatial orbitals $\varphi(\boldsymbol{r})$. In this thesis, we only will use orthonormal basis sets with

$$\langle\varphi'|\varphi\rangle = \int d\boldsymbol{r}\varphi'^{*}(\boldsymbol{r})\varphi(\boldsymbol{r}) = \delta_{\varphi\varphi'}. \tag{2.14}$$

2.2.2 Many-particle Hilbert space

Many-particle Hilbert spaces are build from one-particle Hilbert spaces and many-body wave functions are build from spin orbitals. If we assume two non-interacting distinguishable electrons, their two-body wave function would be

$$\Phi_{\text{dist.}}(\boldsymbol{x}_1, \boldsymbol{x}_2) = \psi_1(\boldsymbol{x}_1)\psi_2(\boldsymbol{x}_2). \tag{2.15}$$

Electrons, however, are indistinguishable particles, meaning we could not tell them apart by performing any kind of measurement. The spin-statistic theorem [50] states that there are only two kinds of particles:

- bosons that have integer-spin and whose wave function has the same value (is symmetric) when the coordinates of any two particles are swapped,
- fermions that have half-integer-spin and whose wave function changes sign (is antisymmetric) when the coordinates of any two particles are swapped.

Electrons are fermions and therefore the wave function of two electrons has to fulfill the condition $\Phi(\boldsymbol{x}_1, \boldsymbol{x}_2) = -\Phi(\boldsymbol{x}_2, \boldsymbol{x}_1)$, from which follows that

$$\Phi(\boldsymbol{x}_1, \boldsymbol{x}_2) = \frac{1}{\sqrt{2}}\left(\psi_1(\boldsymbol{x}_1)\psi_2(\boldsymbol{x}_2) - \psi_1(\boldsymbol{x}_2)\psi_2(\boldsymbol{x}_1)\right). \tag{2.16}$$

This is in accordance to the Pauli exclusion principle, which states that two particles cannot occupy the same spin orbital.

[5] Strictly speaking, plane waves are *generalized* eigenstates of the kinetic energy operator, since they are defined on an infinite space and cannot be normalized. In physics literature, however, this subtlety is usually neglected.

The function in Eq. (2.16) is also regarded as the anti-symmetric product of two spin orbitals. The generalization to the N_e-particle case is given by

$$\Phi\big(\{\boldsymbol{x}_i\}\big) = \frac{1}{\sqrt{N_e!}} \begin{vmatrix} \psi_1(\boldsymbol{x}_1) & \psi_1(\boldsymbol{x}_2) & \cdots & \psi_1(\boldsymbol{x}_{N_e}) \\ \psi_2(\boldsymbol{x}_1) & \psi_2(\boldsymbol{x}_2) & \cdots & \psi_2(\boldsymbol{x}_{N_e}) \\ \vdots & \vdots & \ddots & \vdots \\ \psi_{N_e}(\boldsymbol{x}_1) & \psi_{N_e}(\boldsymbol{x}_2) & \cdots & \psi_{N_e}(\boldsymbol{x}_{N_e}) \end{vmatrix}, \tag{2.17}$$

$$|\Phi\rangle = \frac{1}{\sqrt{N_e!}} \bigwedge_{i=1}^{N_e} |\psi_i\rangle \equiv |\psi_1 \cdots \psi_{N_e}\rangle^-, \tag{2.18}$$

where $\wedge$ denotes the per construction anti-symmetric wedge product[6] [51]. In Eq. (2.18) we introduced the general form of a Slater determinant and in Eq. (2.17) its real-space representation.

For a given set of orbitals, all possible Slater determinants build the N_e-particle Hilbert space of the problem. For the space itself we write

$$\mathscr{H}_-^{(N_e)} \equiv \bigwedge_{i=1}^{N_e} \mathscr{H}^{(1)} \quad \subset \quad \bigotimes_{i=1}^{N_e} \mathscr{H}^{(1)} \equiv \mathscr{H}^{(N_e)}. \tag{2.19}$$

The N_e-electron Hilbert space $\mathscr{H}_-^{(N_e)}$ is anti-symmetrized by construction, since it is spanned by all possible N_e-particle Slater determinants that can be built from $2N$ basis functions. It's dimension is given by a binomial coefficient

$$\dim \mathscr{H}_-^{(N_e)} = \binom{2N}{N_e}. \tag{2.20}$$

As indicated in Eq. (2.19), $\mathscr{H}_-^{(N_e)}$ can be viewed as a subspace of a larger Hilbert space $\mathscr{H}^{(N_e)}$ that does not include particle-exchange symmetry. In practice, it is often used even though it has unphysical states, since it is easier to construct. In these cases, wave functions with the proper symmetry are chosen.

2.2.3 Fock space

Usually, when relativistic effects are neglected and the system is closed, the electronic Hamiltonian conserves the number of particles, i.e. an N_e-particle wave function propagated in time remains an N_e-particle wave function. So it is sufficient to consider only N_e-particle Hilbert spaces introduced in the previous section. However, it will prove useful to consider more complex spaces, the so-called Fock spaces, as they provide the basis for the formalism of second quantization.

The electronic Fock space is given by a direct sum of Hilbert spaces with all possible numbers of particles up to N_e, starting with 0 particles (vacuum space, which is identified by $\mathbb{C}$)

$$\mathscr{F} = \mathbb{C} \oplus \mathscr{H}_-^{(1)} \oplus \mathscr{H}_-^{(2)} \oplus \cdots \oplus \mathscr{H}_-^{(2N)}. \tag{2.21}$$

We can now relate Slater determinants with basis states in Fock space via

$$|\Phi_i\rangle \to 0 \oplus 0 \oplus \cdots \oplus |\Phi_i\rangle \oplus \cdots \oplus 0. \tag{2.22}$$

The basis is complete, if we further define the vacuum $|0\rangle \equiv |\Phi_0\rangle$. We are now able to define the identity operator on $\mathscr{F}$ as

$$\mathbb{1}_{\mathscr{F}} = \sum_{i=0}^{4^N} |\Phi_i\rangle\langle\Phi_i|, \tag{2.23}$$

[6] $a \wedge b = -(b \wedge a)$

where the limits result from summing over Hilbert-space dimensions from Eq. (2.20) for all possible electron numbers

$$\dim \mathscr{F} = \sum_{N_\mathrm{e}=0}^{2N} \binom{2N}{N_\mathrm{e}} = 4^N. \tag{2.24}$$

By employing Eq. (2.23), any wave function can be represented as

$$|\Psi\rangle = \sum_{i=0}^{4^N} |\Phi_i\rangle \underbrace{\langle \Phi_i|\Psi\rangle}_{\equiv \Psi_i} \tag{2.25}$$

and an operator as

$$\hat{O} = \sum_{i=0}^{4^N} \sum_{j=0}^{4^N} |\Phi_i\rangle \underbrace{\langle \Phi_i|\hat{O}|\Phi_j\rangle}_{\equiv O_{ij}} \langle \Phi_j| \tag{2.26}$$

The equations above provide a vector-matrix representation of states and linear operators in Fock space.

2.3 Second quantization

Second quantization is a formalism that allows for efficient treatment of identical particles and can be applied to both, fermions and bosons. Here we will consider only electrons and apply the same concepts to bosons later in section 4.2, when we introduce photons as quanta of the electromagnetic field.

In the formalism of second quantization, a basis function of a many-body Hilbert space is not written as a complex function of spatial and spin coordinates of every particle, which includes the bothersome anti-symmetrization embodied in its determinant structure (see Eq. (2.17)). It is rather formulated in terms of occupation numbers of every basis function spanning the one-particle Hilbert space. Due to the Pauli-exclusion principle, for fermions all these occupation number are given by either 1 or 0.

Hilbert spaces with different particle numbers within the Fock space are then connected through adding or removing particles from certain orbitals, meaning adding or removing corresponding rows and columns from Slater determinants. We call the described transition between neighboring Hilbert spaces creation or annihilation of a single electron. The corresponding operators read

$$\hat{c}_j^\dagger : \qquad \mathscr{F} \to \mathscr{F} \quad \left(\mathscr{H}_-^{(n)} \to \mathscr{H}_-^{(n+1)}\right), \tag{2.27}$$

$$|\psi_1 \cdots \psi_n\rangle^- \mapsto |\psi_j \psi_1 \cdots \psi_n\rangle^-, \tag{2.28}$$

$$\text{and} \quad \hat{c}_j : \qquad \mathscr{F} \to \mathscr{F} \quad \left(\mathscr{H}_-^{(n+1)} \to \mathscr{H}_-^{(n)}\right), \tag{2.29}$$

$$\hat{c}_j = \left(\hat{c}_j^\dagger\right)^\dagger, \qquad \text{with} \quad \hat{c}_j|0\rangle = 0. \tag{2.30}$$

Every basis state in the Fock space can be constructed as

$$|\psi_1 \cdots \psi_n\rangle^- = \hat{c}_1^\dagger \cdots \hat{c}_n^\dagger |0\rangle. \tag{2.31}$$

The anti-symmetric character of fermionic states results in the following feature: when applying two annihilation operators, we obtain

$$\hat{c}_2 \hat{c}_1 |\psi_1 \psi_2 \cdots \psi_n\rangle^- = |\psi_3 \cdots \psi_n\rangle^-, \tag{2.32}$$

$$\hat{c}_1 \hat{c}_2 |\psi_1 \psi_2 \cdots \psi_n\rangle^- = -\hat{c}_1 \hat{c}_2 |\psi_2 \psi_1 \cdots \psi_n\rangle^- = -|\psi_3 \cdots \psi_n\rangle^-. \tag{2.33}$$

This can be generalized to the anti-commutator[7] relations for fermionic creation and annihilation operators

$$\left\{\hat{c}_i, \hat{c}_j\right\} = \left\{\hat{c}_i^\dagger, \hat{c}_j^\dagger\right\} = 0, \qquad \left\{\hat{c}_i, \hat{c}_j^\dagger\right\} = \delta_{ij}. \tag{2.34}$$

We further define the occupation-number operator

$$\hat{c}_i^\dagger \hat{c}_i |\Phi\rangle = |\Phi\rangle \begin{cases} 1, & \text{if } |\psi_i\rangle \text{ in } |\Phi\rangle, \\ 0, & \text{if } |\psi_i\rangle \text{ not in } |\Phi\rangle. \end{cases} \tag{2.35}$$

Hence, a Slater determinant is fully determined by the number of particles and occupation numbers of every orbitals.

At this point, we want to mention that the Fock space $\mathscr{F}$ itself can be equivalently constructed (in the style of second quantization) as a tensor product of what we call spin-orbital Fock spaces. In fact, we can assign a Fock space to each spin-orbital $|\psi_j\rangle$

$$\mathscr{F}_j \equiv |0\rangle_j \oplus |1\rangle_j, \tag{2.36}$$

since every fermionic orbital is either empty ($|0\rangle$) or occupied ($|1\rangle$), resulting in a set of two-dimensional orbital Fock spaces. The full Fock space is then constructed via

$$\mathscr{F} = \bigotimes_{j=1}^{N} \mathscr{F}_j \tag{2.37}$$

and we can associate e.g. for the vacuum

$$|0\rangle = \bigotimes_{j=1}^{N} |0\rangle_j. \tag{2.38}$$

This construction can be easily defined for a finite orbital set and is equivalent to the construction in Eq. (2.21).

Operators in second quantization

Since every basis state of the Fock space can be constructed by employing creation and annihilation operators, also every linear operator on this space can be expressed in terms of these operators. This is done by combining Eq. (2.26) and Eq. (2.31).

We will show this reformulation explicitly for a relevant set of operators, namely those that conserve the number of particles in the system and that depend on at most two particle coordinates, since all electronic Hamiltonians considered here share these features (see section 2.4 for more details). Generalization to other types of operators is straight-forward.

We begin by writing an operator $\hat{O}$ as a sum of its one and two-body components

$$\hat{O} = \sum_{i}^{N_e} \hat{O}_i^{(1)} + \frac{1}{2} \sum_{i,j}^{N_e} \hat{O}_{i,j}^{(2)}, \tag{2.39}$$

meaning that $\hat{O}_i^{(1)}$ acts on particle i and $\hat{O}_{i,j}^{(2)}$ on particles i and j simultaneously. From section 2.3 we know that Slater determinants can be mapped onto each other with help of creation and annihilation operators. As an example, consider two determinants with the same number of electrons $|\Phi_i\rangle$ and $|\Phi_j\rangle$ that differ by only one orbital, $|\psi_i\rangle$ in $|\Phi_i\rangle$ and $|\psi_j\rangle$ in $|\Phi_j\rangle$, respectively.

[7] $\{a, b\} = ab + ba$

We can relate them via

$$|\Phi_i\rangle = \hat{c}_i^\dagger \hat{c}_j |\Phi_j\rangle. \tag{2.40}$$

If we now apply the one-body part of $\hat{O}$ to a Slater determinant

$$\sum_i^{N_\mathrm{e}} \hat{O}_1^{(i)} |\Phi_j\rangle = \sum_i^{N_\mathrm{e}} |\psi_1 \cdots \hat{O}_1 \psi_i \cdots \psi_{N_\mathrm{e}}\rangle^-, \tag{2.41}$$

we immediately see that only those matrix elements $\langle\Phi_i|\hat{O}|\Phi_j\rangle$ can differ from zero, for which $|\Phi_i\rangle$ and $|\Phi_j\rangle$ differ at most by only one orbital. Hence, we can conclude that

$$\sum_i^{N_\mathrm{e}} \hat{O}_1^{(i)} \quad \rightarrow \quad \sum_{i,j=1}^{N_\mathrm{e}} \langle\psi_i|\hat{O}_1|\psi_j\rangle \hat{c}_i^\dagger \hat{c}_j. \tag{2.42}$$

For the two-body part, the expression

$$\frac{1}{2}\sum_{i,j}^{N_\mathrm{e}} \hat{O}_2^{(i,j)} \quad \rightarrow \quad \frac{1}{2}\sum_{i,j,k,l}^{N_\mathrm{e}} \langle\psi_i\psi_j|\hat{O}_2|\psi_k\psi_l\rangle \hat{c}_i^\dagger \hat{c}_j^\dagger \hat{c}_l \hat{c}_k \tag{2.43}$$

can be derived in the same manner.

2.4 Molecular Hamiltonian

In this section, we introduce a typical Hamiltonian used in atomic, molecular and condensed matter physics. It is constructed from the kinetic energies of the nuclei (subscript n) and the electrons (subscript e) as well as all possible electrostatic particle-particle interactions ($\hat{W}$-operators)

$$\hat{H}_\mathrm{en} = \hat{T}_\mathrm{e} + \hat{T}_\mathrm{n} + \hat{W}_\mathrm{ee} + \hat{W}_\mathrm{nn} + \hat{W}_\mathrm{en}. \tag{2.44}$$

At this point, no external potentials like e.g. electromagnetic potentials are included.

In real space individual terms in atomic units[8] read:

$$\hat{T}_\mathrm{e} = \quad -\sum_{j=1}^{N_\mathrm{e}} \frac{\nabla_{\boldsymbol{r}_j}^2}{2} \tag{2.45}$$

$$\hat{T}_\mathrm{n} = \quad -\sum_{J=1}^{N_\mathrm{n}} \frac{\nabla_{\boldsymbol{R}_J}^2}{2M_J} \tag{2.46}$$

$$\hat{W}_\mathrm{ee} = \quad \sum_{j=1}^{N_\mathrm{e}} \sum_{k>j}^{N_\mathrm{e}} \frac{1}{|\boldsymbol{r}_j - \boldsymbol{r}_k|} \tag{2.47}$$

$$\hat{W}_\mathrm{nn} = \quad \sum_{J=1}^{N_\mathrm{n}} \sum_{K>J}^{N_\mathrm{n}} \frac{Z_J Z_K}{|\boldsymbol{R}_J - \boldsymbol{R}_K|} \tag{2.48}$$

$$\hat{W}_\mathrm{en} = -\sum_{j=1}^{N_\mathrm{e}} \sum_{K=1}^{N_\mathrm{n}} \frac{Z_K}{|\boldsymbol{r}_j - \boldsymbol{R}_K|} \tag{2.49}$$

Here, lowercase letters are used for electrons and uppercase letters for nuclei, respectively. The symbol M_J denotes the mass and Z_J the atomic number of the nucleus J. This Hamiltonian can be obtained from classical mechanics in the same fashion as the one-body Hamiltonian in section 2.2.1 with additional pairwise interactions between all charged particles, which here is accounted for by the Coulomb interaction.

[8] We use atomic units starting from here throughout the thesis, if not stated otherwise.

2.4.1 Born-Oppenheimer approximation

The Hamiltonian in Eq. (2.44) is often simplified by applying the Born-Oppenheimer (BO) approximation [52]. This approximation is based on the fact that nuclei are much heavier than electrons and therefore usually much slower. Consequently, it is a reasonable approximation to consider electrons that move in an electrostatic field created by fixed nuclear charges. The nuclear kinetic energy is then approximately zero and nuclear coordinates enter the Schrödinger equation not as variables, but as parameters.

Hence, we can approximately solve the Schrödinger equation for $\hat{H}_{\text{en}}$, if we first solve the electronic Schrödinger equation for every set of nuclear coordinates

$$\hat{H}_{\text{e},\,\{\boldsymbol{R}_J\}}|\Psi_{\text{e}}\rangle_{\{\boldsymbol{R}_J\}} = E_{\text{e},\,\{\boldsymbol{R}_J\}}|\Psi_{\text{e}}\rangle_{\{\boldsymbol{R}_J\}}, \tag{2.50}$$

with

$$\hat{H}_{\text{e},\,\{\boldsymbol{R}_J\}} = \underbrace{-\sum_{j=1}^{N_{\text{e}}}\frac{1}{2}\nabla^2_{\boldsymbol{r}_j}}_{\hat{T}} + \underbrace{\sum_{j=1}^{N_{\text{e}}}\sum_{k>j}^{N_{\text{e}}}\frac{1}{|\boldsymbol{r}_j-\boldsymbol{r}_k|}}_{\hat{W}} + \underbrace{v_{\{\boldsymbol{R}_J\}}\big(\{\boldsymbol{r}_i\}\big)}_{\hat{V}} \tag{2.51}$$

and

$$v_{\{\boldsymbol{R}_J\}}\big(\{\boldsymbol{r}_i\}\big) = -\sum_{j=1}^{N_{\text{e}}}\sum_{K=1}^{N_{\text{n}}}\frac{Z_K}{|\boldsymbol{r}_j-\boldsymbol{R}_K|}. \tag{2.52}$$

Here, the subscript $\{\boldsymbol{R}_J\}$ denotes the *parametric* dependence on nuclear coordinates. We will drop this dependence later and just refer to the electrostatic potential of the nuclei as some external potential $v_{\text{ext}}(\boldsymbol{r})$.

Although it is much simpler than the original molecular many-body problem, solving the purely electronic Schrödinger equation accurately for many-electron systems remains one of the main challenges in electronic structure theory. Due to the instantaneous electron-electron repulsion, all electrons have to be taken into account simultaneously, which does not allow for any simple additional separation (parametric treatment of electronic coordinates).

We will dedicate large parts of this thesis to approximate methods for solving the electronic many-body problem. But before considering these methods, let us briefly discuss how we would proceed with the solutions. In the clamped-nuclei approximation, additionally to the energy of the electrons $E_{\text{e},\,\{\boldsymbol{R}_J\}}$, the total energy of the system must include the (in this case constant) repulsion energy of the nuclei

$$E_{\text{e},\,\{\boldsymbol{R}_J\}} + \sum_{J=1}^{N_{\text{n}}}\sum_{K>1}^{N_{\text{n}}}\frac{Z_J Z_K}{|\boldsymbol{R}_J-\boldsymbol{R}_K|}. \tag{2.53}$$

Further, we already have established that within the BO approximation, the electrons react instantaneously to nuclear motion. Hence, if we try to solve for the ground state of the full system, we can always assume that the electrons are in their ground state for any particular molecular configuration. In the light of the above, for the nuclear Hamiltonian we write

$$\hat{H}^{\text{BO}}_{\text{n}} = -\sum_{J=1}^{N_{\text{n}}}\frac{1}{2M_J}\nabla^2_{\boldsymbol{R}_J} + \underbrace{E_{\text{e},\,\{\boldsymbol{R}_J\}} + \sum_{J=1}^{N_{\text{n}}}\sum_{K>1}^{N_{\text{n}}}\frac{Z_J Z_K}{|\boldsymbol{R}_J-\boldsymbol{R}_K|}}_{V^{\text{BO}}(\{\boldsymbol{R}_J\})}. \tag{2.54}$$

Here, the clamped-nuclei energy of the system as defined in Eq. (2.53) serves as a potential energy surface $V^{\text{BO}}\big(\{\boldsymbol{R}_J\}\big)$ on which the nuclei move.

The BO approximation provides remarkably good results for a large range of problems, especially for energetically low-lying potential energy surfaces [53]. In this thesis, we will always work within the BO approximation and concentrate on solving the electronic Schrödinger equation in Eq. (2.50), especially for the electronic ground state.

2.4.2 Electronic Hamiltonian in second quantization

We reformulate the clamped-nuclei Hamiltonian of Eq. (2.51) in terms of particle creation and annihilation operators as introduced in section 2.3

$$\hat{H}_\mathrm{e} = \underbrace{\hat{T}+\hat{V}}_{\equiv\hat{h}} + \hat{W} = \sum_{i,j,\sigma} h_{ij}\hat{c}^\dagger_{i\sigma}\hat{c}_{j\sigma} + \frac{1}{2}\sum_{i,j,k,l,\sigma,\sigma'} W_{ijkl}\hat{c}^\dagger_{i\sigma}\hat{c}^\dagger_{j\sigma'}\hat{c}_{l\sigma'}\hat{c}_{k\sigma}\,. \tag{2.55}$$

By following Eqs. (2.42)-(2.43), the pre-factors in Eq. (2.55) are given by

$$h_{ij} = \int d\boldsymbol{r}\; \varphi^*_i(\boldsymbol{r})\left[-\frac{1}{2}\nabla^2_{\boldsymbol{r}} + v_\mathrm{ext}(\boldsymbol{r})\right]\varphi_j(\boldsymbol{r}), \tag{2.56}$$

$$W_{ijkl} = \int d\boldsymbol{r}\int d\boldsymbol{r}'\varphi^*_i(\boldsymbol{r})\varphi^*_j(\boldsymbol{r}')\frac{1}{|\boldsymbol{r}-\boldsymbol{r}'|}\varphi_l(\boldsymbol{r}')\varphi_k(\boldsymbol{r}). \tag{2.57}$$

These quantities are often referred to as one- and two-electron integrals over spatial orbitals. More generally, two-electron integrals for spin-orbitals in physicists' notation[9] are defined as

$$\langle ij|kl\rangle = \int d\boldsymbol{x}\int d\boldsymbol{x}'\psi^*_i(\boldsymbol{x})\psi^*_j(\boldsymbol{x}')\frac{1}{|\boldsymbol{r}-\boldsymbol{r}'|}\psi_l(\boldsymbol{x}')\psi_k(\boldsymbol{x}) \tag{2.58}$$

and certain pairs of these integrals are summarized as

$$\langle ij||kl\rangle = \langle ij|kl\rangle - \langle ij|lk\rangle. \tag{2.59}$$

We will use these expressions later in section 3.1.3.

[9] In chemistry, usually a different notation due to different order of orbitals is used.

3 Methods in electronic structure theory

Even though the complexity of the Schrödinger equation for a molecular or condensed matter system can be reduced significantly by applying the BO approximation, it still can be solved exactly only for a small range of problems. This is caused by the fact that the Hilbert space of the problem grows exponentially with the number of single-particle basis states (see Eq. (2.20) and Eq. (2.24)), a problem that is known as the *exponential wall* of many-body physics.

In this chapter, we briefly introduce popular methods to attack this wall. We will only consider *ab initio* methods, which means that only physical constants and mathematical principles are used to develop approximations and no empirical knowledge e.g. from experiments is used. *Ab initio* electronic structure methods can be roughly divided into two categories (see Fig. 1):

- **Wave-function methods:** These are methods that aim at directly approximating the many-body wave function of the system. Here, we will concentrate on popular methods used in quantum chemistry [5] with emphasis on coupled-cluster theory [15]. Most wave-function methods are still computationally expensive and can only be applied to rather small systems.

- **Functional methods:** These methods replace the wave-function as a descriptor for the system by a lower dimensional object. Observables are then calculated in terms of this lower dimensional object. Here, we will introduce probably the most popular of these methods – density-functional theory [8]. Its computational efficiency makes it applicable to a large range of problems. The accuracy of results, however, strongly depends on the particular system as well as the chosen functional.

Methods from both groups provide results with different levels of accuracy, depending on approximations utilized in them as well as the particular system to which a method is applied. Methods that combine high-level with low-level approaches are commonly referred to as *embedding theories* [7, 54, 55]. Those methods enable the quantum treatment of large system by combining an accurate description of parts of a system with computationally cheap treatment

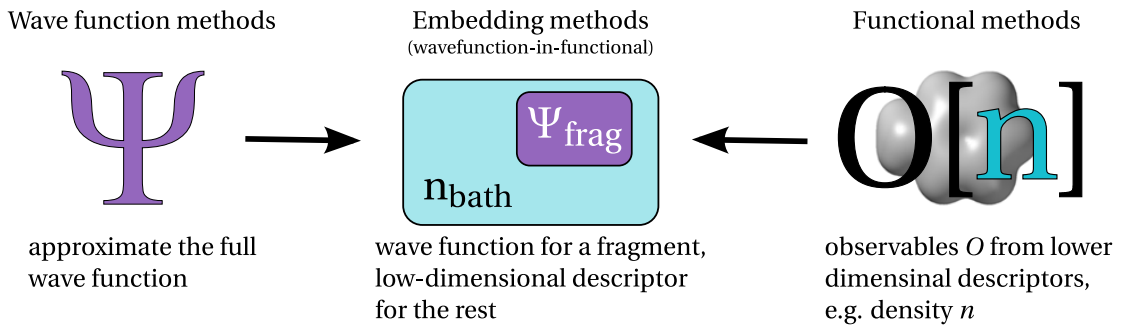

Figure 1. Overview of strategies to solve the electronic Schrödinger equation. Roughly speaking, electronic structure methods either target directly the many-body wave function of the system or a derived lower dimensional object. Combination of both strategies is given by (wavefunction-in-functional) embedding methods.

of the rest. Here, we introduce a simple but effective quantum embedding framework given by the DMET approach [20–22].

3.1 Wave function-based approaches

The starting point for method development is the Rayleigh-Ritz variational principle [5]. It states that the energy functional defined on an N_e-electron Hilbert space takes its minimum (if it exists) at the ground-state wave function of the system

$$E_0 = \langle\Psi_0|\hat{H}|\Psi_0\rangle = \min_{\{|\Psi_i\rangle\neq 0\}} \frac{\langle\Psi_i|\hat{H}|\Psi_i\rangle}{\langle\Psi_i|\Psi_i\rangle}, \tag{3.1}$$

which is basically a reformulation of the Schrödinger equation in Eq. (2.6).

Now, since this minimization on the full Hilbert space of the problem is in general not feasible, in practice only a subset of vectors in $\mathscr{H}^{(N_\mathrm{e})}$ is chosen. The energy is then minimized with respect to few parameters that define this subset. Methods that obey the principle in Eq. (3.1) are called variational methods.

3.1.1 Hartree-Fock method

In the Hartree-Fock (HF) method [56, 57], the subset of wave functions on which the minimization of Eq. (3.1) is performed, consists of Slater determinants. The HF solution is obtained via optimizing the spin-orbitals $\{|\psi_i\rangle\}$ from which the Slater determinant $|\Phi_0\rangle$ is built (see Eq. (2.18)). This means, the many-body problem is reduced to the following set of N one-body problems

$$\hat{f}|\psi_i\rangle \equiv \hat{h}|\psi_i\rangle + \sum_{i\neq j}\langle\psi_j|\hat{W}|\psi_j\rangle|\psi_i\rangle - \langle\psi_j|\hat{W}|\psi_i\rangle|\psi_j\rangle = \varepsilon_i|\psi_i\rangle, \tag{3.2}$$

with the following real-space representation of the interaction integrals

$$\langle\psi_a|\hat{W}|\psi_b\rangle|\psi_c\rangle \equiv \left[\int d\boldsymbol{x}\,\psi_a^*(\boldsymbol{x})\psi_b(\boldsymbol{x})\hat{W}(\boldsymbol{r},\boldsymbol{r}')\right]\psi_c(\boldsymbol{x}'). \tag{3.3}$$

The spin-orbitals $|\psi_i\rangle$ are eigenstates of the introduced *Fock operator* $\hat{f} = \hat{f}\left[\{|\psi_i\rangle\}\right]$, meaning that Eq. (3.2) provides a fixed-point scheme and can be solved trough a *self-consistent field* (SCF) algorithm [5, 58]. It consists of:

1. constructing the Fock operator $\hat{f}^{(0)}$ from an initial set of orbitals $\{|\psi_i\rangle\}^{(0)}$;
2. diagonalizing $\hat{f}^{(0)}$ to obtain a new set of orbitals $\{|\psi_i\rangle\}^{(1)}$;
3. repeating this procedure until self-consistency is reached.

In this framework, the HF method boils down to an optimization of the single-particle orbitals from which an approximate ground-state wave function, the HF Slater determinant, is constructed.

The HF Slater determinant is often referred to as the mean-field solution, since the HF approximation can be understood in a way that every electron feels the average Coulomb repulsion of all other electrons, their *mean field*[1].

[1] Generally, mean-field approximation of a product of two one-body operators $\hat{A}$ and $\hat{B}$ means disregarding fluctuation terms from the expansion $\hat{A}\hat{B} = \hat{A}\langle\hat{B}\rangle + \langle\hat{A}\rangle\hat{B} - \langle\hat{A}\rangle\langle\hat{B}\rangle + \cancel{(\hat{A}-\langle\hat{A}\rangle)(\hat{B}-\langle\hat{B}\rangle)}$.

All observables can be calculated as expectation values with respect to the HF Slater determinant, e.g. the HF energy is given by

$$E_{\mathrm{HF}} = \langle\Phi_0|\hat{H}|\Phi_0\rangle = \sum_{i=1}^{N_\mathrm{e}} \varepsilon_i - \frac{1}{2}\sum_{i,j=1}^{N_\mathrm{e}} \langle\psi_i|\langle\psi_j|\hat{W}|\psi_i\rangle|\psi_j\rangle. \tag{3.4}$$

HF theory is the simplest and computationally cheapest wave-function method. The numerically demanding part of the algorithm is the construction of the Fock operator from the two-body interaction term $\hat{W}$, which, if N is the measure of system size, formally scales as N^4. In practice, this scaling is reduced to N^2 by using screening techniques [58] or even to linear scaling [59].

Although based on a crude approximation, the HF method provides surprisingly good results for a large range of problems, often accounting for more than 99% of the total energy. Unfortunately though, the energy differences that matter for chemical processes are usually far below 1% and better approximations are necessary. For many problems, however, the HF Slater determinant provides a good starting point for more accurate methods that basically consist of imposing corrections onto the HF solution by accounting, in one way or another, for missing correlations. These approaches are called *post-HF* methods and we will summarize basic concepts behind them in the following.

3.1.2 Configuration interaction

An N_e-particle wave function is an element of a many-particle Hilbert space introduced in section 2.2.2 and hence can be expressed in terms of Slater determinants. For an interacting system, this expansion *always* consists of more than just one Slater determinant. Since with the HF method we have obtained an optimized basis, we can expand the ground state wave function in terms of all Slater determinants built from this basis. They can be built by exciting electrons from the HF Slater determinant. This means, we destroy electrons in energetically lower (occupied) spin-orbitals $|\psi_i\rangle$, $|\psi_j\rangle$ etc., and create the same number of electrons in energetically higher (unoccupied) spin-orbitals $|\psi_a\rangle$, $|\psi_b\rangle$, etc., respectively[2]. E.g., we define

$$|\Phi_i^a\rangle \equiv \hat{c}_a^\dagger \hat{c}_i |\Phi_0\rangle, \qquad\qquad |\Phi_{ij}^{ab}\rangle \equiv \hat{c}_b^\dagger \hat{c}_a^\dagger \hat{c}_i\, \hat{c}_j |\Phi_0\rangle. \tag{3.5}$$

The resulting determinants are either simply called excited determinants or *configurations*, where the name configuration interaction (CI) originates from. We refer to different orders of excitation as *singles*, *doubles*, etc. (see Fig. 2 for visualization).

We can now expand the ground-state of our interacting system as

$$\begin{aligned} |\Psi_{\mathrm{FCI}}\rangle &= C_0|\Phi_0\rangle + \sum_{i,a} C_i^a |\Phi_i^a\rangle + \sum_{i,j,a,b} C_{ij}^{ab} |\Phi_{ij}^{ab}\rangle + \sum_{i,j,k,a,b,c} C_{ijk}^{abc} |\Phi_{ijk}^{abc}\rangle + \cdots \\ &\equiv C_0|\Phi_0\rangle + \sum_\mu C_\mu \hat{\tau}_\mu |\Phi_0\rangle, \end{aligned} \tag{3.6}$$

where we have defined excitation operators $\hat{\tau}_\mu = \hat{c}_a^\dagger \hat{c}_i,\ \hat{c}_b^\dagger \hat{c}_a^\dagger \hat{c}_i\, \hat{c}_j,\ \ldots$

The CI approach [5] consists of minimizing the energy by optimizing the coefficients C in the expansion, after the expansion is truncated at a desired order. E.g. in CI singles doubles (CISD) only singly and doubly excited determinants are included. This procedure is equivalent to diagonalizing the Hamiltonian in the subspace of chosen determinants and therefore also calculation of excited states of the system is naturally included in the CI approach.

[2] In this context, indicies $i, j, k, l, \ldots$ will always denote occupied orbitals and indicies $a, b, c, d, \ldots$ empty orbitals.

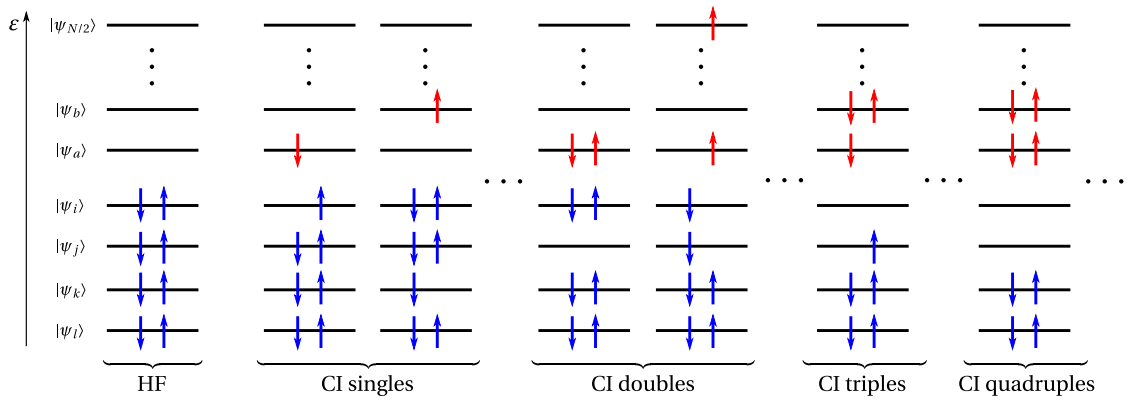

Figure 2. Visualization of HF and CI Slater determinants and their excitation order. Excited determinants are built by promoting electrons from occupied HF spin-orbitals $|\psi_i\rangle$, $|\psi_j\rangle$, etc. to energetically higher, unoccupied HF spin-orbitals $|\psi_a\rangle$, $|\psi_b\rangle$.

If all possible determinants are kept in Eq. (3.6), the method is called full configuration interaction (FCI) [14] or, equivalently, exact diagonalization. Unfortunately, the dimension of this problem is the same as the size of the Hilbert space and, hence, the computational cost grows exponentially with system size. In contrast, the cost of truncated CI calculations grows polynomially, e.g. in case of CISD as N^6 [3].

Truncated CI methods are variational and linear in expansion coefficients. Unfortunately, they are still computationally demanding and also suffer from size-extensivity (the total energy must scale linearly with the number of particles) and size-consistency (the total energy is sum of subsystem energies in case of non-interacting subsystems) issues [5]. The latter can be illustrated by considering two separated hydrogen atoms with two spatial orbitals in each case. We will denote two electrons (spin-singlet $\uparrow\downarrow$) occupying the lower orbital by $|g\rangle$ and two electrons occupying the upper orbital by $|e\rangle$, respectively. The CI doubles (CID) expansion of an individual atom is

$$|\Psi_{\mathrm{CID}}\rangle_{A/B} = C_0|g\rangle_{A/B} + C_1|e\rangle_{A/B} \tag{3.7}$$

For a combined system we get

$$|\Psi_{\mathrm{CID}}\rangle_{A+B} = \widetilde{C}_0|g\rangle_A|g\rangle_B + \widetilde{C}_1|e\rangle_A|g\rangle_B + \widetilde{C}_3|g\rangle_A|e\rangle_B \tag{3.8}$$

On the other hand, in order to provide a size-consistent energy for two non-interacting molecules $E_{A+B} = E_A + E_B$, the combined wave function has to factorize

$$\begin{aligned}\big(C_0|g\rangle_A + C_1|e\rangle_A\big)\big(C_0|g\rangle_B + C_1|e\rangle_B\big) = \\ C_0^2|g\rangle_A|g\rangle_B + C_0C_1|e\rangle_A|g\rangle_B + C_0C_1|g\rangle_A|e\rangle_B + C_1^2|e\rangle_A|e\rangle_B.\end{aligned} \tag{3.9}$$

By comparing Eq. (3.9) with Eq. (3.8), we see that CID introduces a spurious correlation by excluding the quadruple excitation $|e\rangle_A|e\rangle_B$ in the expansion, meaning that molecule A can be excited only if molecule B is not and vice versa. This issue is solved in coupled-cluster theory.

3.1.3 Coupled-cluster theory

In the following, we will outline one of the most powerful approaches in quantum chemistry – the CC theory. It provides a systematic way on how to approximate higher-order excited determinants by lower-order coefficients. Within a certain level of approximation (singles, doubles and perturbative triples), the method achieves energy resolutions on a level of chemical accuracy while keeping the key-properties of the exact wave-function, such as size-extensivity,

[3] See section 3.1.3 or [60] for a more detailed discussion on scaling.

intact and is therefore known as golden standard of quantum chemistry. An comprehensive review on CC theory can be found in [15] and an excellent pedagogical introductions in [60, 61].

CC ansatz

Considering Eq. (3.9) reveals that, although the number of determinants needed for a size-consistent description equals to four, all of them can be taken into account by just two expansion coefficients. This observation is utilized in CC theory as follows: similar to CI, in CC theory we expand a ground-state wave function as a sum of HF and excited determinants, but here we do it as a product *ansatz*

$$|\Psi_{\mathrm{CC}}\rangle = \prod_{\mu} \left(1 + t_\mu \hat{\tau}_\mu\right) |\Phi_0\rangle. \tag{3.10}$$

The excitation operators are the same that have been introduced in Eq. (3.6). The nomenclature for the excitation order refers to the number of creation-annihilation operator pairs entering the excitation operators. Through the product ansatz though, also higher excited determinants enter the expansion: e.g. in CC doubles (CCD)[4] we would obtain

$$|\Psi_{\mathrm{CCD}}\rangle = |\Phi_0\rangle + \sum_{i,j,a,b} t_{ij}^{ab} |\Phi_{ij}^{ab}\rangle + \sum_{i,j,k,l,a,b,c,d} t_{ij}^{ab}\, t_{kl}^{cd} |\Phi_{ijkl}^{abcd}\rangle + \cdots \tag{3.11}$$

The quadruply excited determinant $|\Phi_{ijkl}^{abcd}\rangle$ enters the expansion as it is created by applying a product of two excitation operators, $\hat{c}_b^\dagger \hat{c}_a^\dagger \hat{c}_i\, \hat{c}_j$ and $\hat{c}_d^\dagger \hat{c}_c^\dagger \hat{c}_k \hat{c}_l$, to $|\Phi_0\rangle$. The corresponding coefficient, however, is not an independent variable in the later optimization but is approximated by a product of amplitudes $t_{ij}^{ab}\, t_{kl}^{cd}$.

Note that for convenience reasons a different normalization of the wave function is chosen in Eqs. (3.10)-(3.11)

$$\langle \Psi_{\mathrm{CC}} | \Psi_{\mathrm{CC}} \rangle \neq 1, \qquad\qquad \langle \Phi_0 | \Psi_{\mathrm{CC}} \rangle = 1. \tag{3.12}$$

In literature, this is known as *intermediate normalization*.

The order, in which excitation operators are applied to $|\Phi_0\rangle$, is irrelevant, since they all commute $[\hat{\tau}_\mu, \hat{\tau}^\nu] = 0$. Furthermore, for fermions the nilpotency of excitation operators ($\hat{\tau}_\mu \hat{\tau}_\mu = 0$) follows directly from the Pauli exclusion principle. Hence, instead of the product in Eq. (3.10), we can write

$$|\Psi_{\mathrm{CC}}\rangle = e^{\hat{T}} |\Phi_0\rangle, \qquad\qquad \text{with} \quad \hat{T} = \sum_{\mu} t_\mu \hat{\tau}_\mu. \tag{3.13}$$

The operator $\hat{T}$ is called *cluster operator*.

With the cluster operator grouped by the excitation order $\hat{T} = \hat{T}_1 + \hat{T}_2 + \hat{T}_3 + \cdots$, we illustrate how the level of truncation affects the theory. For CCD, CC singles doubles (CCSD), and CC singles doubles triples (CCSDT), we expand Eq. (3.13) and bring the sum into a CI-like form of Eq. (3.6)

$$\begin{aligned}
|\Psi_{\mathrm{CCD}}\rangle &= \left[1 \quad + \quad \hat{T}_2 \quad + \quad \tfrac{1}{2}\hat{T}_2^2 \quad + \cdots\right] |\Phi_0\rangle, \\
|\Psi_{\mathrm{CCSD}}\rangle &= \left[1 + \hat{T}_1 + \left(\hat{T}_2 + \tfrac{1}{2}\hat{T}_1^2\right) + \left(\hat{T}_2\hat{T}_1 + \tfrac{1}{6}\hat{T}_1^3\right) + \left(\tfrac{1}{2}\hat{T}_2^2 + \tfrac{1}{2}\hat{T}_2\hat{T}_1^2 + \tfrac{1}{24}\hat{T}_1^4\right) + \cdots\right] |\Phi_0\rangle, \\
|\Psi_{\mathrm{CCSDT}}\rangle &= \Bigg[1 + \underbrace{\hat{T}_1}_{\text{single,}} + \underbrace{\left(\hat{T}_2 + \tfrac{1}{2}\hat{T}_1^2\right)}_{\text{double,}} + \underbrace{\left(\hat{T}_3 + \hat{T}_2\hat{T}_1 + \tfrac{1}{6}\hat{T}_1^3\right)}_{\text{triple,}} + \underbrace{\left(\hat{T}_3\hat{T}_1 + \tfrac{1}{2}\hat{T}_2^2 + \tfrac{1}{2}\hat{T}_2\hat{T}_1^2 + \tfrac{1}{24}\hat{T}_1^4\right)}_{\text{quadruple excitations}} + \cdots\Bigg] |\Phi_0\rangle.
\end{aligned} \tag{3.14}$$

[4] There is no CC singles only as well there is no CI singles only due to Brillouin's theorem [5], which states that, starting from a HF reference, for all singly excited determinants we have $\langle \Phi_0 | \hat{H} | \Phi_i^a \rangle = 0$.

We see that, while in the CCD expansion determinants with odd number of excitations are missing, *all* possible excited determinant are included in both CCSD and CCSDT theories. As opposed to CCSD, in CCSDT triple excitations are included explicitly, which makes the theory more accurate. The above expansion converges to FCI and is equivalent to Eq. (3.6), when all possible excitations (up to N_e-fold) are included in $\hat{T}$.

CC equations

Variational treatment of the CC energy with respect to amplitudes entering $|\Psi_{CC}\rangle$ unfortunately leads to exponentially scaling computational cost [61]. Instead, CC equations are obtained by projecting the Schrödinger equation

$$\hat{H}e^{\hat{T}}|\Phi_0\rangle = E_0 e^{\hat{T}}|\Phi_0\rangle \tag{3.15}$$

onto $|\Phi_0\rangle$ and onto all excited Slater determinants $|\Phi_\mu\rangle \equiv \hat{\tau}_\mu|\Phi_0\rangle$. In this way, we obtain a set of non-linear equations for the ground state energy E_0 and the CC amplitudes t_μ. For practical reasons[5], we multiply this equation with $e^{-\hat{T}}$ before projecting it and obtain

$$\langle\Phi_0|e^{-\hat{T}}\hat{H}e^{\hat{T}}|\Phi_0\rangle = E_0, \tag{3.16}$$

$$\langle\Phi_\mu|e^{-\hat{T}}\hat{H}e^{\hat{T}}|\Phi_0\rangle = 0. \tag{3.17}$$

Eq. (3.16) is referred to as CC energy equation and Eq. (3.17) as amplitude equations. The operator

$$\bar{H} \equiv e^{-\hat{T}}\hat{H}e^{\hat{T}} \tag{3.18}$$

is called *similarity transformed* (ST) Hamiltonian. If $\hat{T}$ is not truncated, the ST Hamiltonian has the same eigenvalues as the untransformed Hamiltonian $\hat{H}$. Moreover, we see that for a complete $\hat{T}$, $\bar{H}$ has the HF reference $|\Phi_0\rangle$ as its ground state but with the exact ground-state energy E_0 . For a truncated $\hat{T}$, we basically assume that the ground state of $\bar{H}$ still has a big overlap with $|\Phi_0\rangle$ and that then Eq. (3.16) is a good estimate for the ground-state energy.

A downside of CC theory is the fact that Eq. (3.16) does not result from the variational principle Eq. (3.1) and therefore does not necessarily provide an upper bound for the true ground-state energy.

Baker-Campbell-Hausdorff expansion

By using the Baker-Campbell-Hausdorff (BCH) [62–64] formula, we can rewrite the ST Hamiltonian as a sum of nested commutators of $\hat{H}$ and $\hat{T}$

$$\bar{H} = \hat{H} + [\hat{H},\hat{T}] + \frac{1}{2!}[[\hat{H},\hat{T}],\hat{T}] + \frac{1}{3!}[[[\hat{H},\hat{T}],\hat{T}],\hat{T}] + \frac{1}{4!}[[[[\hat{H},\hat{T}],\hat{T}],\hat{T}],\hat{T}] + \cdots \tag{3.19}$$

It can be shown that, if $\hat{H}$ contains at most two-body terms, which is the case in standard quantum chemistry, the BCH always truncates at fourth order, independent of truncation level in $\hat{T}$ [61]. This means that, operator combinations that enter Eqs. (3.16)-(3.17) can be obtained analytically.

[5] With this trick, the energy equation (Eq. (3.16)) is decoupled the from amplitude equations (Eq. (3.17)). Further, we can utilize the Baker-Campbell-Hausdorff expansion (see discussion hereafter in the section).

CCSD equations

Here, we show the explicit form of CCSD equations (see e.g. [60, 61] for an explicit derivation). The energy equation (Eq. (3.16)) takes quite a simple form

$$E_{\mathrm{CCSD}} = E_{\mathrm{HF}} + \frac{1}{4}\sum_{ijab}\langle ij||ab\rangle\left(t_{ij}^{ab} + t_i^a t_j^b - t_i^b t_j^a\right), \tag{3.20}$$

with the antisymmetrized two-electron integral $\langle ij||ab\rangle$ as defined in Eq. (2.59).

Since in Eq. (3.16) we always project onto $|\Phi_0\rangle$, the amplitudes that enter the energy expression are at most doubles for any truncation level of $\hat{T}$, meaning that Eq. (3.20) remains the same also for CCSDT and for even higher orders of the theory. The particular values that enter Eq. (3.20), however, change with the truncation level of $\hat{T}$ (see Eq. (3.14)) and are related to the other amplitudes via Eq. (3.17).

In CCSD, these amplitude equations are for single-excitations

$$\begin{aligned}
\langle\Phi_i^a|\bar{H}|\Phi_0\rangle &= (\epsilon_a - \epsilon_i)t_i^a + \sum_{kc}\langle ak||ic\rangle t_k^c \\
&+ \frac{1}{2}\sum_{kcd}\langle ak||cd\rangle t_{ik}^{cd} + \sum_{kcd}\langle ak||cd\rangle t_i^a t_k^d - \frac{1}{2}\sum_{klc}\langle kl||ic\rangle t_{kl}^{ac} - \sum_{klc}\langle kl||ic\rangle t_k^a t_l^c \\
&- \frac{1}{2}\sum_{klcd}\langle kl||cd\rangle t_i^c t_{kl}^{ad} - \frac{1}{2}\sum_{klcd}\langle kl||cd\rangle t_k^a t_{il}^{cd} + \sum_{klcd}\langle kl||cd\rangle t_k^c t_{li}^{da} - \sum_{klcd}\langle kl||cd\rangle t_i^c t_k^a t_l^d \\
&= 0,
\end{aligned} \tag{3.21}$$

and for double-excitations

$$\begin{aligned}
&\langle\Phi_{ij}^{ab}|\bar{H}|\Phi_0\rangle \\
&= (\epsilon_a + \epsilon_b - \epsilon_i - \epsilon_j)t_{ij}^{ab} + \langle ab||ij\rangle + P(ij)\sum_c\langle ab||cj\rangle t_i^c - P(ab)\sum_k\langle kb||ij\rangle t_k^a \\
&+ \frac{1}{2}\sum_{kl}\langle kl||ij\rangle t_{kl}^{ab} + P(ab)\sum_{kl}\langle kl||ij\rangle t_k^a t_l^b + \frac{1}{2}\sum_{cd}\langle ab||cd\rangle t_{ij}^{cd} + \frac{1}{2}P(ij)\sum_{cd}\langle ab||cd\rangle t_i^c t_j^d \\
&+ P(ij)P(ab)\sum_{kc}\langle kb||cj\rangle t_{ik}^{ac} - P(ij)P(ab)\sum_{kc}\langle kb||ic\rangle t_k^a t_j^c \\
&+ \frac{1}{2}P(ij)\sum_{klc}\langle kl||cj\rangle t_i^c t_{kl}^{ab} - P(ij)\sum_{klc}\langle kl||ci\rangle t_k^c t_{lj}^{ab} \\
&+ P(ij)P(ab)\sum_{klc}\langle kl||ic\rangle t_l^a t_{jk}^{bc} + \frac{1}{2}P(ij)P(ab)\sum_{klc}\langle kl||cj\rangle t_i^c t_k^a t_l^b \\
&- \frac{1}{2}P(ab)\sum_{kcd}\langle kb||cd\rangle t_k^a t_{ij}^{cd} + P(ab)\sum_{kcd}\langle ka||cd\rangle t_k^c t_{ij}^{db} \\
&+ P(ij)P(ab)\sum_{kcd}\langle ak||dc\rangle t_i^d t_{jk}^{bc} - \frac{1}{2}P(ij)P(ab)\sum_{kcd}\langle kb||cd\rangle t_i^c t_k^a t_l^d \\
&+ \frac{1}{4}\sum_{klcd}\langle kl||cd\rangle t_{ij}^{cd} t_{ij}^{ab} + \frac{1}{4}P(ij)\sum_{klcd}\langle kl||cd\rangle t_i^c t_j^d t_{ij}^{ab} + \frac{1}{4}P(ab)\sum_{klcd}\langle kl||cd\rangle t_k^a t_l^b t_{ij}^{cd} \\
&- \frac{1}{2}P(ij)\sum_{klcd}\langle kl||cd\rangle t_{ik}^{ab} t_{jl}^{cd} - \frac{1}{2}P(ab)\sum_{klcd}\langle kl||cd\rangle t_{ij}^{ac} t_{kl}^{bd} + \frac{1}{2}P(ij)P(ab)\sum_{klcd}\langle kl||cd\rangle t_{ik}^{ac} t_{lj}^{db} \\
&- P(ij)\sum_{klcd}\langle kl||cd\rangle t_k^c t_i^d t_{lj}^{ab} - P(ab)\sum_{klcd}\langle kl||cd\rangle t_k^c t_l^a t_{ij}^{db} + P(ij)P(ab)\sum_{klcd}\langle kl||cd\rangle t_i^c t_l^b t_{kj}^{ad} \\
&+ \frac{1}{4}P(ij)P(ab)\sum_{klcd}\langle kl||cd\rangle t_i^c t_j^d t_k^a t_l^b = 0.
\end{aligned} \tag{3.22}$$

Above, we have used a permutation operator P, which is defined as

$$P(ij)f(i,j) \equiv f(i,j) - f(j,i). \tag{3.23}$$

These algebraic equations are quite cumbersome, but they can be formulated in a more compact and elegant form with diagrammatic techniques. Further, they are non-linear in the amplitudes and are therefore solved through iterative root-finding algorithms. The CC energy is then obtained from Eq. (3.20).

Scaling

The scaling of the theory depends on the truncation level of $\hat{T}$. We can relate the overall scaling of the theory to evaluation of the most expensive term in Eq. (3.21) or Eq. (3.22). Assuming that the number of occupied spin-orbitals N_{occ} is much smaller than the number of empty spin-orbitals N_{emp}, we can identify $\frac{1}{2}\sum_{cd}\langle ab||cd\rangle t_{ij}^{cd}$ as most expensive linear term in Eqs. (3.21)-(3.22), since it contains four empty-orbital labels. The computational cost for this term is proportional to $N_{\text{emp}}^4 \cdot N_{\text{occ}}^2$ for each iteration.

Although quadratic terms such as $\frac{1}{4}\sum_{klcd}\langle kl||cd\rangle t_{ij}^{cd} t_{ij}^{ab}$ have more indices to contract, they can be summed in stages [60] and do not increase the overall scaling of the methods. Hence, CCSD scales, roughly speaking, as N^6. Note that the same term would also appear in CCD equations. Therefore, CCD has the same scaling as CCSD[6]. CCSDT, on the contrary, scales as N^8 due to the expensive evaluation of connected triples and is therefore considered too computationally demanding for practical implementations [60].

The optimal trade-off between accuracy and computational cost for the ground state properties is achieved in CCSD with perturbative triples (CCSD(T)) [15]. There, a standard CCSD computation (which scales as N^6) is performed and triple excitations are added in a perturbative fashion afterwards through a single (non-iterative) step that scales as N^7.

Excited states in CC theory

Treatment of excited states in CC theory is not as straightforward as in CI approaches, since the operator that is diagonalized in a chosen subset of Slater determinants is not the original Hamiltonian but its ST version defined in Eq. (3.18). A simple CI-like strategy is utilized by the equation-of-motion coupled-cluster (EOM-CC) approach [65] that we introduce in the following.

The starting point of EOM-CC ansatz is the Schrödinger equation for an excited state

$$\hat{H}|\Psi_k\rangle = E_k|\Psi_k\rangle. \tag{3.24}$$

In general, the state $|\Psi_k\rangle$ can be build by applying an excitation operator $\hat{\mathscr{R}}_k$ (consisting of all(!) possible excitations) to the ground-state $|\Psi_0\rangle$.

In EOM-CC, the ground state of the system is approximated by the CC ground state and the operator $\hat{\mathscr{R}}_k$ is truncated at the same level as cluster operator $\hat{T}$ of the ground-state theory

$$\hat{\mathscr{R}}_k = \sum_{\mu} r_{k,\mu}\hat{\tau}_\mu. \tag{3.25}$$

Hence, for an excited state we write

$$|\Psi_k^{\text{CC}}\rangle = \hat{\mathscr{R}}_k|\Psi_0^{\text{CC}}\rangle = e^{\hat{T}}\hat{\mathscr{R}}_k|\Phi_0\rangle. \tag{3.26}$$

And Eq. (3.24) additionally multiplied by $e^{-\hat{T}}$ becomes

$$e^{-\hat{T}}\hat{H}e^{\hat{T}}\hat{\mathscr{R}}_k|\Phi_0\rangle = \bar{H} = E_k\hat{\mathscr{R}}_k|\Phi_0\rangle. \tag{3.27}$$

[6] The scaling behavior of e.g. CISD is estimated in the same manner.

Equation above is nothing but a linear equation determining the coefficients $r_{k,\mu}$ that enter $\hat{\mathscr{R}}_k$. Put differently, we have to diagonalize the ST Hamiltonian in the subspace of excited determinants entering the theory.

Since the ST Hamiltonian is not hermitian, it has different left and right eigenvectors. Hence, within EOM-CC theory we obtain a bi-orthonormal set of eigenvectors that approximate excited states of the system. They are determined by the following set of equations

$$\bar{H}\hat{\mathscr{R}}_k = E_k\hat{\mathscr{R}}_k, \tag{3.28}$$

$$\hat{\mathscr{L}}_j\bar{H} = \hat{\mathscr{L}}_j E_j, \tag{3.29}$$

$$\hat{\mathscr{L}}_j\hat{\mathscr{R}}_k = \delta_{jk}\mathbb{1}. \tag{3.30}$$

The right excited states are given by Eq. (3.26) and the left eigenstates accordingly by

$$\langle\tilde{\Psi}_j^{\mathrm{CC}}| = \langle\Phi_0|e^{-\hat{T}}\hat{\mathscr{L}}_j. \tag{3.31}$$

The tilde emphasizes the fact that left and right eigenvectors are not hermitian conjugates of each other $\langle\tilde{\Psi}_j^{\mathrm{CC}}| \neq \left(|\Psi_j^{\mathrm{CC}}\rangle\right)^\dagger$.

In terms of left and right eigenstates, expectation values of operators and transition moments are in general approximated as [65]

$$\langle\Psi_i|\hat{O}|\Psi_i\rangle \approx \langle\tilde{\Psi}_i^{\mathrm{CC}}|\hat{O}|\Psi_i^{\mathrm{CC}}\rangle, \tag{3.32}$$

$$|O_{ij}|^2 = |\langle\Psi_i|\hat{O}|\Psi_j\rangle|^2 \approx \langle\tilde{\Psi}_j^{\mathrm{CC}}|\hat{O}|\Psi_i^{\mathrm{CC}}\rangle\langle\tilde{\Psi}_i^{\mathrm{CC}}|\hat{O}|\Psi_j^{\mathrm{CC}}\rangle. \tag{3.33}$$

The EOM-CC formalism provides a simple approach to excited states of a system in the framework of CC theory. This method is able to describe correlated excited states and has the same scaling as the underlying ground-state theory [66]. A disadvantage of EOM-CC is that it looses size-extensivity for excited states [67].

3.1.4 Other honorable mentions

All of the methods introduced in this section perform well, when one Slater determinant is enough to cover the coarse electronic structure of the system. There are systems, however, where this is not the case, examples being stretched molecular bonds [58]. This type of correlations are referred to as *static correlations* and we briefly introduce some popular approaches to deal with such situations below.

The most prominent method in quantum chemistry to address static correlations is multi-configurational self-consistent field (MCSCF) [68], which is a multi-configurational extension of HF theory. There, HF-orbitals are optimized such that not only one Slater determinant but a sum of selected Slater determinants has the lowest energy.

Another group of approaches addressing static correlations in a similar spirit are multi-reference methods. These methods use more than one Slater determinant as the starting point for the expansion of the wave function, e.g. multi-reference CI [69] and multi-reference CC [15] methods.

An entirely different strategy to handle strong correlations is given by DMRG [16]. This variational approach is based on an alternative representation of the wave function, namely as a matrix product state. This method provides very accurate results for systems with short-range interactions and long-range correlations, such as the Hubbard model [70] and is therefore widely used in solid-state physics. Although, by construction, it is mostly suited to describe one-dimensional systems, it has also been successfully applied for *ab initio* studies of molecules [71]. The scaling of DMRG is polynomial but it also strongly depends on the considered system. For most realistic systems this method is often very expensive.

3.2 Density functional theory

In this section, we outline the concepts of DFT [72], a functional theory that uses the ground-state electronic density as the key variable.

Considering for simplicity a non-degenerate ground state of a closed-shell N_e-electron system[7], we define its spatial distribution of electrons, its *electronic density*, as

$$n(\boldsymbol{r}) = N_\mathrm{e} \int d\boldsymbol{x}_{N_\mathrm{e}} \cdots \int d\boldsymbol{x}_2 \int d\chi \;\; \Psi_0^*\left(\boldsymbol{x}, \boldsymbol{x}_2, \cdots, \boldsymbol{x}_{N_\mathrm{e}}\right) \Psi_0\left(\boldsymbol{x}, \boldsymbol{x}_2, \cdots, \boldsymbol{x}_{N_\mathrm{e}}\right), \tag{3.34}$$

where by $\boldsymbol{x}$ we again denote the combined space and spin index $(\boldsymbol{r}, \chi)$.

DFT is based on the Hohenberg-Kohn (HK) theorem [8], which states that, for a fixed interaction $\hat{W}$, there is a one-to-one correspondence between the external potential $v_\mathrm{ext}(\boldsymbol{r})$ of a given system and its ground-state wave function $|\Psi_0\rangle$, as well as there is a one-to-one correspondence between the ground-state wave function of this system and its ground-state electronic density

$$v_\mathrm{ext}(\boldsymbol{r}) \xleftrightarrow{\text{1:1}} |\Psi_0\rangle \xleftrightarrow{\text{1:1}} n(\boldsymbol{r}). \tag{3.35}$$

From the HK theorem we conclude that all ground-state properties of a many-body system are uniquely determined by its ground state-density

$$|\Psi_0\rangle = |\Psi_0[n]\rangle \;\Rightarrow\; \langle\hat{O}\rangle = \langle\Psi_0|\hat{O}|\Psi_0\rangle = \langle\hat{O}\rangle[n]. \tag{3.36}$$

Especially for the energy we write

$$\begin{aligned} E[n] &= \langle\Psi_0[n]|\hat{H}|\Psi_0[n]\rangle = \langle\Psi_0[n]|\hat{T} + \hat{V} + \hat{W}|\Psi_0[n]\rangle \\ &= T[n] + W[n] + \int d\boldsymbol{r}\, v_\mathrm{ext}(\boldsymbol{r}) n(\boldsymbol{r}). \end{aligned} \tag{3.37}$$

From this formulation follows:

1. the energy functional has its minimum at the ground-state density of the system,
2. the functionals $T[n]$ and $W[n]$ are *universal* functionals of the density.

Therefore, knowing the functional form of $T[n]$ and $W[n]$ exactly would remove the necessity of solving the Schrödinger equation to obtain the ground-state energy of a system. Unfortunately, the exact functionals remain (and most certainly will remain) unknown and have to be approximated for practical calculations. Specifically, the kinetic energy contribution $T[n]$ is the most difficult part and all direct approximations are so far insufficient [73].

3.2.1 Kohn-Sham DFT

There is a method to indirectly approximate $T[n]$. This is done by means of Kohn-Sham (KS) DFT [9]. The KS construction is based on the HK theorem, from which follows that for any interacting system there exists one and only one auxiliary non-interacting system with a local potential $v_\mathrm{KS}(\boldsymbol{r})$, which has the same ground-state density. The potential $v_\mathrm{KS}(\boldsymbol{r})$ is called KS potential.

Based on this connection, the ground-state density of an interacting system is found by solving the one-body KS eigenvalue equations

$$\left(-\frac{\nabla^2}{2} + v_\mathrm{KS}(\boldsymbol{r})\right)\varphi_j^\mathrm{KS}(\boldsymbol{r}) = \varepsilon_j \varphi_j^\mathrm{KS}(\boldsymbol{r}). \tag{3.38}$$

[7] DFT itself is not restricted to such systems.

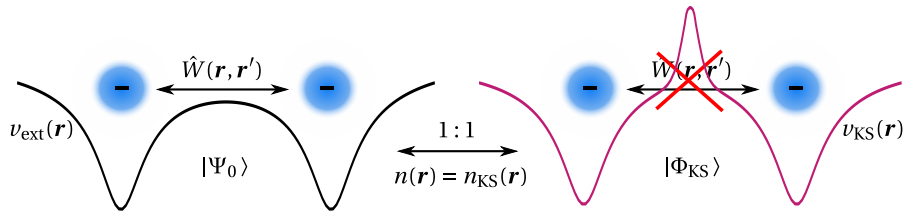

Figure 3. Visualization of the Kohn-Sham construction in DFT: The electronic density $n(\boldsymbol{r})$ of an interacting system in an external potential $v_{\text{ext}}(\boldsymbol{r})$ can be uniquely reproduced by a non-interacting system in a different external potential $v_{\text{KS}}(\boldsymbol{r})$.

The ground state of the auxiliary KS system is given by a Slater determinant $|\Phi_{\text{KS}}\rangle$ built from spatial orbitals $\varphi_i^{\text{KS}}(\boldsymbol{r})$ and the density of both interacting and non-interacting system is obtained via

$$n(\boldsymbol{r}) = 2\sum_{j=1}^{N_e/2} |\varphi_j^{\text{KS}}(\boldsymbol{r})|^2. \tag{3.39}$$

The kinetic energy of the non-interacting KS system is obtained in a straight-forward manner

$$T_{\text{KS}}[n] = -\sum_{j=1}^{N_e/2} \int d\boldsymbol{r}\, \varphi_j^{\text{KS}*}(\boldsymbol{r}) \left[\frac{\nabla_{\boldsymbol{r}}^2}{2} \varphi_j^{\text{KS}}(\boldsymbol{r})\right]. \tag{3.40}$$

We now can rewrite Eq. (3.37) as

$$E[n] = T_{\text{KS}}[n] + \underbrace{(T[n] - T_{\text{KS}}[n] + W[n])}_{E_{\text{Hxc}}[n]} + \int d\boldsymbol{r}\, v_{\text{ext}}(\boldsymbol{r}) n(\boldsymbol{r}), \tag{3.41}$$

where we have found an explicit expression for a big portion of the kinetic energy contributions. The remaining kinetic correlations and electron-electron interactions are summarized in the *Hartree exchange-correlation* (Hxc) energy functional $E_{\text{Hxc}}[n]$, which is the term that is usually approximated in KS DFT. This functional can be further decomposed into a part accounting for classical electrostatic interactions (Hartree) and the rest (exchange-correlation)

$$E_{\text{Hxc}}[n] = \underbrace{\int d\boldsymbol{r} \int d\boldsymbol{r}'\, n(\boldsymbol{r}) W(\boldsymbol{r},\boldsymbol{r}') n(\boldsymbol{r}')}_{E_{\text{H}}[n]} + E_{\text{xc}}[n]. \tag{3.42}$$

Correspondingly, the difference between the KS potential and the external potential is called the Hxc potential $v_{\text{Hxc}}[n](\boldsymbol{r})$ and can be connected to the Hxc energy functional via

$$v_{\text{KS}}[n, v_{\text{ext}}](\boldsymbol{r}) - v_{\text{ext}}(\boldsymbol{r}) \equiv v_{\text{Hxc}}[n](\boldsymbol{r}) = \frac{\delta E_{\text{Hxc}}[n]}{\delta n} = \int d\boldsymbol{r}' W(\boldsymbol{r},\boldsymbol{r}') n(\boldsymbol{r}') + \frac{\delta E_{\text{xc}}[n]}{\delta n} \tag{3.43}$$

$$\equiv v_{\text{H}}[n] + v_{\text{xc}}[n]. \tag{3.44}$$

In KS DFT, the set of equations (Eq. (3.38) and Eq. (3.39)) has to be solved self-consistently, while updating $v_{\text{Hxc}}[n](\boldsymbol{r})$ for each step. For an explicit energy functional, the potential is constructed via Eq. (3.43). Starting with an initial guess for e.g. a KS potential v_{KS} we obtain a first guess for the ground-state density $n^{(0)}$. From this a new Hxc potential $v_{\text{Hxc}}[n^{(0)}]$ and a new KS potential are constructed. Then, the KS equations are solved again in order to obtain a new density $n^{(1)}$. This procedure is repeated until convergence.

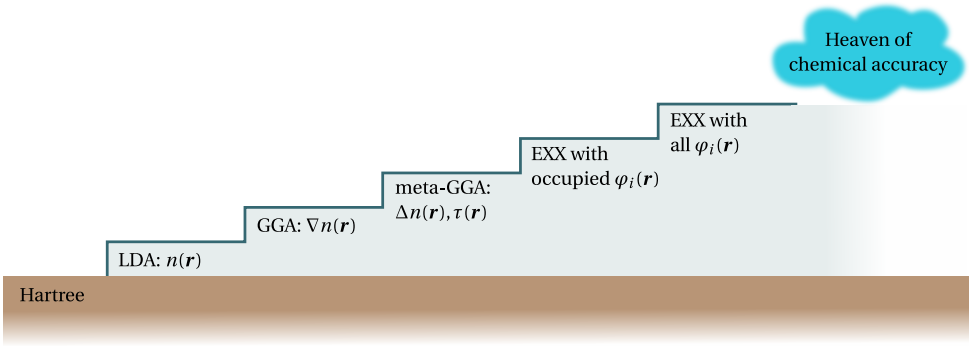

Figure 4. Jacob's ladder of functional approximations in DFT, adapted from [74].

3.2.2 Energy-functional approximations

Over last decades, a wide range of approximations to the functional form of $E_{\mathrm{Hxc}}[n](\boldsymbol{r})$ with different levels of complexity and corresponding accuracy has been developed.

Generally, we can write the xc energy functional as

$$E_{\mathrm{xc}}[n] = \int d\boldsymbol{r} \epsilon_{\mathrm{xc}}([n];\boldsymbol{r})\, n(\boldsymbol{r}), \tag{3.45}$$

with the xc energy density ϵ_{xc} that depends on the full density distribution in space. This dependence can be expanded as

$$\epsilon_{\mathrm{xc}}([n];\boldsymbol{r}) = \epsilon_{\mathrm{xc}}\big(n(\boldsymbol{r}), \nabla n(\boldsymbol{r}), \Delta n(\boldsymbol{r}), \cdots\big), \tag{3.46}$$

The simplest approximation for $E_{\mathrm{xc}}[n]$ is known as the local density approximation (LDA) [9]. There ϵ_{xc} is assumed to depend only locally on the density and its explicit form is taken from a homogeneous electron gas

$$E_{\mathrm{xc}}^{\mathrm{LDA}}[n] = \int d\boldsymbol{r} \epsilon_{\mathrm{xc}}^{\mathrm{HEG}}(n(\boldsymbol{r}))\, n(\boldsymbol{r}). \tag{3.47}$$

More accurate approximations are those, where not only the density but also its gradient at a point in space are taken into account. They build a range of general gradient approximations (GGAs) [75], with Perdew-Burke-Ernzerhof (PBE) functional [10] being the most famous. Within meta-GGAs higher derivatives of the density and in some cases orbital-dependent quantities such the kinetic energy density $\tau(\boldsymbol{r})$ are included (e.g. VS98 [76] or PKZB [77]). The next level of accuracy is reached by including exact exchange (EXX) energy contributions to the xc energy approximations of LDA, GGA or meta-GGA. EXX is calculated from occupied orbitals and therefore the functionals become orbital-dependet. Examples are hybrid functionals such as B3LYP [75, 78, 79] and PBE0 [80]. By including all KS orbitals into the calculation of EXX we reach the last set of functionals, where functionals based on the random-phase approximation (RPA) [81] are the best known examples. The outlined hierarchy is known as Jacob's ladder of density functional approximations [74] (see Fig. 4). Very good summaries on this topic can be found in e.g. the original paper of Perdew *et al* [74] and a more recent literature [11].

3.2.3 Limitations of standard DFT

Despite its efficiency, there are still open issues in standard DFT that need to be addressed. From a formal perspective, it has been shown that the exact functionals are not functionally differentiable [82] and therefore regularizations need to be done [83]. Further, in contrast to wave-function methods, where results can be improved by increasing the number of single-particle

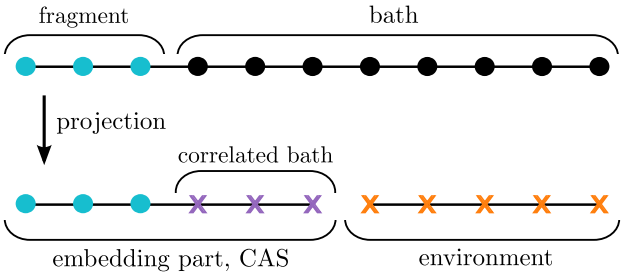

Figure 5. Visualization of the decomposition of the system into fragment and bath and the projection onto embedding (CAS) and environment part. The dots depict the sites, which correspond to our chosen initial basis set and the crosses the orbitals after projecting. In order to describe the physics of the fragment only the embedding part is considered. Graphic was originally published in [88].

orbitals or by including higher excitations, there is no systematic way on how to increase the accuracy of a chosen functional approximation. Additionally, there is the often overlooked but important issue of how to construct other observables from the KS Slater determinant, since any observable that cannot be expressed directly in terms of the density needs to be approximated in terms of the latter.

From an application perspective, we need to mention that, although significant progress in functional development over the years has been achieved, approximate DFT functionals usually still struggle to describe systems with strongly correlated electrons [13]. Dissociation of the H_2 molecule is a good example for a simple situation, which commonly used approximate DFT functionals fail to describe correctly.

3.3 Density-matrix embedding theory

Density-matrix embedding theory [20–22] is a simple quantum embedding scheme for fragments that are strongly coupled to the rest of the system. In such situation, the rest of the system cannot be mimicked by a simple external potential as e.g. is usually done in DFT embedding [54, 84–87]. It rather has to be interpreted as a *bath* to which an *open* quantum system (the fragment) is coupled. The DMET method provides an algorithm to reduce the full bath to a small set of orbitals (*correlated bath*) that effectively describe correlations between fragment and rest of the system (see Fig. 5 for a visualization).

In DMET, single particle orbitals of the Fock space are divided into two groups: N_{frag} spatial orbitals that belong to fragment A (a.k.a. impurity) and $(N-N_{\text{frag}})$ spatial orbitals that belong to the rest of the system B, which we call bath. Without loss of generality, we assume $N_{\text{frag}} \leq N/2$. For a real-space-grid basis this corresponds to spatial separation and is easy to visualize (see Fig. 5). For the subsequent discussion we further assume that the fragment consists of the first N_{frag} sites.

Any wave function in the full Fock space can be decomposed as

$$|\Psi\rangle = \sum_{i}^{4^{N_{\text{frag}}}} \sum_{j}^{4^{(N-N_{\text{frag}})}} \Psi_{ij} |A_i\rangle \otimes |B_j\rangle. \tag{3.48}$$

The object Ψ_{ij} is a $4^{N_{\text{frag}}} \times 4^{(N-N_{\text{frag}})}$-matrix that we can rewrite by using its singular-value decomposition (SVD) (see Fig. 6)

$$\Psi_{ij} = \sum_{\alpha}^{4^{N_{\text{frag}}}} \mathcal{U}_{i\alpha} \Lambda_{\alpha} \mathcal{V}^{\dagger}_{\alpha j}. \tag{3.49}$$

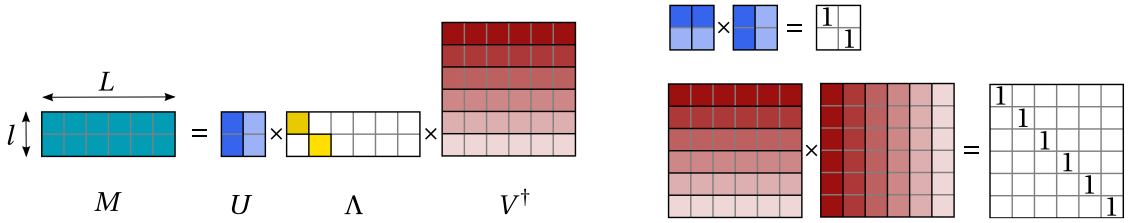

Figure 6. Visualization of singular-value decomposition of a $l \times L$-dimensional matrix M. It has l left-singular vectors that build the columns of an $l \times l$-dimensional matrix U and L right-singular vectors that are contained in an $L \times L$-dimensional matrix V. Singular vectors are normalized, meaning $U \cdot U^\dagger = \mathbb{1}_{l\times l}$ and $V \cdot V^\dagger = \mathbb{1}_{L\times L}$. The matrix M has l singular values that build the diagonal of Λ.

The matrix $\mathscr{U}$ consist of left-singular vectors and the $\mathscr{V}$ of right-singular vectors to the singular values Λ_α. With Eq. (3.49) we rewrite the wave function as

$$\begin{aligned} |\Psi\rangle &= \sum_{\alpha}^{4^{N_\mathrm{frag}}} \Lambda_\alpha \left(\sum_{i}^{4^{N_\mathrm{frag}}} \mathscr{U}_{i\alpha} |A_i\rangle \right) \otimes \left(\sum_{j}^{4^{(N-N_\mathrm{frag})}} \mathscr{V}^\dagger_{\alpha j} |B_j\rangle \right), \\ &= \sum_{\alpha}^{4^{N_\mathrm{frag}}} \Lambda_\alpha |\widetilde{A}_\alpha\rangle \otimes |\widetilde{B}_\alpha\rangle. \end{aligned} \tag{3.50}$$

With this reformulation we see that the number of many-body states in B that contribute to the wave function boils down to the size of the fragment Fock space.

3.3.1 Single-particle projection

The reformulation in Eq. (3.50) is interesting but, for the time being, of no practical use for a general $|\Psi\rangle$, since the new basis consists of unknown many-body states for which we would have to solve the Schrödinger equation in order to obtain them. However, if the wave function of interest is a Slater determinant, we can relate the SVD to a simple basis transformation. Here, we follow the derivation from [89].

The ground-state wave function of a single-particle Hamiltonian $\hat{h}$ is given by

$$|\Phi\rangle = \prod_{k=1}^{N_\mathrm{e}} \hat{\psi}^\dagger_k |0\rangle = \prod_{k=1}^{N_\mathrm{e}} \sum_{i=1}^{2N} C_{ik} \hat{c}^\dagger_i |0\rangle, \tag{3.51}$$

where operators $\psi^\dagger_k$ create particles in corresponding spin-orbitals that are obtained by diagonalizing $\hat{h}$. The numbers C_{ik} are values of corresponding spin-orbitals on the real-space grid. Note that for each site we have two possible spin configurations and, therefore, there are $2N$ basis states in total in the original basis. We summarize the coefficients C_{ik} in the following matrix

$$C = \underbrace{\begin{pmatrix} \varphi_1(1) & \cdots & \varphi_k(1) & \cdots & \varphi_{N_\mathrm{e}/2} \\ \vdots & & \vdots & & \vdots \\ \varphi_1(j) & \cdots & \varphi_k(j) & \cdots & \varphi_{N_\mathrm{e}/2}(j) \\ \vdots & & \vdots & & \vdots \\ \varphi_1(N) & \cdots & \varphi_k(N) & \cdots & \varphi_{N_\mathrm{e}/2}(N) \end{pmatrix}}_{\equiv C_\varphi} \otimes \begin{pmatrix} |\uparrow\rangle & 0 \\ 0 & |\downarrow\rangle \end{pmatrix}. \tag{3.52}$$

Here again, we assume even particle number N_e and therefore have $N_\mathrm{e}/2$ spatial orbitals φ_k occupied by one spin-up and one spin-down electron, respectively. We further assume $4N_\mathrm{frag} \leq N_\mathrm{e}$ for the subsequent derivation.

As a next step, we consider a transformation of spatial orbitals into a new set of orbitals: $2N_{\text{frag}}$ orbitals that do have entries on the fragment and the remaining $N-2N_{\text{frag}}$ orbitals that do not. This is done by performing a SVD on a fragment submatrix C_φ^A of C_φ

$$C_\varphi = \left(\begin{array}{ccc} \bullet & \varphi_k(1) & \bullet \\ \vdots & \vdots & \vdots \\ \vdots & \varphi_k(N_{\text{frag}}) & \vdots \\ \hline \vdots & \varphi_k(N_{\text{frag}}+1) & \vdots \\ \vdots & \vdots & \vdots \\ \bullet & \varphi_k(N) & \bullet \end{array}\right) \equiv \left(\begin{array}{c} C_\varphi^A \\ \hline C_\varphi^B \end{array}\right) = \left(\begin{array}{c} U_A \cdot \lambda \cdot V_A^\dagger \\ \hline C_\varphi^B \end{array}\right). \tag{3.53}$$

The matrices U_A ($N_{\text{frag}} \times N_{\text{frag}}$) and V_A ($N_e/2 \times N_e/2$) contain left- and right-singular vectors of C_φ^A (see Fig. 6 for visualization). Rotating the coefficient matrix C_φ with V_A results in

$$\widetilde{C}_\varphi = C_\varphi \cdot V_A = \left(\begin{array}{c|c} U_A \cdot \lambda & \mathbb{O} \\ \hline C_\varphi^B \cdot V_A & \end{array}\right) \qquad \text{and} \quad \widetilde{C} = \widetilde{C}_\varphi \otimes \begin{pmatrix} |\uparrow\rangle & 0 \\ 0 & |\downarrow\rangle \end{pmatrix}. \tag{3.54}$$

Here, $\mathbb{O}$ denotes a $N_{\text{frag}} \times (N_e/2 - N_{\text{frag}})$-dimensional matrix consisting of only zeros. Through the rotation the first N_{frag} spatial orbitals in $\widetilde{C}_\varphi$ have entries on all sites and we call them complete active space (CAS) or embedding orbitals. The remaining $N_e/2 - N_{\text{frag}}$ orbitals only have entries on the bath. Those we call environment orbitals. In terms of spin-orbitals in $\widetilde{C}$ we now have $2N_{\text{frag}}$ spin-orbitals in CAS and $N_e - 2N_{\text{frag}}$ orbitals in the environment.

We can equivalently rewrite the Slater determinant defined in Eq. (3.51) in terms of the new spin-orbitals in $\widetilde{C}$ as

$$|\Phi\rangle = \prod_{k=1}^{N_e} \sum_{i=1}^{2N} \widetilde{C}_{ik} \hat{c}_i^\dagger |0\rangle = \underbrace{\prod_{k=1}^{2N_{\text{frag}}} \sum_{i=1}^{2N} \widetilde{C}_{ik} \hat{c}_i^\dagger}_{\text{orbitals on } A+B} \underbrace{\prod_{k=(2N_{\text{frag}}+1)}^{N_e} \sum_{i=(2N_{\text{frag}}+1)}^{2N} \widetilde{C}_{ik} \hat{c}_i^\dagger}_{\text{orbitals solely on } B} |0\rangle \tag{3.55}$$

$$= \prod_{k=1}^{2N_{\text{frag}}} \left(\underbrace{\sum_{i=1}^{2N_{\text{frag}}} \widetilde{C}_{ik} \hat{c}_i^\dagger}_{\equiv \widetilde{C}_k^A \hat{a}_k^\dagger} + \underbrace{\sum_{i=(2N_{\text{frag}}+1)}^{2N} \widetilde{C}_{ik} \hat{c}_i^\dagger}_{\equiv \widetilde{C}_k^B \hat{b}_k^\dagger} \right) \prod_{k=(2N_{\text{frag}}+1)}^{N_e} \underbrace{\sum_{i=(2N_{\text{frag}}+1)}^{2N} \widetilde{C}_{ik} \hat{c}_i^\dagger}_{\equiv \widetilde{C}_k^B \hat{b}_k^\dagger} |0\rangle \tag{3.56}$$

$$= \prod_{k=1}^{2N_{\text{frag}}} \left(\widetilde{C}_k^A \hat{a}_k^\dagger + \widetilde{C}_k^B \hat{b}_k^\dagger \right) \prod_{k=(2N_{\text{frag}}+1)}^{N_e} \widetilde{C}_k^B \hat{b}_k^\dagger \; |0\rangle. \tag{3.57}$$

We have defined (properly re-normalized on the respective Fock-subspaces of A and B) operators that create particles in orbitals whose entries are either purely on the fragment ($\hat{a}_k^\dagger$) or purely on the bath ($\hat{b}_k^\dagger$)

$$\hat{a}_k^\dagger = \frac{1}{\sqrt{\sum_{i=1}^{2N_{\text{frag}}} |\widetilde{C}_{ik}|^2}} \sum_{i=1}^{2N_{\text{frag}}} \widetilde{C}_{ik} \hat{c}_i^\dagger, \qquad \widetilde{C}_k^A = \sqrt{\sum_{i=1}^{2N_{\text{frag}}} |\widetilde{C}_{ik}|^2}, \tag{3.58}$$

$$\hat{b}_k^\dagger = \frac{1}{\sqrt{\sum_{i=(2N_{\text{frag}}+1)}^{2N} |\widetilde{C}_{ik}|^2}} \sum_{i=(2N_{\text{frag}}+1)}^{2N} \widetilde{C}_{ik} \hat{c}_i^\dagger \qquad \widetilde{C}_k^B = \sqrt{\sum_{i=(2N_{\text{frag}}+1)}^{2N} |\widetilde{C}_{ik}|^2}. \tag{3.59}$$

If we would explicitly rewrite the two products in Eq. (3.57) as a single sum, we could relate individual terms to the many-body states in Eq. (3.50).

The crucial point to make here, however, is that we can identify one fixed part in every many-body state in the expansion Eq. (3.57) and therefore also in Eq. (3.50), namely

$$\prod_{k=(2N_{\text{frag}}+1)}^{N_e} \tilde{C}_k^B \hat{b}_k^\dagger \quad |0\rangle \equiv |\tilde{0}\rangle. \tag{3.60}$$

This part is unimportant for the behavior of the fragment and can therefore be understood as a *new vacuum* $|\tilde{0}\rangle$. For the Slater determinant we then can simply write

$$|\Phi\rangle = \prod_{k=1}^{2N_{\text{frag}}} \left(\tilde{C}_k^A \hat{a}_k^\dagger + \tilde{C}_k^B \hat{b}_k^\dagger\right) |\tilde{0}\rangle. \tag{3.61}$$

In this way, we have removed $N_e - 2N_{\text{frag}}$ (spatial) environmental orbitals from the Fock space and can now consider a lower dimensional Fock space built from $2N_{\text{frag}}$ spatial CAS orbitals in order to describe the fragment.

In practice, the fragment part of CAS-orbitals ($\tilde{C}_k^A$) is rotated back such that the orignal basis of the fragment (real-space sites) is restored (also depicted in Fig. 5). We call the transformation of the original basis into the CAS and the environment basis and subsequent removal the environment orbitals *single-particle projection P*, which for spatial orbitals is a $N \times 2N_{\text{frag}}$-dimensional matrix

$$P = \left(\begin{array}{c|ccc} \mathbb{1}_{N_{\text{frag}} \times N_{\text{frag}}} & \multicolumn{3}{c}{\mathbb{0}_{N_{\text{frag}} \times N_{\text{frag}}}} \\ \hline \mathbb{0}_{(N-N_{\text{frag}}) \times N_{\text{frag}}} & \tilde{\varphi}_1^B(N_{\text{frag}}+1) & \cdots & \tilde{\varphi}_{N_{\text{frag}}}^B(N_{\text{frag}}+1) \\ & \vdots & \ddots & \vdots \\ & \tilde{\varphi}_1^B(N) & \cdots & \tilde{\varphi}_{N_{\text{frag}}}^B(N) \end{array}\right). \tag{3.62}$$

Usually, this matrix is obtained from the one-body reduced density matrix (1RDM), whose matrix elements are define as

$$\gamma_{ij} = \langle\Phi|\hat{c}_{i\uparrow}^\dagger \hat{c}_{j\uparrow} + \hat{c}_{i\downarrow}^\dagger \hat{c}_{j\downarrow}|\Phi\rangle = 2\sum_{k=1}^{N_e/2} \tilde{\varphi}_k^*(i)\tilde{\varphi}_k(j) = 2\sum_{k=1}^{N_{\text{frag}}} \tilde{\varphi}_k^*(i)\tilde{\varphi}_k(j) + 2\sum_{k=(N_{\text{frag}}+1)}^{N_e/2} \tilde{\varphi}_k^*(i)\tilde{\varphi}_k(j). \tag{3.63}$$

If we now separate the 1RDM as

$$\gamma = \left(\begin{array}{c|c} \gamma^{\text{A}} & \gamma^{\text{A-B}} \\ \hline \gamma^{\text{A-B}\dagger} & \gamma^{\text{B}} \end{array}\right) \tag{3.64}$$

and calculate γ^{B} explicitly

$$\gamma^{\text{B}} = 2\sum_{k=1}^{N_{\text{frag}}} \|\tilde{C}_k^B\|^2 \tilde{\varphi}_k^{B*}(i)\tilde{\varphi}_k^B(j) + 2\sum_{k=(N_{\text{frag}}+1)}^{N_e/2} \tilde{\varphi}_k^*(i)\tilde{\varphi}_k(j), \tag{3.65}$$

with $\tilde{C}_k^B$ as defined in Eq. (3.59), we see that correlated-bath orbitals can be obtained simply by diagonalizing γ^{B}. There are N_{frag} orbitals with eigenvalues $\tilde{\lambda}_k = 2\|\tilde{C}_k^B\|^2 < 2$ and exactly those are the correlated-bath orbitals.

3.3.2 Embedding interacting system

In general, the ground-state wave function of an interacting problem is a superposition of all basis states (Slater determinants) of the Hilbert space

$$|\Psi\rangle = \sum_{\alpha=1}^{\binom{2N}{N_e}} \Psi_\alpha |\Phi_\alpha\rangle = \sum_{\alpha=1}^{\binom{2N}{N_e}} \Psi_\alpha \left[\prod_{k=1}^{N_e} \hat{\psi}_k^\dagger\right]_\alpha |0\rangle, \tag{3.66}$$

where the basis states $|\Phi_\alpha\rangle$ are build from all possible N_e-fold products of operators $\hat{\psi}_k^\dagger$, that create particles in one of the $2N$ spin-orbitals. We denote these combinations by $[\ldots]_\alpha$.

In DMET, this expansion is reduced to the set of CAS orbitals that we have obtained from a single Slater determinant in the previous section

$$\left\{\hat{\psi}_k^{\dagger\mathrm{CAS}}\right\} = \left\{\left\{\tilde{C}_k^A \hat{a}_{k\sigma}^\dagger\right\}, \left\{\tilde{C}_k^B \hat{b}_{k\sigma}^\dagger\right\}\right\}, \quad \text{with } \sigma \in \{\uparrow,\downarrow\} \text{ and } k \in \{1,\ldots,N_{\mathrm{frag}}\}. \tag{3.67}$$

In total, we have $4N_{\mathrm{frag}}$ spin-orbitals in the CAS. The number of electrons that have to be distributed among these orbitals is reduced to $N_e - 2N_{\mathrm{frag}}$, since $2N_{\mathrm{frag}}$ electrons have been absorbed in the new vacuum (see Eq. (3.60)).

In the light of the above, the ground-state wave function of the interacting problem is approximated as

$$|\Psi\rangle \approx \sum_{\alpha=1}^{\binom{4N_{\mathrm{frag}}}{N_e-2N_{\mathrm{frag}}}} \tilde{\Psi}_\alpha |\tilde{\Phi}_\alpha\rangle = \sum_{\alpha=1}^{\binom{4N_{\mathrm{frag}}}{N_e-2N_{\mathrm{frag}}}} \tilde{\Psi}_\alpha \left[\prod_{k=1}^{N_e-2N_{\mathrm{frag}}} \hat{\psi}_k^{\dagger\mathrm{CAS}}\right]_\alpha |\tilde{0}\rangle \equiv \hat{\Psi}_{\mathrm{emb}}^\dagger |\tilde{0}\rangle. \tag{3.68}$$

where we defined the notion of the embedding field operator $\hat{\Psi}_{\mathrm{emb}}^\dagger$ for later use.

The approximation made in Eq. (3.68) means that, in DMET we assume that in the interacting case we have the same set of fully occupied and completely empty orbitals as in the non-interacting case and that correlation effects in the system are considered only within the CAS. This, of course, is a crude approximation, but we assume that it provides good results for observables on the fragment.

The non-trivial part of $|\Psi\rangle$ is obtained by diagonalizing the embedding Hamiltonian $\hat{H}_{\mathrm{emb}}$, which is obtained via the single-particle projection of the original many-body Hamiltonian (Eq. (2.55)) as

$$\hat{H}_{\mathrm{emb}} = \hat{h}_{\mathrm{emb}} + \hat{W}_{\mathrm{emb}} = \sum_{a,b=1}^{2N_{\mathrm{frag}}} \sum_\sigma h_{ab}^{\mathrm{emb}} \hat{c}_{a\sigma}^\dagger \hat{c}_{b\sigma} + \frac{1}{2} \sum_{i,j,k,l=1}^{2N_{\mathrm{frag}}} \sum_{\sigma,\sigma'} W_{abcd}^{\mathrm{emb}} \hat{c}_{a\sigma}^\dagger \hat{c}_{b\sigma'}^\dagger \hat{c}_{d\sigma'} \hat{c}_{c\sigma}\,, \tag{3.69}$$

with

$$h_{ab}^{\mathrm{emb}} = \sum_{a,b=1}^{N} P_{ai}^\dagger h_{ij} P_{jb}, \qquad W_{abcd}^{\mathrm{emb}} = \sum_{a,b=1}^{N} P_{ai}^\dagger P_{bj}^\dagger W_{ijkl} P_{kc} P_{ld}. \tag{3.70}$$

The ground state of $\hat{H}_{\mathrm{emb}}$ can be obtained with an accurate wave-function method, since the dimensionality of the problem reduces significantly for sufficiently small N_{frag}.

In single-shot DMET [22] already this result is used to calculate observables. From the full approximate wave function as defined in Eq. (3.68), we can obtain observables such as the energy of the fragment by tracing out the bath

$$E_A = \sum_{i\in A} \left(\sum_{j=1}^{N} \gamma_{ij} h_{ij} + \frac{1}{2} \sum_{j,k,l=1}^{N} \Gamma_{ijkl} W_{ijkl} \right) \tag{3.71}$$

with

$$\gamma_{ij} = \langle\Psi|\sum_{\sigma}\hat{c}^{\dagger}_{i\sigma}\hat{c}_{j\sigma}|\Psi\rangle, \qquad \Gamma_{ijkl} = \langle\Psi|\sum_{\sigma,\sigma'}\hat{c}^{\dagger}_{i\sigma}\hat{c}^{\dagger}_{j\sigma'}\hat{c}_{l\sigma'}\hat{c}_{k\sigma}|\Psi\rangle. \tag{3.72}$$

Eq. (3.71) can equivalently be applied to any other observable.

The full system is described by treating every part of it as a fragment and, hence, by calculating a set of embedding wave functions. In our example, the system would be described by N/N_{frag} fragments. Observables are then calculated by summing over the fragments.

3.3.3 Self-consitency

In most cases, however, the set of embedding wave functions is used to improve the projection in a self-consistent manner. In this context, improving the projection is equivalent to optimizing the CAS orbitals. This means that the Slater determinant $|\Phi\rangle$, from which they are constructed, has to be improved. This is achieved by updating the single-particle Hamiltonian $\hat{h}$ by adding a non-local correlation potential $\hat{u}$ to it

$$\hat{h} \;\rightarrow\; \hat{h}' = \hat{h} + \sum_{A}\sum_{i,j\in A}\sum_{\sigma} u^{A}_{ij}\hat{c}^{\dagger}_{i\sigma}\hat{c}_{j\sigma} \tag{3.73}$$

This correlation potential is found by minimizing the difference between interacting and non-interacting 1RDMs on the fragment

$$\min \sum_{A}\sum_{i,j\in A}\sum_{\sigma}\left|\langle\Psi^{A}|\hat{c}^{\dagger}_{i\sigma}\hat{c}_{j\sigma}|\Psi^{A}\rangle - \langle\Phi|\hat{c}^{\dagger}_{i\sigma}\hat{c}_{j\sigma}|\Phi\rangle\right|^{2} \tag{3.74}$$

or on the corresponding CASs

$$\min \sum_{A}\sum_{i,j\in \text{CAS}_A}\sum_{\sigma}\left|\langle\Psi^{A}|\hat{c}^{\dagger}_{i\sigma}\hat{c}_{j\sigma}|\Psi^{A}\rangle - \langle\Phi|\hat{c}^{\dagger}_{i\sigma}\hat{c}_{j\sigma}|\Phi\rangle\right|^{2}. \tag{3.75}$$

The orbitals are updated until the potential $\hat{u}$ does not change anymore.

3.3.4 Gains and drawbacks of DMET

DMET was developed for fermionic lattice systems such as the Hubbard model [20] and extended to closely related *ab initio* systems, such as hydrogen rings and grids [21]. For these systems it provides results comparable to DMRG but with much lower cost, since only fragments have to be calculated with an expensive wave-function method instead of the full system. Moreover, systems to which DMET was initially applied, are translationally invariant, meaning that only one fragment has to be considered in Eq. (3.74) or Eq. (3.75) and also for calculating observables, reducing the overall computational cost. The size of the fragment determines how much of correlation is captured within the projection and DMET results, therefore, can be improved by increasing the fragment size.

The DMET method, however, also has its downsides. One of the weaknesses is that both of the proposed optimizations schemes for the correlation potential (Eq. (3.74) and Eq. (3.75)) have their drawbacks

- 1RDMs of the embedding and the non-interacting system can be matched exactly on the fragment. The solution of Eq. (3.74), however, is not unique [90], which leads to instabilities and convergence problems [91].

- Matching 1RDMs on the full CAS (Eq. (3.75)) does lead to a unique solution for the correlation potential and hence provides a robust convergence criterion. Therefore, this type of matching is used in common DMET implementations. However, the 1RDMs cannot be made exactly the same [90], which raises questions about justification of the target non-interacting system in the first place. This type of matching can e.g. result in wrong particle numbers [90].

Another issue, which arises also in initially targeted systems, is symmetry breaking. It appears per construction when a translationally invariant system is projected onto a fragment and bath; the embedding system does not have the same symmetry properties as the full system. This fact, however, has its benefits. It is necessary in order to mimic important many-body effects [91], e.g. appearance of the Mott gap in the Hubbard-Holstein model [92]. Unfortunately though, symmetries of observables such as the density are often lost in DMET.

Generalization of the above issue is the appearance of density-discontinuities at fragment boundaries in DMET [93]. Especially for inhomogeneous systems, this can lead to convergence problems, since the correlation potential has to mimic these discontinuities. These errors are then passed on to the next step, since they cannot be circumvented by periodic continuation of the correlation potential as in the homogeneous case. Examples for this issue will be shown in section 6.2.3.

The discontinuity problem of DMET is addressed e.g. in the *Bootstrap embedding* method [93], where the boundaries of a fragment are matched to the center of a neighboring fragment such that the density remains continuous. A simple alternative that uses overlapping patches was introduced in [88] and we will discuss it in more detail in section 5.2.1.

4 Light-matter interaction

This chapter of the thesis is dedicated to the description of electronic systems that interact with electromagnetic fields, both classical and quantum. The underlying theory is called quantum electrodynamics (QED), which is the first formulated quantum field theory [94] and which to date provides some of the most accurate prediction, such as the Lamb shift of the energy levels of hydrogen [95]. Here, we will discuss only relevant parts of the theory that will leads us to the non-relativistic QED Hamiltonian in long-wavelength limit, which is used to describe the behavior of molecular systems strongly coupled to cavity photons. Comprehensive derivations and discussions on this topic can be found in [96, 97].

4.1 Classical electrodynamics

Maxwell's equations

Maxwell's equations [98] lie at the heart of classical electrodynamics. These are first order differential equations for the electric field $\boldsymbol{E}$ and the magnetic field $\boldsymbol{B}$

$$\nabla \times \boldsymbol{E} = -\frac{\partial \boldsymbol{B}}{\partial t}, \tag{4.1}$$

$$\nabla \times \boldsymbol{B} = \mu_0 \boldsymbol{j} + \frac{1}{c^2}\frac{\partial \boldsymbol{E}}{\partial t}, \tag{4.2}$$

$$\nabla \cdot \boldsymbol{E} = 4\pi\rho, \tag{4.3}$$

$$\nabla \cdot \boldsymbol{B} = 0, \tag{4.4}$$

where ρ is the charge density and $\boldsymbol{j}$ the current density, which is caused by moving charged particles, and μ_0 is the magnetic permeability in vacuum. It is related to electric permittivity ε_0 and velocity of light c in vacuum via $c = (\varepsilon_0\mu_0)^{-1/2}$. Here, we again use atomic units and also omit the spatial and temporal dependencies $(\boldsymbol{r}, t)$ of all quantities.

The energy of the field is given by [98]

$$E_{\text{field}} = \frac{\varepsilon_0}{2}\int d\boldsymbol{r}\left(\boldsymbol{E}^2 + c^2\boldsymbol{B}^2\right). \tag{4.5}$$

Electromagnetic potentials

Following Helmholz' theorem, $\boldsymbol{E}$ and $\boldsymbol{B}$ can be constructed from a scalar (electric) potential Φ and a vector (magnetic) potential $\boldsymbol{A}$. Generally, a twice continuously differentiable square-integrable vector field on $\mathbb{R}^3$ can be separated in its transversal (source-free) and longitudinal (curl-free) components, which further can be written in terms of a general scalar potential Φ_F and a vector potential $\boldsymbol{A}_F$ [99]

$$\boldsymbol{F} = \boldsymbol{F}_{\parallel} + \boldsymbol{F}_{\perp} = -\nabla\Phi_F + \nabla \times \boldsymbol{A}_F. \tag{4.6}$$

From the Maxwell's equation (4.4) we deduce that the magnetic field is always purely transversal and that we can write

$$\boldsymbol{B} = \boldsymbol{B}_{\parallel} = \nabla \times \boldsymbol{A}. \tag{4.7}$$

Here, we omitted the subscript in the magnetic vector potential $\boldsymbol{A}_B = \boldsymbol{A}$. We will also omit the subscripts in the electric scalar potential $\Phi_E = \Phi$. For the electric field we combine Eqs. (4.1), (4.2) and (4.7) to obtain

$$\boldsymbol{E} = \boldsymbol{E}_{\parallel} + \boldsymbol{E}_{\perp} = -\nabla\Phi + \nabla \times \boldsymbol{A}_E = -\nabla\Phi - \frac{\partial \boldsymbol{A}}{\partial t}, \tag{4.8}$$

where the last equality follows from Eqs. (4.1) and (4.7)

$$\nabla \times \boldsymbol{E} = \nabla \times \boldsymbol{E}_{\perp} = -\frac{\partial \boldsymbol{B}}{\partial t} = -\frac{\partial}{\partial t}\nabla \times \boldsymbol{A} = \nabla \times \left(-\frac{\partial \boldsymbol{A}}{\partial t}\right). \tag{4.9}$$

Gauge freedom and gauge fixing

Both the scalar and the vector potential are not unique and can be modified in the following way

$$\Phi' = \Phi - \frac{\partial \chi}{\partial t}, \tag{4.10}$$

$$\boldsymbol{A}' = \boldsymbol{A} + \nabla\chi. \tag{4.11}$$

with any twice-differentiable scalar function $\chi = \chi(\boldsymbol{r}, t)$ without changing the physics. Put differently, the Maxwell's equations are invariant under the transformation above. This freedom of choice is called *gauge freedom* and the transformation *gauge transformation*. The electric and the magnetic field are gauge-independent.

A popular gauge choice, which we will also use in this thesis, is the Coulomb or transversal gauge. Here, the vector potential is chosen to be purely transversal

$$\nabla \cdot \boldsymbol{A} = 0. \tag{4.12}$$

This choice combined with Eqs. (4.3) and (4.8) implies that

$$\Delta\Phi = -4\pi\rho, \tag{4.13}$$

which is known as the Poisson equation. This equation implies that the electric potential changes instantly everywhere in response to a local change in charge distribution. The instantaneous Coulomb interaction between charged particles that we already introduced in our standard molecular Hamiltonian in section 2.4 is the direct consequence of the Coulomb gauge.

Light waves

Without presence of charges, the Coulomb gauge becomes the *radiation gauge*

$$\nabla \cdot \boldsymbol{A} = 0, \qquad \Phi = 0 \tag{4.14}$$

and we can rewrite Eq. (4.2) as a wave equation for the vector potential on $\mathbb{R}^3$

$$\left(\Delta - \frac{1}{c^2}\frac{\partial^2}{\partial t^2}\right)\boldsymbol{A}(\boldsymbol{r}, t) = 0. \tag{4.15}$$

This equation has plane-wave solutions of the form

$$\boldsymbol{A} = \boldsymbol{A}_{\lambda\boldsymbol{k}} e^{i(\boldsymbol{k}\boldsymbol{r}-\omega t)} \equiv \boldsymbol{A}_{\lambda\boldsymbol{k}}(t) e^{i\boldsymbol{k}\boldsymbol{r}}. \tag{4.16}$$

Here, $\boldsymbol{k}$ is the propagation vector of the plane wave and $\boldsymbol{A}_{\lambda\boldsymbol{k}}$ the amplitude vector, which is perpendicular to it: $\boldsymbol{A}_{\lambda\boldsymbol{k}} \cdot \boldsymbol{k} = 0$. Hence, in a three-dimensional space there are two possible polarizations λ and we write $\boldsymbol{A}_{\lambda\boldsymbol{k}} = A_{\lambda\boldsymbol{k}} \boldsymbol{e}_{\lambda\boldsymbol{k}}$ with polarization vectors $\boldsymbol{e}_{\lambda\boldsymbol{k}}$. The frequency ω in Eq. (4.16) is related to the wave vector via the dispersion relation of light in vacuum

$$\omega_k = c|\boldsymbol{k}|. \tag{4.17}$$

4.2 Quantization of the free electromagnetic field

We will now briefly discuss quantization of light waves introduced in the previous section following [100]. We will keep the radiation gauge and therefore consider only purely transversal fields.

We begin by expanding a general vector potential in terms of plane waves of Eq. (4.16)

$$\boldsymbol{A}(\boldsymbol{r}, t) = \sum_{\boldsymbol{k},\lambda} \boldsymbol{e}_{\lambda\boldsymbol{k}} \left[A_{\lambda\boldsymbol{k}} e^{i(\boldsymbol{k}\boldsymbol{r}-\omega_k t)} + A^*_{\lambda\boldsymbol{k}} e^{-i(\boldsymbol{k}\boldsymbol{r}-\omega_k t)} \right]. \tag{4.18}$$

For the fields we write accordingly

$$\boldsymbol{E}_\perp(\boldsymbol{r}, t) = i \sum_{\boldsymbol{k},\lambda} \omega_k \boldsymbol{e}_{\lambda\boldsymbol{k}} \left[A_{\lambda\boldsymbol{k}} e^{i(\boldsymbol{k}\boldsymbol{r}-\omega_k t)} - A^*_{\lambda\boldsymbol{k}} e^{-i(\boldsymbol{k}\boldsymbol{r}-\omega_k t)} \right], \tag{4.19}$$

$$\boldsymbol{B}(\boldsymbol{r}, t) = i \sum_{\boldsymbol{k},\lambda} \boldsymbol{k} \times \boldsymbol{e}_{\lambda\boldsymbol{k}} \left[A_{\lambda\boldsymbol{k}} e^{i(\boldsymbol{k}\boldsymbol{r}-\omega_k t)} + A^*_{\lambda\boldsymbol{k}} e^{-i(\boldsymbol{k}\boldsymbol{r}-\omega_k t)} \right]. \tag{4.20}$$

With these we obtain for the energy of the radiation field (Eq. (4.5))

$$E_{\text{ph}} = \varepsilon_0 V \sum_{\boldsymbol{k},\lambda} \omega_k^2 \left(A_{\lambda\boldsymbol{k}} A^*_{\lambda\boldsymbol{k}} + A^*_{\lambda\boldsymbol{k}} A_{\lambda\boldsymbol{k}} \right), \tag{4.21}$$

where V is the quantization volume. In practice, the quantization is performed in a finite volume V and the full space is then constructed through periodic continuation of this volume, which is equivalent to periodic boundary conditions.

We now promote the classical potential and the fields to field operators and the amplitudes $A^{(*)}_{\lambda\boldsymbol{k}}$ to photon creation and annihilation operators denoted by $\hat{a}^{(\dagger)}$.

$$A_{\lambda\boldsymbol{k}} \to (2\varepsilon_0 V \omega_k)^{-1/2} \hat{a}_{\lambda\boldsymbol{k}}, \qquad A^*_{\lambda\boldsymbol{k}} \to (2\varepsilon_0 V \omega_k)^{-1/2} \hat{a}^\dagger_{\lambda\boldsymbol{k}}. \tag{4.22}$$

Inserting the above expressions into Eq. (4.21) leads to the Hamiltonian of the free electromagnetic field

$$\hat{H}_{\text{p}} = \frac{1}{2} \sum_{\boldsymbol{k},\lambda} \omega_k \left(\hat{a}_{\lambda\boldsymbol{k}} \hat{a}^\dagger_{\lambda\boldsymbol{k}} + \hat{a}^\dagger_{\lambda\boldsymbol{k}} \hat{a}_{\lambda\boldsymbol{k}} \right) = \sum_{\boldsymbol{k},\lambda} \omega_k \left(\hat{a}^\dagger_{\lambda\boldsymbol{k}} \hat{a}_{\lambda\boldsymbol{k}} + \frac{1}{2} \right). \tag{4.23}$$

For the last part of the equation, we have used the fact that photons are bosons and that the corresponding creation and annihilation operators obey the bosonic commutator ($[a, b] = ab - ba$) relations

$$\left[\hat{a}_{\lambda\boldsymbol{k}}, \hat{a}_{\lambda'\boldsymbol{k}'} \right] = \left[\hat{a}^\dagger_{\lambda\boldsymbol{k}}, \hat{a}^\dagger_{\lambda'\boldsymbol{k}'} \right] = 0, \qquad \left[\hat{a}_{\lambda\boldsymbol{k}}, \hat{a}^\dagger_{\lambda'\boldsymbol{k}'} \right] = \delta_{\lambda\lambda'} \delta_{\boldsymbol{k}\boldsymbol{k}'}. \tag{4.24}$$

The Hamiltonian in Eq. (4.23) is very simple. It consists of a sum of one-body operators only, meaning that quanta of the free electromagnetic field do not interact with one another[1].

[1] The actual reason for it is that QED is an *abelian* gauge theory, which means that the generators of the underlying symmetry group build a commutative Lie algebra. Quantizing an abelian gauge theory then results in having non-interacting gauge bosons, see e.g. [101] for more details.

The operators $\hat{a}_{\lambda\boldsymbol{k}}$ and $\hat{a}^\dagger_{\lambda\boldsymbol{k}}$ are defined on the photonic Fock space. In the following, we will briefly discuss how this space is built similar to our discussion in the electronic case in section 2.2. We start by defining the one-particle basis functions (photonic modes). For periodic boundary conditions these are plane waves

$$\phi(\lambda,\boldsymbol{k}) = \phi^\lambda(\boldsymbol{k}) = \frac{1}{\sqrt{V}} e^{i\boldsymbol{k}\boldsymbol{r}}, \qquad \text{with} \quad \boldsymbol{k} = \frac{2\pi}{\sqrt[3]{V}} \begin{pmatrix} m_1 \\ m_2 \\ m_3 \end{pmatrix} \quad \text{and} \quad m_{1,2,3} = 0, \pm 1, \pm 2 \ldots, \tag{4.25}$$

where we assumed a cubic quantization volume for simplicity. For other geometries and boundary conditions, these basis functions are much more complicated and we usually do not have their explicit analytical form [102].

Photons are bosons, which means that their many-body wave-function has to be symmetric with respect to exchange of particles. This implies that photonic many-body basis states with N_p particles are, as opposed to Slater determinants for electrons, simple *permanents*

$$|\Phi_\mathrm{p}\rangle = \prod_{j=1}^{N_\mathrm{p}} \phi_j^\lambda(\boldsymbol{k}). \tag{4.26}$$

The symmetry further has the consequence that each photonic mode can in principle be occupied by any possible number of particles. Here, the language of second quantization comes in very handy: every basis state is fully determined by the number of particles $n_{\lambda,\boldsymbol{k}}$ occupying the corresponding mode $\phi^\lambda(\boldsymbol{k})$

$$|\Phi_\mathrm{p}\rangle \rightarrow |\{n_{\lambda,\boldsymbol{k}}\}\rangle, \qquad \text{with} \quad \hat{a}^\dagger_{\lambda,\boldsymbol{k}}\hat{a}_{\lambda,\boldsymbol{k}} = n_{\lambda,\boldsymbol{k}}|\{n_{\lambda,\boldsymbol{k}}\}\rangle, \tag{4.27}$$

where $\hat{a}^\dagger_{\lambda,\boldsymbol{k}}\hat{a}_{\lambda,\boldsymbol{k}}$ is the corresponding particle-number operator. We call the states $|\{n_{\lambda,\boldsymbol{k}}\}\rangle$ *Fock number states* or *Fock states*. For creation and annihilation operators for a particular mode we have the following relations in terms of Fock states

$$\hat{a}^\dagger|n\rangle = \sqrt{n+1}|n+1\rangle \qquad \hat{a}\ |n\rangle = \sqrt{n}|n-1\rangle. \tag{4.28}$$

Since most photonic observables like electric or magnetic fields do not conserve the number of particles (see expansions in Eqs. (4.19)-(4.20)), photonic calculations have to be performed in the Fock space.

First-quantization picture

Although the language of second quantization is much more convenient for photons, we here will briefly derive the form of the photonic Hamiltonian $\hat{H}_\mathrm{p}$ in the first-quantization picture. Later, this formulation will make some transformations on the way to the non-relativistic QED Hamiltonian easier to handle.

First, we establish that each mode in the expansion of the vector potential or the fields (Eqs. (4.18)-(4.20)) can be associated with a quantum harmonic oscillator [100], if we relate

$$\hat{a}_{\lambda\boldsymbol{k}} = \frac{1}{\sqrt{2\omega_k}}\left(\omega_k \hat{q}_{\lambda\boldsymbol{k}} + i\hat{p}_{\lambda\boldsymbol{k}}\right), \qquad \hat{a}^\dagger_{\lambda\boldsymbol{k}} = \frac{1}{\sqrt{2\omega_k}}\left(\omega_k \hat{q}_{\lambda\boldsymbol{k}} - i\hat{p}_{\lambda\boldsymbol{k}}\right), \tag{4.29}$$

or correspondingly

$$\hat{q}_{\lambda\boldsymbol{k}} = \frac{1}{\sqrt{2\omega_k}}\left(\hat{a}^\dagger_{\lambda\boldsymbol{k}} + \hat{a}_{\lambda\boldsymbol{k}}\right), \qquad \hat{p}_{\lambda\boldsymbol{k}} = -i\sqrt{\frac{\omega_k}{2}}\left(\hat{a}^\dagger_{\lambda\boldsymbol{k}} - \hat{a}_{\lambda\boldsymbol{k}}\right). \tag{4.30}$$

The displacement operators $\hat{q}_{\lambda \boldsymbol{k}}$ play the role of the set of canonical variables with conjugated momenta $\hat{p}_{\lambda \boldsymbol{k}}$. The Hamiltonian of Eq. (4.23) then takes the form of a harmonic oscillator

$$\hat{H}_{\mathrm{p}} = \frac{1}{2} \sum_{\boldsymbol{k},\lambda} \hat{p}^2_{\lambda \boldsymbol{k}} + \omega_k^2 \hat{q}^2_{\lambda \boldsymbol{k}}. \tag{4.31}$$

This form of $\hat{H}_{\mathrm{p}}$ can be transformed back to the language of first-quantization by expressing the operators in terms of generalized coordinates $q_{\lambda \boldsymbol{k}}$ [49] [2]

$$\hat{q}_{\lambda \boldsymbol{k}} \rightarrow q_{\lambda \boldsymbol{k}}, \qquad \hat{p}_{\lambda \boldsymbol{k}} \rightarrow i \frac{\partial}{\partial q_{\lambda \boldsymbol{k}}}. \tag{4.32}$$

Therefore, in the language of first quantization, the Hamiltonian of the transversal electromagnetic field reads

$$\hat{H}_{\mathrm{p}} = \frac{1}{2} \sum_{\boldsymbol{k},\lambda} -\frac{\partial^2}{\partial q^2_{\lambda \boldsymbol{k}}} + \omega_k^2 q^2_{\lambda \boldsymbol{k}}. \tag{4.33}$$

4.3 Semi-classical approach to light-matter interaction

In this section, as a preliminary step towards full non-relativistic QED, we will discuss how to include interactions of quantized matter with a classical electromagnetic field into the Schrödinger equation. We will consider only molecular Hamiltonians in the clamped-nuclei approximation introduced in section 2.4.1.

The form of light-matter interaction can be deduced from gauge-invariance of the electromagnetic field and additional symmetry properties. For the electronic many-body wave function we can identify the following very simple symmetry

$$|\Psi\rangle \quad \rightarrow \quad |\Psi'\rangle = e^{iq\chi}|\Psi\rangle, \tag{4.34}$$

the $U(1)$ symmetry. This simply means that the wave function is defined up to a local phase $\chi = \chi(\boldsymbol{r}, t)$, since this phase does not affect observables. We can show this by considering a general expectation value

$$\begin{aligned} \langle \Psi' | \hat{O} | \Psi' \rangle &= \langle \Psi | e^{-iq\chi} \hat{O} e^{iq\chi} | \Psi \rangle \\ &= \langle \Psi | \hat{O} | \Psi \rangle + \langle \Psi | \left[\hat{O}, e^{iq\chi} \right] | \Psi \rangle + \frac{1}{2} \langle \Psi | \left[\left[\hat{O}, e^{iq\chi} \right], e^{iq\chi} \right] | \Psi \rangle + \cdots \\ &= \langle \Psi | \hat{O} | \Psi \rangle, \end{aligned} \tag{4.35}$$

where we have used the BCH expansion introduced in Eq. (3.19) and the fact that all commutators above vanish for hermitian operators

$$\langle \Psi | \hat{O} e^{iq\chi} - e^{iq\chi} \hat{O} | \Psi \rangle = e^{iq\chi} \left(\langle \hat{O}^\dagger \Psi | \Psi \rangle - \langle \Psi | \hat{O} \Psi \rangle \right) = e^{iq\chi} \left(\langle \hat{O} \rangle - \langle \hat{O} \rangle \right) = 0. \tag{4.36}$$

We call the transformation defined in Eq. (4.34) a *gauge transformation* similar to Eqs. (4.10)-(4.11) for electromagnetic potentials and choose the same scalar function $\chi(\boldsymbol{r}, t)$. Same as the Maxwell's equations in classical electrodynamics (see section 4.1), the electronic Schrödinger equation has to be invariant under the gauge transformation of Eq. (4.34).

As a first step, we consider the Schrödinger equation for one electron in real space. We examine the behavior of a general first-order differential operator $\hat{D}$ under a local gauge transformation

$$\hat{D}|\Psi\rangle = \hat{D}\left(e^{-iq\chi} |\Psi'\rangle \right) = e^{-iq\chi} \left(\hat{D} - iq\left(\hat{D}\chi \right) \right). |\Psi'\rangle \tag{4.37}$$

[2] See Eq. (2.10) for comparison to matter particles.

Inserting this into Eq. (2.3), we obtain

$$i\left(\frac{\partial}{\partial t} - iq\frac{\partial \chi}{\partial t}\right)|\Psi'\rangle = \frac{1}{2}\Big(-i\nabla - q\nabla\chi\Big)^2|\Psi'\rangle. \tag{4.38}$$

If we now insert the gauge freedom conditions of the scalar and vector potential Eqs. (4.10)-(4.11) in the equation above

$$i\left(\frac{\partial}{\partial t} - iq\Phi + iq\Phi'\right)|\Psi'\rangle = \frac{1}{2}\left(-i\nabla - q\boldsymbol{A}' + q\boldsymbol{A}\right)^2|\Psi'\rangle, \tag{4.39}$$

we deduce that the following transformation of the derivatives

$$\frac{\partial}{\partial t} \quad \rightarrow \quad \frac{\partial}{\partial t} + iq\Phi, \qquad\qquad \nabla \quad \rightarrow \quad \nabla - iq\boldsymbol{A} \tag{4.40}$$

keeps the Schrödinger equation form-invariant under the gauge transformation of Eq. (4.34). With this transformation behavior, the Schrödinger equation for an electron in the presence of electromagnetic field is given by

$$i\frac{\partial}{\partial t}|\Psi\rangle = \left[\frac{1}{2}\left(-i\nabla + q\boldsymbol{A}\right)^2 + q\Phi\right]|\Psi\rangle. \tag{4.41}$$

Here, we see that the scalar potential Φ plays the role of an external potential. It is the potential that is generated by clamped charged nuclei. The coupling constant q of the electromagnetic field and the electron can be related to the electric charge of an electron $-e$. Hence, in atomic units we have $q = -1$.

The transformation prescription in Eq. (4.40) is called *minimal coupling*. It is the simplest form of derivative transformation that ensures form-invariance of the Schrödinger equation[3] under the given gauge transformation of Eq. (4.34).

For a many-electron system we can generalize the Hamiltonian in Eq. (4.41) in a straight-forward manner. By further adding the energy of the electromagnetic field (Eq. (4.5)) we obtain the Hamiltonian for semi-classical treatment of light-matter interaction

$$\begin{aligned}\hat{H}_{\text{semi-classical}} = \frac{1}{2}\sum_{j=1}^{N_e}\left(i\nabla_j + \boldsymbol{A}(\boldsymbol{r}_j, t)\right)^2 - \sum_{j=1}^{N_e}\Phi(\boldsymbol{r}_j, t) + \frac{1}{2}\sum_{j=1}^{N_e}\sum_{k=1}^{N_e}\frac{1}{|\boldsymbol{r}_j - \boldsymbol{r}_k|} \\ + \frac{\varepsilon_0}{2}\int d\boldsymbol{r}\boldsymbol{E}_\perp^2(\boldsymbol{r}, t) + c^2\boldsymbol{B}^2(\boldsymbol{r}, t).\end{aligned} \tag{4.42}$$

4.4 Hamiltonain of non-relativistic quantum electrodynamics

Pauli-Fierz Hamiltonian

We proceed by replacing the classical quantities in Eq. (4.42) by their quantum counterparts (Eq. (4.32) for $\hat{H}_\text{p}$) and write in the language of first quantization

$$\hat{H}_\text{PF} = \frac{1}{2}\sum_{j=1}^{N_e}\left(i\nabla_j + \hat{\boldsymbol{A}}(\boldsymbol{r}_j)\right)^2 - \sum_{j=1}^{N_e}\Phi(\boldsymbol{r}_j) + \frac{1}{2}\sum_{j=1}^{N_e}\sum_{k=1}^{N_e}\frac{1}{|\boldsymbol{r}_j - \boldsymbol{r}_k|} + \frac{1}{2}\sum_{\boldsymbol{k},\lambda} -\frac{\partial^2}{\partial q_{\lambda\boldsymbol{k}}^2} + \omega_k^2 q_{\lambda\boldsymbol{k}}^2. \tag{4.43}$$

Here, we work in the Schrödinger picture of quantum mechanics [47], in which operators of the electromagnetic field do not have any explicit time dependence. The above Hamiltonian is known as (spinless) Pauli-Fierz Hamiltonian.

[3] Same prescription holds for the relativistic counterpart of the Schrödinger equation, the Dirac equation [50], since this transformation is also invariant under the Lorentz-transformation.

Long-wavelength limit

In a typical optical set-up the size of atomic and molecular components (few ångström) is significantly smaller than the wave length of used light (couple hundreds of nanometers). In these cases, we can approximate mode functions of Eq. (4.25) as being constant in space ($e^{\pm i\boldsymbol{k}\boldsymbol{r}} \approx 1$). With this, expressions for the vector potential and the electric field (quantized versions of Eqs. (4.18)-(4.19)) can be simplified as

$$\hat{\boldsymbol{A}}(\boldsymbol{r}) = \hat{\boldsymbol{A}} = \frac{1}{\sqrt{\varepsilon_0 V}} \sum_{\boldsymbol{k},\lambda} \boldsymbol{e}_{\lambda\boldsymbol{k}} \hat{q}_{\lambda\boldsymbol{k}}, \tag{4.44}$$

$$\hat{\boldsymbol{E}}_\perp(\boldsymbol{r}) = \hat{\boldsymbol{E}} = \frac{-1}{\sqrt{\varepsilon_0 V}} \sum_{\boldsymbol{k},\lambda} \boldsymbol{e}_{\lambda\boldsymbol{k}} \hat{p}_{\lambda\boldsymbol{k}}. \tag{4.45}$$

The Pauli-Fierz Hamiltonian becomes

$$\begin{aligned}\hat{H}_{\mathrm{PF_V}} = &\frac{1}{2}\sum_{j=1}^{N_\mathrm{e}} \left(-\nabla_j^2 + 2i\hat{\boldsymbol{A}}\cdot\nabla_j + \hat{\boldsymbol{A}}^2\right) - \sum_{j=1}^{N_\mathrm{e}} \Phi(\boldsymbol{r}_j) + \frac{1}{2}\sum_{j=1}^{N_\mathrm{e}}\sum_{k=1}^{N_\mathrm{e}} \frac{1}{|\boldsymbol{r}_j - \boldsymbol{r}_k|} \\ &+ \frac{1}{2}\sum_{\boldsymbol{k},\lambda} -\frac{\partial^2}{\partial q_{\lambda\boldsymbol{k}}^2} + \omega_k^2 q_{\lambda\boldsymbol{k}}^2.\end{aligned} \tag{4.46}$$

This form of the Hamiltonian is usually called Pauli-Fierz Hamiltonian in the *velocity gauge*.

Length gauge

In the Coulomb gauge the light-matter interaction in Eq. (4.46) is written in terms of the vector potential and is therefore gauge-dependent. This disadvantage can be removed by transforming $\hat{H}_{\mathrm{PF_V}}$ into a different gauge, the *length gauge*. This transformation is known as Power-Zienau-Woolley transformation [103, 104]. It consists of a unitary transformation of the from $e^{-i\chi}\hat{H}e^{i\chi}$ with a fixed gauge function χ that mixes matter and photonic degrees of freedom such that the interaction between the two becomes gauge independent.

Particularly, in the long-wavelength limit, this transformation is quite simple [35, 105]. The gauge function becomes $\chi = \hat{\boldsymbol{A}}\cdot\hat{\boldsymbol{d}}$, where $\hat{\boldsymbol{d}}$ is the dipole operator of the system, here the dipole operator of the electrons

$$\hat{\boldsymbol{d}} = -\sum_{j=1}^{N_\mathrm{e}} \boldsymbol{r}_j. \tag{4.47}$$

Following [105], we now transform every term in Eq. (4.46) individually by consequently applying Eq. (4.37) to every relevant term in Eq. (4.46). Terms that transform non-trivially are

$$e^{i\hat{\boldsymbol{A}}\cdot\boldsymbol{r}_j}\left(\nabla_{\boldsymbol{r}_j}^2\, e^{-i\hat{\boldsymbol{A}}\cdot\boldsymbol{r}_j}\right) = \nabla_{\boldsymbol{r}_j}^2 + 2i\hat{\boldsymbol{A}}\cdot\nabla_{\boldsymbol{r}_j} - \hat{\boldsymbol{A}}^2, \tag{4.48a}$$

$$e^{i\hat{\boldsymbol{A}}\cdot\boldsymbol{r}_j}\left(\hat{\boldsymbol{A}}\cdot\nabla_{\boldsymbol{r}_j}\, e^{-i\hat{\boldsymbol{A}}\cdot\boldsymbol{r}_j}\right) = \hat{\boldsymbol{A}}\cdot\nabla_{\boldsymbol{r}_j} + i\hat{\boldsymbol{A}}^2, \tag{4.48b}$$

$$e^{-i\hat{\boldsymbol{A}}\cdot\hat{\boldsymbol{d}}}\left(\frac{\partial^2}{\partial q_{\lambda\boldsymbol{k}}^2}\, e^{i\hat{\boldsymbol{A}}\cdot\hat{\boldsymbol{d}}}\right) = \frac{\partial^2}{\partial q_{\lambda\boldsymbol{k}}^2} + 2i\frac{\boldsymbol{e}_{\lambda\boldsymbol{k}}\cdot\hat{\boldsymbol{d}}}{\sqrt{\varepsilon_0 V}}\frac{\partial}{\partial q_{\lambda\boldsymbol{k}}} - \frac{1}{\varepsilon_0 V}\left(\boldsymbol{e}_{\lambda\boldsymbol{k}}\cdot\hat{\boldsymbol{d}}\right)^2 = -\left(i\frac{\partial}{\partial q_{\lambda\boldsymbol{k}}} - \frac{\boldsymbol{e}_{\lambda\boldsymbol{k}}\cdot\hat{\boldsymbol{d}}}{\sqrt{\varepsilon_0 V}}\right)^2. \tag{4.48c}$$

In the last part we used the relation given in Eq. (4.44). We insert Eqs. (4.48a)-(4.48c) in Eq. (4.46) and perform the replacement in Eq. (4.32) backwards to obtain

$$\begin{aligned}\hat{H}_\mathrm{L} = &-\frac{1}{2}\sum_{j=1}^{N_\mathrm{e}} \nabla_j^2 - \sum_{j=1}^{N_\mathrm{e}} \frac{1}{c}\Phi(\boldsymbol{r}_j, t) + \frac{1}{2}\sum_{j=1}^{N_\mathrm{e}}\sum_{k=1}^{N_\mathrm{e}} \frac{1}{|\boldsymbol{r}_j - \boldsymbol{r}_k|} \\ &+ \frac{1}{2}\sum_{\boldsymbol{k},\lambda}\left(\hat{p}_{\lambda\boldsymbol{k}} + \frac{\boldsymbol{e}_{\lambda\boldsymbol{k}}\cdot\hat{\boldsymbol{d}}}{\omega_k\sqrt{\varepsilon_0 V}}\right)^2 + \omega_k^2\hat{q}_{\lambda\boldsymbol{k}}^2.\end{aligned} \tag{4.49}$$

By performing the Power-Zienau-Woolley transformation, we have removed the coupling to the vector potential from the electronic part of the Hamiltonian. The electronic part is now the same as in Eq. (2.51). Instead, we now have an explicit dependence on electronic coordinates in the photonic part of the Hamiltonian. The generalized momenta $\hat{p}_{\lambda \boldsymbol{k}}$ are shifted by the electric dipole contribution in polarization direction of the field. The classical analogon to this is that, when electromagnetic fields are considered in matter, the electric field $\boldsymbol{E}$ is replaced by the electric displacement field $\boldsymbol{D}$ in Maxwell's equation Eq. (4.3) [98].

Usually, also the following unitary variable exchange of displacement and momentum coordinates is performed: $\hat{q}_{\lambda \boldsymbol{k}} \to -\frac{1}{\omega_k}\hat{p}_{\lambda \boldsymbol{k}}$ and $\hat{p}_{\lambda \boldsymbol{k}} \to -\omega_k \hat{q}_{\lambda \boldsymbol{k}}$[4], which results in the standard form of the length-gauge QED Hamiltonian

$$\hat{H}_{\mathrm{L}} = \hat{H}_{\mathrm{e}} + \sum_{\boldsymbol{k},\lambda} \left[\frac{1}{2}\left(\hat{p}^2_{\lambda \boldsymbol{k}} + \omega_k^2 \hat{q}_{\lambda \boldsymbol{k}}\right) - \frac{\omega_k}{\varepsilon_0 V} \boldsymbol{e}_{\lambda \boldsymbol{k}} \hat{q}_{\lambda \boldsymbol{k}} \cdot \hat{\boldsymbol{d}} + \frac{1}{\varepsilon_0 V}\left(\boldsymbol{e}_{\lambda \boldsymbol{k}} \cdot \hat{\boldsymbol{d}}\right)^2 \right] \tag{4.50}$$

Above, we have written down the individual parts of the Hamiltonian explicitly. The first term after $\hat{H}_{\mathrm{e}}$ is the Hamiltonian of quantum harmonic oscillators as already discussed in section 4.2. The next term corresponds to the light-matter-interaction Hamiltonian in dipole approximation, which has the same form as its classical counterpart [106]. It corresponds to a linear coupling of the electronic dipole $\boldsymbol{d}$ to the electric displacement field $\boldsymbol{D}$. The last term, however, does not have a classical counterpart. In the literature it is refered to as *dipole self-energy*. In typical quantum optical set-ups it is rather small and, hence, it is often omitted [107]. However, it has been shown recently [105] that keeping this term is necessary, because otherwise the light-matter Hamiltonian is not bounded from below and hence no variational principle holds.

[4] In this way, the photonic Hamiltonian has the usual form of a shifted harmonic oscillator. Further, the dipole operator of the electrons couples to the displacement field and not to its derivative, which makes subsequent calculations easier [35].

Part II:

Self-consistent density-functional embedding

In this part of the thesis, we develop a density embedding approach that allows for construction of approximate exchange-correlation potentials, which does not rely on an explicit form of the energy functional. To this end, we introduce a fixed-point iteration scheme for the density-to-potential mapping that is approximated through a rigorous DMET-inspired embedding scheme. The method is benchmarked for molecular-bond stretching in one and two dimensions, for which we show energies, densities, and potentials. Convergence test with fragment sizes are also provided. This part of the thesis is based on the publication [88].

5 Method

In this chapter, we are going to introduce a fixed-point approach to DFT and develop the self-consistent density-functional embedding (SDE) as not only the first but also as an efficient approximation to it. SDE allows to explicitly construct approximations to the xc potential with increasing accuracy without an underlying energy functional. By including insights from exact wave functions of small fragments into KS description of the system through a self-consistent embedding scheme, signatures of strong correlation can be naturally included into the DFT framework. A path on how to calculated observables from the KS potential is also given.

5.1 Fixed-point approach to DFT

As already discussed in section 3.2.3, there are some issues with the standard DFT approach, with the inaccessibility of the exact energy functional being the most prominent. Here, we avoid these issue by following a different path that involves no explicit approximate expression for $E_{\mathrm{Hxc}}[n]$ or $v_{\mathrm{Hxc}}[n]$. Instead, we first introduce a formal approach that employs density-potential mappings of DFT directly (see e.g. [108]) and then make this approach practical by applying approximations to it. Following the HK theorem, for a given density $n^{(i)}$ there is a interacting system with the external potential $v[n^{(i)}]$ that produces this density. And exactly the same density can be reproduced by non-interacting system with the potential $v_s[n^{(i)}]$. Hence, an interacting density $n^{(i)}(\boldsymbol{r})$ can be uniquely inverted to both an interacting potential $v[n^{(i)}](\boldsymbol{r})$ and a non-interacting potential $v_s[n^{(i)}](\boldsymbol{r})$. The Hxc potential is then defined by the difference of those two potentials

$$v_{\mathrm{KS}}[v_{\mathrm{ext}}, n^{(i)}](\boldsymbol{r}) = v_{\mathrm{ext}}(\boldsymbol{r}) + \underbrace{v_{\mathrm{S}}[n^{(i)}](\boldsymbol{r}) - v[n^{(i)}](\boldsymbol{r})}_{v_{\mathrm{Hxc}}[n^{(i)}](\mathbf{r})}. \tag{5.1}$$

Solving the single-particle eigenvalue equations Eq. (3.38) with $v_{\mathrm{KS}}[v_{\mathrm{ext}}, n^{(i)}]$ we obtain the updated density $n^{(i+1)}$ via Eq. (3.39). Starting with some initial density $n^{(0)}$, this scheme converges at the true ground state density n that is produced by the external potential $v_{\mathrm{ext}} = v[n]$ and we have also found the non-interacting potential $v_{\mathrm{KS}}[n] = v_{\mathrm{S}}[n]$ to reproduce this density.

Note that the fixed-point iteration scheme from reference [108] that we have introduced above does not need any explicit expression of an energy functional. However, it is obvious that the scheme itself is not practical at all. In order to avoid solving the exact Schrödinger equation for one interacting system with v_{ext} we ended up performing inversions not only to obtain the non-interacting $v_{\mathrm{S}}[n^{(i)}]$, which in principle is feasible [109–113], but also to obtain the interacting $v[n^{(i)}]$, which would involve solving the interacting Schrödinger equation multiple times at each step and, hence, increase the numerical complexity of the problem instead of decreasing it.

The embedding method that we develop here targets directly at approximating the fixed-point iteration scheme in a way that no inversion for $v[n]$ is necessary. Within our approach the connection between $v[n]$ and n is given by a DMET- inspired projection (see section 3.3.1) and the exact Schrödinger equation is solved in smaller subsystems.

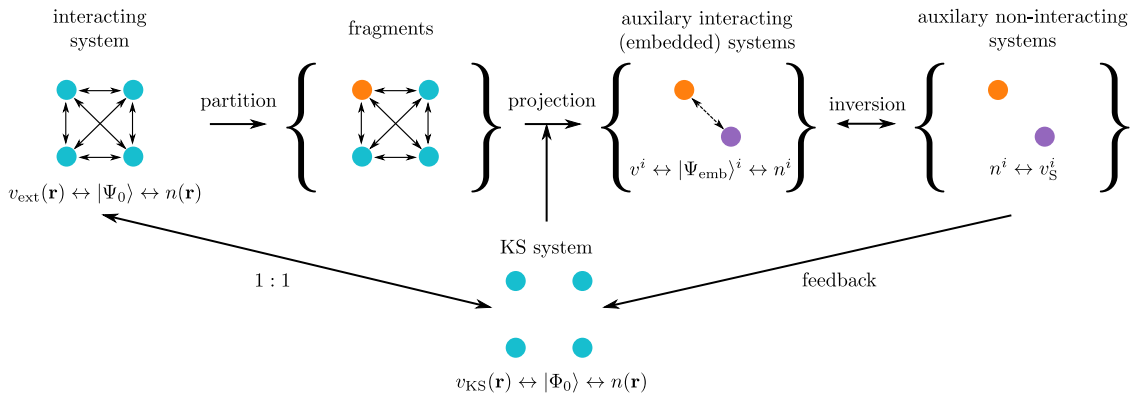

Figure 7. General idea behind the self-consistent density-functional embedding approach: properties of an interacting electronic system with an external potential v_{ext} and a ground-state wave function $|\Psi_0\rangle$ are fully determined by its electronic density $n(\boldsymbol{r})$, that can be uniquely reproduced by a non-interacting system (KS system). The interacting system is divided into fragments. For each fragment (orange) the system is projected onto a smaller auxiliary interacting (embedded) system. The embedded system consists of the fragment, which remains unchanged by the projection and the part of the system that includes interaction and correlation with the fragment (depicted in violet). Each of the embedded systems is then solved on a wave-function level, yielding an accurate density which then can be uniquely mapped onto an auxiliary non-interacting system with the same density. These accurate local potentials are then used to improve the global KS description of the full system. The whole process is repeated self-consistently until convergence of the global KS potential is reached. Graphic published in [88].

5.2 SDE algorithm

The fundamental idea of our density-functional embedding approach is to replace the mapping between the global KS potential and the corresponding density by dividing the system into a set of fragments $\{i\}$ and mapping those onto a set of auxiliary interacting systems with a corresponding set of external potentials $\{v^i\}$, interacting wave-functions $\{|\Psi\rangle^i\}$ and densities $\{n^i\}$. Here, no interacting inversion is needed and we also get an approximated mapping between the KS Slater determinant $|\Phi_0\rangle$ and the ground-state wave function of the system $|\Psi_0\rangle$.

The SDE method is depicted schematically in Fig. 7. It consists of the following steps:

- **Global description:** The full system is described in terms of its ground-state density $n(\boldsymbol{r})$ by means of KS DFT that we have introduced in section 3.2.1.

- **Partition:** The system is divided into fragments. Our proposed partition differs significantly from other DFT embedding schemes [114, 115] and DMET [22] and we will introduce our *continuous partition* in section 5.2.1.

- **Projection:** For each fragment, the full system is projected onto an embedded system, where the fragment is embedded into an effective bath. Out of manifold of possible projectors [17, 20, 86], we here use the projector from the DMET approach, that we introduced in 3.3.1. This projector is modified to treat small particle numbers that we will consider for first applications () in 5.2.2.

- **Fragment calculation:** For each fragment, an accurate calculation is performed with a wave-function method. The fragment wave functions are then used to calculate accurate fragment densities. These wave functions also serve as a local approximation to the mapping between the KS Slater determinant and the ground-state wave function $|\Phi_0[n]\rangle \rightarrow |\Psi_0[n]\rangle$, from which we can directly calculate correlated observables via $O[n] = \langle\Psi[n]|\hat{O}|\Psi[n]\rangle$. Details on this part can be found in section 5.2.3.

- **Local-to-global mapping:** Finally, for each fragment i an auxiliary non-interacting system is found that reproduces the density n_i and the set of obtained potentials $\{v_S[n^i]\}$ is then used to update the global KS potential. How this is done in practice is explained in subsection 5.2.4. The SDE scheme is applied self-consistently and the algorithm is also explained in subsection 5.2.4.

In the remaining part of this chapter, we will outline general ideas behind some parts of the algorithm (those parts that have not already been introduced in the theory part I), whereas most details on the specific implementation of the algorithm are presented in appendix A.1. One detail, however, we want to specify already here: in the following we will consider only systems that are discretized on a real-space grid. This choice is necessary for our partitioning (see section 5.2.1) and it simplifies the local-to-global mapping (see section 5.2.4).

5.2.1 Continuous partition

We begin by considering the task of dividing the full problem into fragments. Generally, the fragments have to cover the full system and should be selected small enough to be calculated with required accuracy.

In embedding approaches like subsystem DFT [87] and also in the framework of partition DFT [114], the system is divided into non-overlapping fragments, which are weakly bounded to one another. In other words, the partition is dictated by density distribution and correlations within the system and cannot be chosen arbitrarily. Therefore, those approaches are not applicable when connections along fragments become important.

In DMET the system is also divided into non-overlapping fragments (see section 3.3.4). The partition itself can be chosen arbitrarily, as particle transfer between fragment and the rest of the system is possible within this approach. The size of the fragments is dictated mostly by the correlation length in the system [20]. Hence, the amount of correlation, which is captured with the DMET method is constrained by the size of the fragment. Thus, by increasing the fragment size, a convergence towards the exact solution is feasible, which makes the method systematically improvable. Dividing the system into non-overlapping fragments, however, causes artificial discontinuities in local observables such as density [93][1], which sometimes also leads to convergence problems [116]. This is one reason why DMET can have convergence problems when applied to inhomogeneous systems [116]. For such systems a simple single-shot embedding is usually performed [22], which still provides very good results for the energies, which is after all the target of the DMET method.

In SDE, we employ the same type of projection as in DMET but, since we are particularly targeting the density, we further introduce a partition that guarantees that all fragments connect smoothly to one another. Specifically, we define a continuous partition, where the system is covered by overlapping fragments as is depicted in Fig. 8. The idea of using overlaps to remove edges of a fragment was first introduced in Bootstrap Embedding [93], where densities of overlapping fragments are matched to one another though additional self-consistency loops. Here, we use a much simpler scheme. We sweep through the system by just going one grid point further for each fragment calculation and, when computing local observables such as the density, we only take into account the grid point in the middle of each fragment. Grid points at systems boundaries are included by considering non-local fragments, as exemplary depicted in purple in Fig. 8(a), that artificially connect the boundary regions. Hence, our partition is constructed such that the local observables are continuous on the real-space grid. The accuracy can be improved by selecting the grid spacing appropriately. In practice, this has to be balanced with the computational cost as for any real-space implementation.

[1] We show a numerical example in section 6.2.2

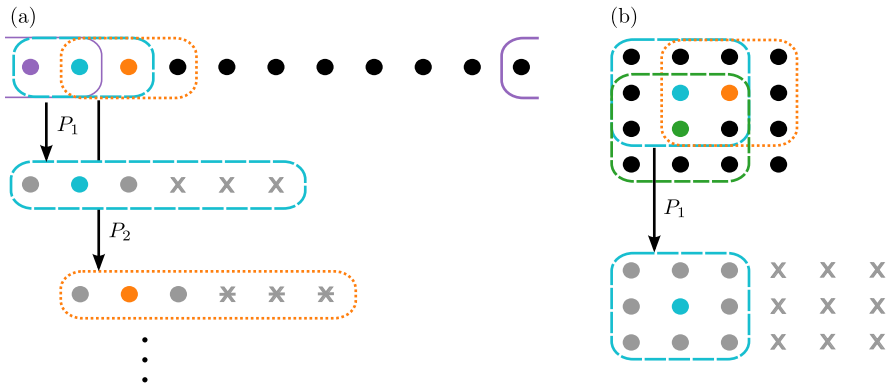

Figure 8. Visualization of the partition procedure: In order to obtain a continuous density, we sweep through the system by just going one site forward for each fragment calculation. Then, only the physical properties of the centering site are taken into account when considering local observables. The image (a) shows the partition in 1D and the image (b) illustrates the partition in 2D. Projections P_i onto embedded systems as well as effective CASs are explained in sections 3.3.1 and 5.2.2. This partition procedure can be extended to 3D in a straight-forward manner (not shown). Figure adapted from [88].

The introduced partitioning relies on a real-space formulation of the problem, as only there we have an intuitive notion of overlapping fragments and the subsequent separation into middle and edge sites. This notion has to be adapted for to more general basis sets in order to allow for application of SDE to arbitrary molecular systems. The BE method has done some steps in this direction with promising outcomes [117].

5.2.2 Modified single-particle projection

In section 3.3.1, we have introduced the single-particle projection as it is used in DMET. There, the set of correlated bath orbitals is obtained from a mean-field 1RDM via separating it as

$$\gamma = \left(\begin{array}{c|c} \gamma^{\mathrm{A}} & \gamma^{\mathrm{A-B}} \\ \hline \gamma^{\mathrm{A-B}\dagger} & \gamma^{\mathrm{B}} \end{array}\right) \tag{5.2}$$

and choosing those eigenstates $\tilde{\varphi}_k^B$ of γ^{B}, whose eigenvalues $\tilde{\lambda}_k$ lie between zero and two. These orbitals are then called correlated bath orbitals. In SDE, the global KS system plays the role of the mean-field 1RDM, from which these orbitals are constructed.

The number of correlated bath orbitals in the CAS is equal to N_{frag} as long as $2N_{\mathrm{frag}} < N_{\mathrm{e}} < 2\left(N - N_{\mathrm{frag}}\right)$ holds [118], otherwise their number is smaller. Since DMET was initially constructed for Hubbard-type lattice systems, for which the condition above mostly holds, in DMET the orbital construction that we introduced so far is used without modifications.

In SDE, we have to modify the orbital construction of DMET in order to get N_{frag} correlated bath orbitals regardless of the particle number N_{e}. For the low particle numbers that are considered here, we achieve this by artificially including correlations into the 1RDM of the full system by occupying higher-energy single-particle orbitals. In order to do so, we adjust the formula of Eq. (3.63) to

$$\gamma_{ij} = \sum_{k=1}^{N_{\mathrm{frag}}} \tilde{\varphi}_k^{B*}(i)\tilde{\varphi}_k^B(j) \cdot \begin{cases} 2 & \text{for } k < N_{\mathrm{e}}/2 - 1, \\ 2 - \eta(N_{\mathrm{frag}} - N_{\mathrm{e}}/2) & \text{for } k = N_{\mathrm{e}}/2, \\ \eta & \text{for } k > N_{\mathrm{e}}/2, \end{cases} \tag{5.3}$$

with some small value η and then continue with the orbital construction from diagonalizing

γ^{B} in Eq. (5.2) as before. The actual value of η is not of great importance[2] as it is only used to include higher-lying orbitals into the 1RDM and the same CAS would be obtained for different values of η.

Note that Eq. (5.3) is valid only for $N_{\mathrm{e}} < 2N_{\mathrm{frag}}$. For large particle numbers $N_{\mathrm{e}} > 2\left(N - N_{\mathrm{frag}}\right)$ the procedure can be adapted in a straight-forward manner due to particle-hole symmetry.

5.2.3 Fragment calculation

For each fragment i the full system is projected onto an embedded systems by means of a DMET-style single-particle projection (see sections 3.3.1 and 5.2.2), which is built from a global KS system. The embedding Hamiltonian $\hat{H}^i_{\mathrm{emb}}$ of each fragment, which is obtained as described in Eqs. (3.69)-(3.70), can be diagonalized with an accurate wave-function method. A simple exact-diagonalization solver that we use to obtain results presented later in this thesis, is given in appendix A.1.2. Hence, we obtain the embedding wave function $|\Psi^i_{\mathrm{emb}}\rangle$ of the fragment i, with the corresponding density n^i given as

$$n^i_\alpha = \sum_\sigma \langle \Psi^i_{\mathrm{emb}} | \hat{c}^\dagger_\alpha \hat{c}_\alpha | \Psi^i_{\mathrm{emb}} \rangle \quad \text{for } \alpha \in \mathrm{CAS}. \tag{5.4}$$

The correlated embedding wave functions can then be used not only to calculate the density, but any other observable such as the energy of the full system E_0. The energy of the full system E_0 can be approximated as a sum of fragment energies, which are calculated calculated from embedding wave-functions as described in section 3.3.2 and specifically in Eq. (3.71).

In the SDE approach for each fragment i only the middle site α_i is considered for obtaining properties of the full system (see section 5.2.1). The site value of an observable is calculated by tracing out all orbitals of the system except for the site α_i. An observable of the full system is then obtained as a sum over values for every site. Hence, taking for example the energy, we adopt the formulas in Eqs. (3.71)-(3.72) to

$$E_0 = \langle \hat{H} \rangle \approx \sum_i^N E_{\alpha_i} = \sum_i^N \left(\sum_{j=1}^N \gamma^i_{\alpha_i j} h_{\alpha_i j} + \frac{1}{2} \sum_{j,k,l=1}^N \Gamma^i_{\alpha_i jkl} W_{\alpha_i jkl} \right), \tag{5.5}$$

with

$$\gamma^i_{\alpha_i j} = \langle \Psi^i | \sum_\sigma \hat{c}^\dagger_{\alpha_i \sigma} \hat{c}_{j\sigma} | \Psi^i \rangle, \qquad \Gamma^i_{\alpha_i jkl} = \langle \Psi^i | \sum_{\sigma,\sigma'} \hat{c}^\dagger_{\alpha_i \sigma} \hat{c}^\dagger_{j\sigma'} \hat{c}_{l\sigma'} \hat{c}_{k\sigma} | \Psi^i \rangle \tag{5.6}$$

and

$$|\Psi^i\rangle = \hat{\Psi}^{i\,\dagger}_{\mathrm{emb}} |\widetilde{0}^i\rangle. \tag{5.7}$$

Here, $|\widetilde{0}^i\rangle$ corresponds to the Slater determinant build from occupied bath orbitals of each fragments. N is the number of fragments, which is equal to the number of grid points. With Eqs. (5.5)-(5.7), we have approximated the full wave function $|\Psi_0\rangle$ by a set of fragment wave-functions $\{|\Psi^i\rangle\}$. The correlation length that can be captured within this approximation, is limited by the fragment size.

The expression in Eq. (5.5) can be applied to any other observable. Thus, we circumvent the usual problem in DFT of finding the explicit dependence between an observable of interest O and the density n, i.e. the functional $O[n]$, by simply using the embedding wave functions instead of the density.

[2] In our implementation $\eta = 0.01$ is chosen.

Before moving on to improving the KS description of the full system, we have to add an additional constrain to the fragment calculations. We have to make sure that, when patching the system back together, we retain the correct particle number N_e in the full system

$$\langle \hat{N}_e \rangle - N_e \stackrel{!}{=} 0. \tag{5.8}$$

Following reference [22], we achieve this by adding and self-consistently optimizing a chemical potential μ to the embedding Hamiltonian of each fragment

$$\hat{H}^i_{\text{emb}} \rightarrow \hat{H}^i_{\text{emb}} + \mu \sum_{\alpha \in N_{\text{frag}}} \hat{n}_\alpha, \tag{5.9}$$

where $\hat{n}_\alpha$ denotes the density operator on site α and the index α runs over all fragment sites. The constant μ in Eq. (5.9)) is added only to the fragment part of the embedding Hamiltonian in order to achieve a correct particle distribution between fragment and environment. In other words, the chemical potential is a Lagrange multiplier, which assures that the constraint in Eq. (5.8)) is fulfilled.

In our implementation we use the secant method, details on which can be found in appendix A.1.4. Additionally, the optimization is not performed at every step of the algorithm, since it would involve unnecessary high numerical cost, but rather at the beginning and at the end of the self-consistency cycle, which we also explain in detail in A.1.4.

5.2.4 Global KS system from local potentials

So far, we have discussed how to project the full system onto a set of interacting embedded systems with $\{H^i_{\text{emb}} \leftrightarrow |\Psi^i_{\text{emb}}\rangle \leftrightarrow n^i_{\text{emb}}\}$ starting from some guess for the global KS potential v_{KS}. We now want to use this set of embedded quantities to update this KS potential.

For each fragment i the Hamiltonian contains a one-body part $\hat{h}^i_{\text{emb}}$ and a two-body part $\hat{W}^i_{\text{emb}}$

$$\hat{H}^i_{\text{emb}} = \hat{h}^i_{\text{emb}} + \hat{W}^i_{\text{emb}}, \tag{5.10}$$

Following the KS construction, the corresponding density n^i_{emb} can be reproduced by an auxiliary non-interacting system with

$$\hat{H}^i_{\text{emb,MF}} = \hat{h}^i_{\text{emb}} + \hat{v}^i_{\text{emb,Hxc}}[n^i_{\text{emb}}] \tag{5.11}$$

where the correlations are mimicked by the Hxc potential $\hat{v}^i_{\text{Hxc,emb}}$, that is defined as the difference of one-body terms of the interacting and the non-interacting systems. In practice, this potential is obtained either by analytical [119] or numerical inversion [109–113], or by a robust minimization routine as usually employed in DMET [22]. The analytical inversion scheme that is used to compute the results presented later in the thesis can be found in appendix A.1.3.

We then approximate the Hxc potential of the full system v_{Hxc} on each site α_i by the corresponding value of $\hat{v}^i_{\text{Hxc,emb}}$ on the same site

$$v_{\text{Hxc}}(\alpha_i) = \hat{v}^i_{\text{Hxc,emb}}(\alpha_i). \tag{5.12}$$

The KS potential is then updated[3] according to Eq. (5.1) as

$$\hat{v}_{\text{KS}}(\alpha_i) = \hat{v}_{\text{ext}}(\alpha_i) + \hat{v}^i_{\text{Hxc}}(\alpha_i). \tag{5.13}$$

This yields the new KS Hamiltonian $\hat{H}_{\text{KS}} = \hat{T} + \hat{V}_{\text{KS}}$, which is then used to obtain a new set of projections P_i.

[3] For technical details on the potential update see A.1.5.

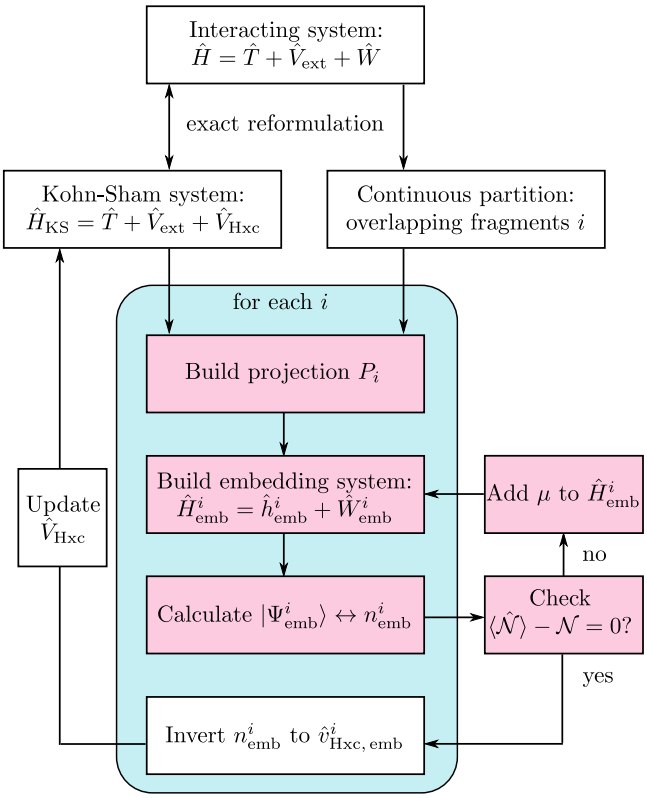

Figure 9. Visualization of the SDE algorithm: The full system can be uniquely mapped onto a non-interacting KS system. The system is divided into overlapping fragments such that a continuous reconstruction of the full system is possible. An initial guess for the global KS system is made, from which a projection is build for each fragment. Then, for each fragment the embedding Hamiltonian is calculated and the corresponding ground-state wave function and density are computed. A self-consistency cycle is added to maintain the correct particle number. As soon as the correct particle number is ensured in the full system, the density of every fragment is inverted and yields an updated v_{Hxc} on each site independently. This potential is then used to update the KS system. The procedure is repeated until self-consistency. In pink we mark those parts of the algorithm that are close to the DMET approach. Graphic adapted from [88].

The whole procedure is performed until convergence (see algorithm in Fig. 9). Eventually, we obtain an accurate density and KS potential from which also correlated observables can be calculated as described in Eq. (5.5). The SDE algorithm can be improved by increasing the fragment size and it converges to the exact solution. Note that the choice of reproducing accurately the density of the interacting embedded system by a non-interacting one, is crucial as it is based on rigorous one-to-one relations between densities and potentials in DFT and gives us a well defined target for the inversion[4]. This would not be the case with any other quantity such as e.g. the 1RDM (which is used in DMET), since the 1RDM of an interacting system cannot be reproduced exactly by a non-interacting one, as e.g. comprehensively discussed in reference [120].

The SDE algorithm is strongly inspired by DMET. Therefore, in order to illustrate the distinction between the two methods, we mark in Fig. 9 in pink, which parts of the algorithm SDE shares with DMET. Both methods coincide for fragment size $N_{\text{frag}} = 1$, as only then there is no difference in partition (single-site fragments cannot overlap) and also between density and 1RDM on the fragment (as there are no off-diagonal elements).

[4] Note, however, that this part of the algorithm has to be formulated in real space, since the one-to-one relations of DFT are given in real space.

To complete the introduction of the SDE method, we now turn to an estimate for its numerical cost. The cost of fragment calculations in SDE grows exponentially with the fragment size N_{frag} and the cost for the underlying calculation of the non-interacting system grows quadratically with the total number of grid points N. This has to be multiplied by the number of fragments, which is also N, and the needed self-consistency iterations η yielding a total scaling of $4^{2 \cdot N_{\text{frag}}} \cdot N^3 \cdot \eta$. This estimate has to be validated by additional studies and we assume that the actual numbers will as usual depend on implementational details as well as on the systems under consideration.

6 Application

The self-consistent density-functional embedding approach as developed in chapter 5 can in principle be applied to any closed system that is properly described by the Schrödinger equation in the BO approximation. In the following, we benchmark the method for simple model systems that on the one hand can be treated with numerically exact approaches and on the other hand exhibit features that are notoriously difficult to capture for standard KS DFT [119].

To this end, in section 6.1 we introduce model systems that mimic the two-electron bond stretching of homo- and heteroatomic molecules in one and two dimensions (1D and 2D, respectively). We then discuss the properties of the one-dimensional H_2 molecule in section 6.2, for which we show the dissociation curve, the densities, and the KS potentials in comparison to other established methods. In this particular case, we also study the convergence behavior of the SDE approach. Eventually, we apply the method to heteroatomic molecule models and 2D systems in sections 6.3 and 6.4, respectively.

6.1 Diatomic molecule models

We begin by introducing the 1D diatomic molecule model. There our system is discretized on the real-space (x) grid with an even number N of uniformly distributed sites in a finite volume L with zero-boundary conditions. The distance between two sites is accordingly given by $\Delta x = L/N$. The corresponding spatial (site) orbitals are (see Fig. 10(a) for visualization)

$$\varphi_i(x) = \frac{1}{\sqrt{\Delta x}}\Theta\left(\frac{\Delta x}{2} - \Big|\underbrace{\Delta x\left(i - \frac{N+1}{2}\right)}_{\equiv x_i} - x\Big|\right), \qquad \text{with } i \in \{1,\dots,N\}, \tag{6.1}$$

where Θ denotes the usual Heaviside step function. These basis function are often called B-splines of order $p = 0$ [121]. Having defined the single-particle basis, we can now consider the one- and two electron integrals defined in Eqs. (2.55)-(2.57) in order to obtain the model Hamiltonian.

For the one-electron integrals, we approximate the second derivative with second-order central finite-difference approximation

$$\left.\frac{\partial^2 f(x)}{\partial x^2}\right|_{x_i} \approx \frac{f(x_{i+1}) + f(x_{i-1}) - 2f(x_i)}{\Delta x^2} \tag{6.2}$$

and obtain

$$h_{ij} = \int dx\, \varphi_i^*(x)\left[-\frac{1}{2}\frac{\partial^2}{\partial x^2} + v_{\text{ext}}(x)\right]\varphi_j(x), = \begin{cases} \frac{1}{\Delta x^2} + v_{i,\text{ext}}, & \text{if } i = j, \\ -\frac{1}{2\Delta x^2}, & \text{if } |i-j| = 1, \\ 0, & \text{else,} \end{cases} \tag{6.3}$$

with $v_{i,\text{ext}} \equiv v_{\text{ext}}(x_i)$. The external potential $v_{\text{ext}}(x)$ mimics the electrostatic field of the nuclei

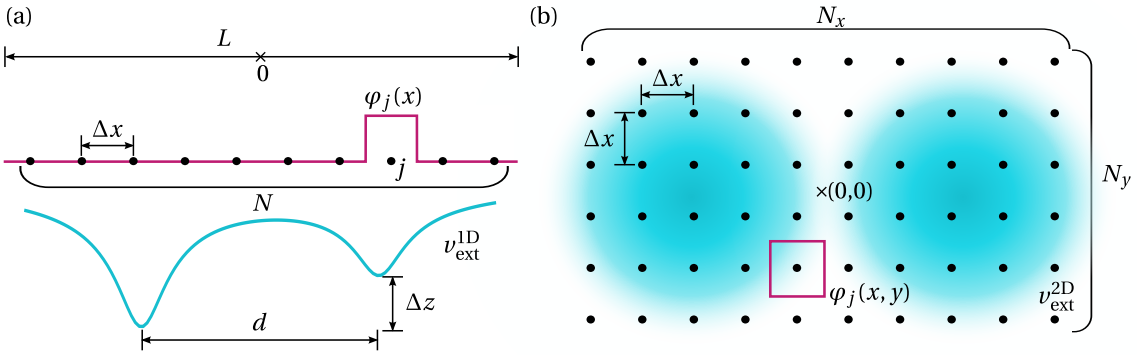

Figure 10. (a) Visualization of the one-dimensional heteroatomic molecule model. The real-space volume L is discretized on a grid with N sites with corresponding spatial orbitals $\varphi_j(x)$. The two atoms are modeled through a asymmetric double well potential $v_{\text{ext}}^{\text{1D}}$. The distance between the nuclei is given by d and the difference of two charges by Δz. (b) Generalization of the model to two dimensions. The space is discretized on a two-dimensional $N_x \times N_y$ grid (with total number of sites $N = N_x \cdot N_y$) and the nuclei are modeled by a two dimensional double-well potential $v_{\text{ext}}^{\text{2D}}$. Here, a homonuclear case ($\Delta z = 0$) is shown.

by a double-well potential. In 1D, it is given by

$$v_{\text{ext}}^{\text{1D}}(x_i) = -\frac{z_1}{\sqrt{\left(x_i - \frac{d}{2}\right)^2 + \alpha}} - \frac{z_2}{\sqrt{\left(x_i + \frac{d}{2}\right)^2 + \alpha}} + \frac{z_1 z_2}{2\sqrt{\left(d^2 + \alpha\right)}}, \tag{6.4}$$

where d is the distance between the two potential wells. The numbers z_1 and z_2 determine the depth of each well, respectively. In our case they take values between 0 and 2 and we will characterize the potential by their difference $\Delta z = z_1 - z_2$. Note that we chose the *soft-Coulomb* potential with some fixed softening parameter α instead of the true ($\sim 1/|x|$) electrostatic potential. This regularization prevents the model Hamiltonian from being unbounded. Moreover, the 1D soft-Coulomb potential is also known to closely mimic the behavior of realistic three-dimensional (3D) systems [122]. The potential is visualized in Fig. 10(a).

For the two-electron integrals of our model, we also use the soft-Coulomb interaction to mimic the repulsion of the electrons, which would otherwise have a singularity at $x = x'$. This wide-range interaction is therefore given by

$$W_{ijkl} = \int dx \int dx' \varphi_i^*(x)\varphi_j^*(x') \frac{1}{\sqrt{(x-x')^2 + \alpha}} \varphi_l(x')\varphi_k(x') = \frac{1}{\sqrt{\left(\Delta x(i-j)\right)^2 + \alpha}} \delta_{ik}\delta_{jl}. \tag{6.5}$$

We combine all of the above to obtain our 1D model Hamiltonian

$$\begin{aligned} \hat{H}_{\text{1D}} = &-\frac{1}{2\Delta x^2} \sum_{i,\sigma} \left(\hat{c}_{i+1,\sigma}^\dagger \hat{c}_{i,\sigma} + \hat{c}_{i,\sigma}^\dagger \hat{c}_{i+1,\sigma} - 2\hat{c}_{i,\sigma}^\dagger \hat{c}_{i,\sigma} \right) + \sum_{i,\sigma} v_{i,\text{ext}}^{\text{1D}} \hat{c}_{i,\sigma}^\dagger \hat{c}_{i,\sigma} \\ &+ \frac{1}{2\Delta x} \sum_{i,j,\sigma,\sigma'} \frac{1}{\sqrt{(i-j)^2 + \alpha}} \hat{c}_{i,\sigma}^\dagger \hat{c}_{j,\sigma'}^\dagger \hat{c}_{j,\sigma'} \hat{c}_{i,\sigma}, \end{aligned} \tag{6.6}$$

where $\hat{c}_{i,\sigma}^\dagger$ and $\hat{c}_{i,\sigma}$ are the usual creation and annihilation operators of an electron with spin σ on site i. The simplest way to model bond-stretching of a 1D molecule is to diagonalize the Hamiltonian in Eq. (6.6) in the two-electron Hilbert space. The exact diagonalization method that we employ as fragment solver for SDE as well as to obtain the numerically exact reference solution (later referred to as FCI) is outlined in appendix A.1.2.

The model Hamiltonian of Eq. (6.6) can be generalized to the 2D case by now considering a $N_x \times N_y$ real-space grid with following spatial orbitals

$$\varphi_i(x,y) = \varphi_{i_x}(x)\varphi_{i_y}(y) = \frac{1}{\Delta x}\Theta\left(\frac{\Delta x}{2} - \left|x_{i_x} - x\right|\right)\Theta\left(\frac{\Delta x}{2} - \left|y_{i_y} - y\right|\right), \tag{6.7}$$

with $i_x \in \{1,\dots,N_x\}$ and $i_y \in \{1,\dots,N_y\}$. Here, the coordinate x_{i_x} is defined as x_i in Eq. (6.1). We further choose the same spacing Δx for both x- and y-direction and therefore have

$$y_{i_y} \equiv \Delta x\left(i_y - \frac{N_y+1}{2}\right). \tag{6.8}$$

We obtain the Hamiltonian for the 2D case by replacing the index i in Eq. (6.6) by the double index (i_x, i_y) and further identifying

$$\begin{aligned} i+1 &\to (i_x+1, i_y), (i_x, i_y+1), \\ (i-j)^2 &\to (i_x - j_x)^2 + (i_y - j_y)^2. \end{aligned} \tag{6.9}$$

The external potential takes the form

$$v_{\text{ext}}^{\text{2D}}(x_i, y_i) = v_{\text{ext}}^{\text{1D}}(x_i) \cdot \frac{1}{\sqrt{y_{i_y}^2 + \alpha}} \tag{6.10}$$

accounting for both, the charge distribution of the ions in x- and in y-direction. The generalization of the model to the 2D case is depicted in Fig. 10(b).

In 2D and 3D the softening of the Coulomb potential is not necessarily required for the Hamiltonian to be well-defined. In such situations, the singularities in the Coulomb potential lead to the presence of cusps in the wave function and in the density at the positions of the nuclei [123], which can become important for modeling of certain situations such as high-harmonic generation [124]. In real-space based implementations, however, the grid always provides a cutoff for the Coulomb interaction, which qualitatively has the same effect as the softening. We therefore do not expect additional challenges coming from the singularities of the true Coulomb potential in *ab initio* calculations, at least as long as a real-space basis is employed.

Summarizing the above, the Hamiltonian for modeling diatomic molecules in 2D is given by

$$\begin{aligned} \hat{H}_{\text{2D}} = &-\frac{1}{2\Delta x^2}\sum_{i_x,i_y,\sigma} \hat{c}^\dagger_{(i_x+1,i_y),\sigma}\hat{c}_{(i_x,i_y),\sigma} + \hat{c}^\dagger_{(i_x,i_y+1),\sigma}\hat{c}_{(i_x,i_y),\sigma} + \hat{c}^\dagger_{(i_x,i_y),\sigma}\hat{c}_{(i_x+1,i_y),\sigma} + \hat{c}^\dagger_{(i_x,i_y),\sigma}\hat{c}_{(i_x,i_y+1),\sigma} \\ &+ \sum_{i_x,i_y,\sigma}\left(v^{\text{2D}}_{(i_x,i_y),\text{ext}} - \frac{1}{\Delta x^2}\right)\hat{c}^\dagger_{(i_x,i_y),\sigma}\hat{c}_{(i_x,i_y),\sigma} \\ &+ \frac{1}{2\Delta x}\sum_{i_x,i_y,j_x,j_y,\sigma,\sigma'} \frac{1}{\sqrt{(i_x-j_x)^2 + (i_y-j_y)^2 + \alpha}}\hat{c}^\dagger_{(i_x,i_y),\sigma}\hat{c}^\dagger_{(j_x,j_y),\sigma'}\hat{c}_{(j_x,j_y),\sigma'}\hat{c}_{(i_x,i_y),\sigma}\,. \end{aligned} \tag{6.11}$$

The main difference to the 1D case is that here we have hopping to four nearest neighbors to account for the kinetic energy of the electrons instead of hopping to two nearest neighbors in the 1D case.

Also in the 2D case, we diagonalize the Hamiltonian in the subspace of two electrons. For practical calculations, the 2D model introduced above is mapped onto an effective 1D model and the details for this mapping are given in appendix A.1.1 together with some technical details regarding partitioning in 2D.

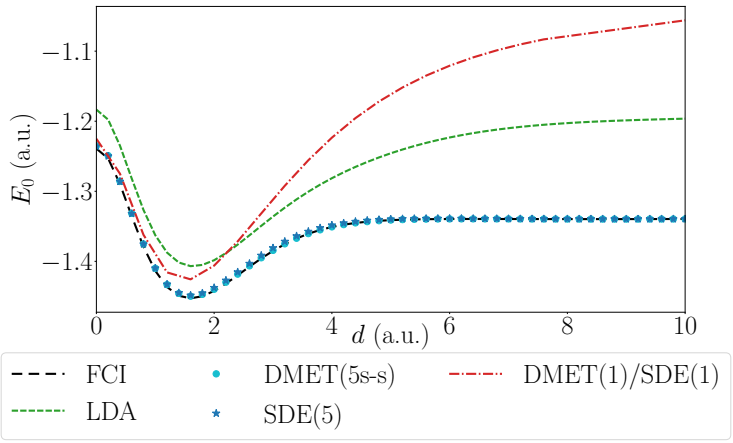

Figure 11. Ground-state energy of the 1D H_2 molecule, calculated with FCI (black dashes line), one dimensional LDA (green dashed line), five-sites single-shot DMET (turquoise circles), five-sites SDE (blue stars) and single-site DMET/SDE (red dash-dotted line). While LDA and DMET(1)/SDE(1) fail to describe the correct long-distance behavior, both DMET(5s-s) and SDE(5) show excellent agreement with the exact result. The following set of parameters has been used (see section 6.1 for details on model): number of real space grid sites $N = 120$, box size $L = 20$, potential well difference $\Delta z = 0$, softening parameter $\alpha = 1$. Plot was published in [88].

6.2 Properties of one-dimensional H_2 molecule

6.2.1 Dissociation curve

Common DFT functionals like LDA [9] or GGA [10, 75] fail to describe the dissociation limit of the H_2 molecule. This failure is attributed to the static correlation error, which is related to description of fractional spin states [125]. The issue can be understood by following the explanation of Cohen *et al.* [125]: consider the closed-shell H_2 molecule at the dissociation limit. Half of this molecule is an an exotic system with fractional spins, namely a H atom with half a spin-up electron and half a spin-down electron. The energy of this system though should be exactly the same as of a H atom with an integer-spin state. This fact can be generalized to the constancy condition for the exact functional: systems with fractional spins should have the same energy as systems with integer spins. Common approximate functionals, however, violate this condition and predict wrong energies for fractional spin states resulting in the wrong dissociation limit.

Although there are methods such as the strictly-correlated electron functional [126], functionals based on RPA [127, 128] and on *GW* combined with RPA [129], or the exchange-correlation potential by Baerends *et. al.* [109, 130], which are able to describe strong static correlations in specific cases, modeling the bond stretching of H_2 remains a challenging test for any new functional.

In Fig. 11, we show how the SDE method performs in this test case. We plot the ground-state energy of the Hamiltonian in Eq. (6.6) with $\Delta z = 0$ as function of interatomic distance d calculated with exact diagonalization (ED or FCI in the following), one-dimensional LDA-DFT [131], one-site DMET (DMET(1)) that is equivalent to one-site SDE (SDE(1))[1], single-shot DMET with five fragment sites (DMET(5s-s)), and five-site SDE (SDE(5)). For both SDE and DMET the initial guess for the projection is build from the one-body part of the Hamiltonian in Eq. (6.6). The exact energy curve shows the following well-known behavior: when varying the distance of the two core potentials d, the curve has a minimum corresponding to a stable molecule. For

[1] DMET(1) is the only version of DMET that we could apply to the model systems studied here self-consistently. It is also the only case in which DMET and SDE results coincide (see section 5.2.4 for a detailed discussion).

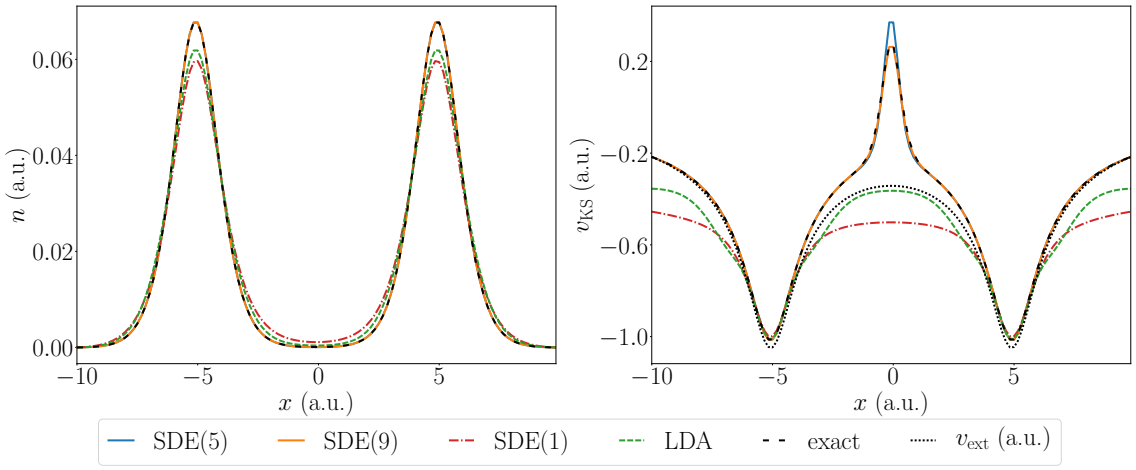

Figure 12. Bond-stretching of a symmetric molecule. Plotted are the density distribution $n(x)$ and the KS potential $v_{KS}(x)$ obtained with SDE(5) (blue solid line), SDE(9) (orange solid line), SDE(1) (red dash-dotted line), LDA (green dashed line) and FCI (black dashes line). The exact and the SDE solutions for fragments sizes larger than one agree quantitatively. The SDE KS potential in these cases shows the expected peak in the center which mimics the electron-electron interaction. For $N_{frag} = 5$, this peak is slightly overestimated, but converges quickly to a quantitatively exact result for $N_{frag} = 9$. The SDE(1) and LDA results on the other hand differ significantly from the exact solution. The peak in the KS potential is missing completely. The following set of parameters has been used: $N = 120$, $L = 20$, $d = 10$, $\Delta z = 0$, $\alpha = 1$. Data published in [88].

smaller core distances, the energy grows due to the repulsion of the two cores. Increasing the distance $d \to \infty$ leads to the vanishing of the binding energy resulting in two separate atoms.

As discussed above, LDA does not predict the correct dissociation behavior of H_2 due to the static correlation error, the energy of the two separated atoms is overestimated. One-site embedding methods DMET(1)/SDE(1) also fail to describe this behavior correctly as static correlation cannot be captured with such small fragment sizes. They perform even worse than LDA for large distances.

In contrast, both SDE and single-shot DMET show excellent agreement with FCI for $N_{frag} = 5$. Both curves are on top of the FCI result. DMET even results in slightly better energies for intermediate distances. This might seem surprising at first glance, but the SDE algorithm is optimized to provide good densities and potentials and, as widely discussed in the literature [12], this does not necessarily go hand in hand with more accurate energies. The difference in energy between SDE and DMET is, however, negligible and in the next section we show that SDE, indeed does provide excellent densities and KS potentials.

6.2.2 Capturing the peak of the exact KS potential

The KS potential of a two-electron system stretched in space exhibits signatures of strong static correlation between the molecular fragments [109, 119, 130]. In case of the symmetric H_2 molecule, this signature is the appearance of a peak between the two potential wells. The peak originates from the kinetic correlation term and its purpose lies in preventing the tunneling of non-interacting KS particles between the two H atoms, which for real electrons is taken care of by their Coulomb repulsion [119].

In Fig. 12, we plot the density and the KS potential of the stretched H_2 molecule obtained with SDE for fragment sizes of 1, 5 and 9 sites and compare them with the exact and with LDA-DFT results. The density from the SDE calculations for the two larger fragment sizes agrees quantitatively with the exact density. We also see a peak at position $x = 0$ in the KS poten-

tial for both SDE(5) and SDE(9) calculations. This peak is slightly overestimated for $N_{\text{frag}} = 5$, but agrees quantitatively with the exact solution as the fragments gets bigger ($N_{\text{frag}} = 9$). The SDE(1)/DMET(1) results are also plotted. As already has been the case for the energy (see Fig. 11), both density and potential deviate strongly from the exact solution. The peak in the KS potential accounting for strong correlations in the system is missing completely and, hence, also the density distribution deviates strongly from the exact solution. The same applies to results obtained with LDA.

With this, we have shown that not only does the SDE scheme converge, but also it accurately reproduces the peak in the KS potential, which is challenging for most DFT approximations.

6.2.3 Comparison with standard DMET implementations

In this section, we compare SDE densities and KS potentials to the ones from our real-space implementation of single-shot DMET that showed good results for ground-state energies of the model. Note that, the DMET correlation potential u (see section 3.3.3 for its definition) is not supposed to be the KS potential. We still include it in the comparison for completeness on the one hand and to show an example of how SDE differs from DMET in practice on the other hand.

In Fig. 13, we plot the deviation of the approximate densities Δn and potentials Δu from the exact ones for both methods for $N_{\text{frag}} = 5$. Note that in DMET the embedding potential u is in general non-local and not unique, as it is solely used to approximate the projection and is not targeted itself by the method. In DMET, we further consider two different types of matching [22] to obtain the potentials: matching of the interacting and non-interacting 1RDM on the fragment (γ-matching, see also section 3.3.3) and matching of only the corresponding densities (n-matching). In case of γ-matching, the embedding potential u is non-local and we compare only its diagonal to the exact KS potential v_{KS}.

We observe that the DMET density deviates stronger from the exact solution than the SDE den-

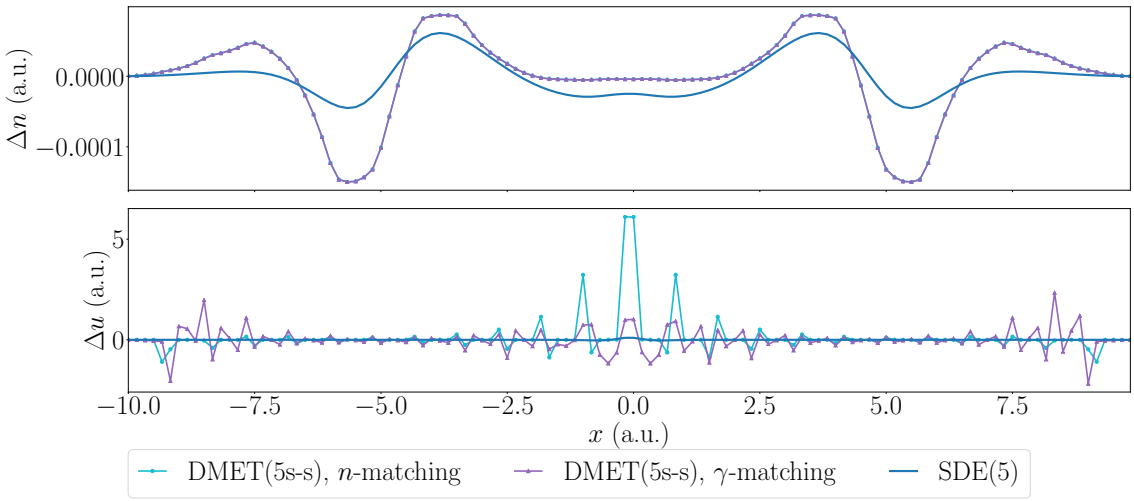

Figure 13. Deviation of densities Δn and potentials Δu from FCI reference results for five-site SDE (blue solid line) and five-site single-shot DMET with two approaches to obtain the potential: density matching (turquoise solid line with circles) and 1RDM matching (violet solid line with triangles). For the densities both DMET results are on top of each other as they do not depend on the type of matching in the first embedding shot. DMET results for the potentials exhibit striking discontinuities that result from discontinuous densities. This is not surprising as the target of DMET is not to obtain a global description of a system through a KS potential. SDE results show smooth behavior for both density and KS potential. The following set of parameters has been used: $N = 120$, $L = 20$, $d = 10$, $\Delta z = 0$, $\alpha = 1$.

sity. Furthermore, in DMET we clearly see a peculiarly shaped density, especially at fragment boundaries. This behavior is caused by the fact that there is no smooth connection between the fragments. This comparison reveals the need of our type of partitioning in order to have accurate densities.

The discontinuity of both DMET embedding potentials is even more pronounced. The strongest deviations appear at fragment boundaries as there embedding potentials have to connect different basis sets of the fragments (site basis) and correlated bath orbitals. In case of γ-matching we further observe asymmetric behavior of the embedding potential although both the external potential and the density are symmetric. This behavior is a clear signature of ambiguities in matching the 1RDMs on the fragment in DMET that we discussed in section 3.3.4. In case of single-shot embedding, the potentials, however, are never used and they are also not targeted by the DMET method. The issues of discontinuity and ambiguity of γ-matching have to be fixed though, if the method needs to be applied self-consistently or if it aims to calculate accurate densities and KS potentials. Both these aims are achieved within the SDE approach.

6.2.4 Convergence behavior

In this section we show that the results obtained with our self-consistent density functional embedding can be improved by increasing the size of the fragments. Moreover, from our numerical evidence we deduce that this improvement is systematic. In Fig. 14 and 15, we plot the deviation of SDE results from the exact solution for different properties Q of the system, integrated over the whole space

$$\Delta Q = \sum_i \left| Q_i^{\mathrm{SDE}} - Q_i^{\mathrm{exact}} \right| \cdot \Delta x. \tag{6.12}$$

In Fig. 14, we plot the deviation of the density Δn and the KS potential Δv_{KS} between the SDE calculation and the exact result. We consider two different core distances ($d = 0$ and $d = 10$),

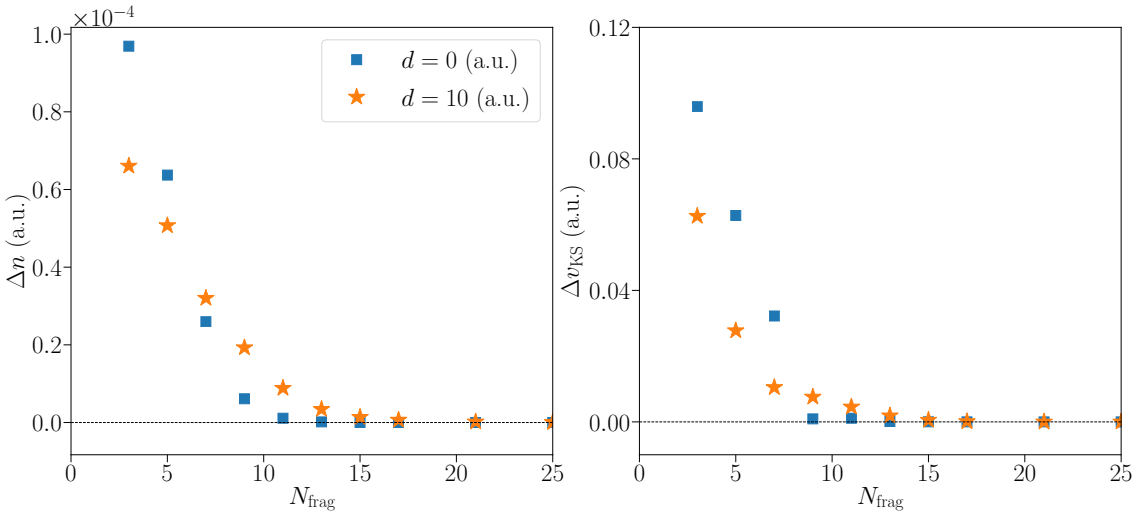

Figure 14. Integrated deviation of the density (upper graph) and the KS potential (lower graph) of the SDE calculation from the exact solution for weakly static correlated ($d = 0$) and strongly static correlated electrons ($d = 10$). In both cases, we observe a decrease in the error between the two calculations. While in the weakly correlated case the error estimate is higher for small fragments and decreases faster, in the strongly correlated case already the calculations for small fragments are very good and decrease slower. Already for ($N_{\mathrm{frag}} = 3$), the error is of the order of $\Delta n \leq 10^{-4}$. Parameters for $d = 0$: $N = 120$, $L = 10$, $\Delta z = 0$, $\alpha = 1$; parameters for $d = 10$: $N = 120$, $L = 20$, $\Delta z = 0$, $\alpha = 1$. Data published in [88].

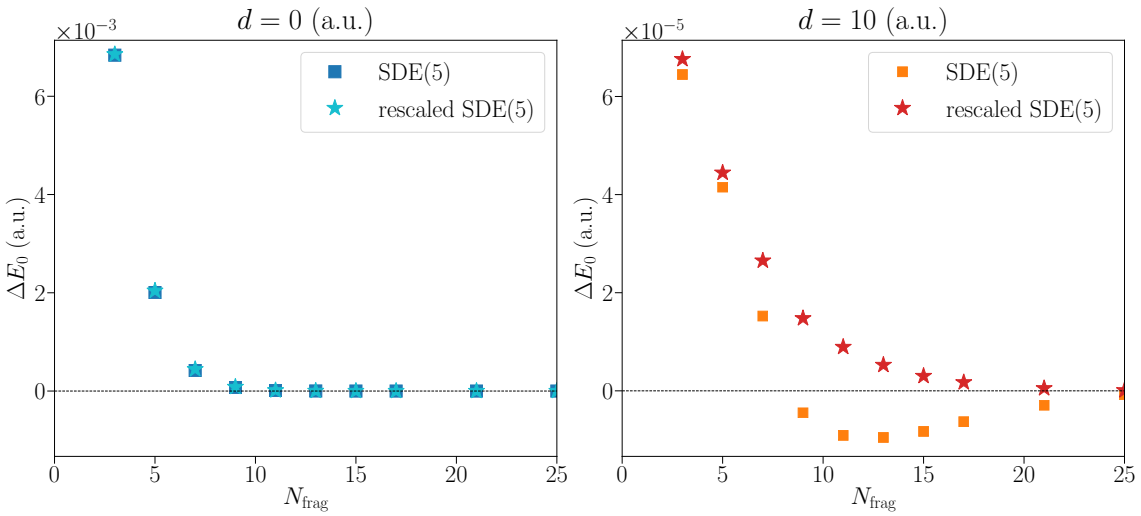

Figure 15. Difference of the total energy between the SDE and the exact solution ΔE_0 with and without rescaling with respect to the particle number. We consider two different core distances ($d = 0$, upper graph and $d = 10$, lower graph), which correspond to weak and strong correlation between the electrons. For the weakly static correlated system, already for $N_{\text{frag}} = 9$, the error between the two calculations is below our selected accuracy limit. For strongly static correlated electrons, $d = 10$, we observe that the energy estimate of the SDE calculations for $N_{\text{frag}} \geq 9$ is too low compared to the exact solution. The deviation in energy is very low for small fragment sizes ($\Delta E_0 \leq 10^{-5}$). Parameters for $d = 0$: $N = 120$, $L = 10$, $\Delta z = 0$, $\alpha = 1$; parameters for $d = 10$: $N = 120$, $L = 20$, $\Delta z = 0$, $\alpha = 1$. Data published in [88].

which correspond to weak and strong static correlation between the electrons. In both cases and for both chosen properties, we observe a monotonous decrease in ΔQ with increasing fragment size up to a quantitative agreement of the two solutions. Already for the smallest considered fragment size $N_{\text{frag}} = 3$, the deviations are relatively small, that is of the order of the fourth digit for the density $\Delta n \leq 10^{-4}$ and of the order of the first digit for the KS potential $\Delta v_{\text{KS}} = 10^{-1}$.

In Fig. 14, we show the deviation of the total energy E_0 of the SDE method from the exact calculation. Again, we consider one example with weakly static correlated electrons and one example with strongly static correlated electrons. For weakly correlated electrons, the difference in energy decreases and already for an fragment size of $N_{\text{frag}} = 7$, the deviation from the exact solution is below chemical accuracy of 1.6 mhartree.

For strongly (static) correlated electrons, we observe that the SDE energy becomes smaller than the exact energy for a range of fragments between $N_{\text{frag}} = 9$ and $N_{\text{frag}} = 20$. This is because the SDE method is not variational and the estimate for the energy therefore can also be lower than the exact energy. Also for this observable though, already for small fragments our estimate is of order $\Delta E_0 \leq 10^{-5}$hartree, which is far below chemical accuracy.

Since we approximate the wave function of the full system by a set of fragment wave functions, the total particle number calculated with fragment wave functions is not necessarily correct. The employed optimization of the chemical potential leads to the correct number for $\langle \hat{N}_e \rangle$ up to a desired accuracy ($|\langle \hat{N}_e \rangle - \hat{N}_e| < 10^{-5}$). As the energy difference is of the same order of magnitude, we further rescale the energy with respect to the particle number

$$E_0^{\text{SDE}} \to E_0^{\text{SDE}} \cdot \hat{N}_e / \langle \hat{N}_e \rangle, \tag{6.13}$$

to see if we achieve a better convergence behavior. We indeed do, as we can also see in Fig. 15. Nonetheless, the calculated energy can still be lower than the exact energy, meaning that we still observe the non-variational nature of our approximation.

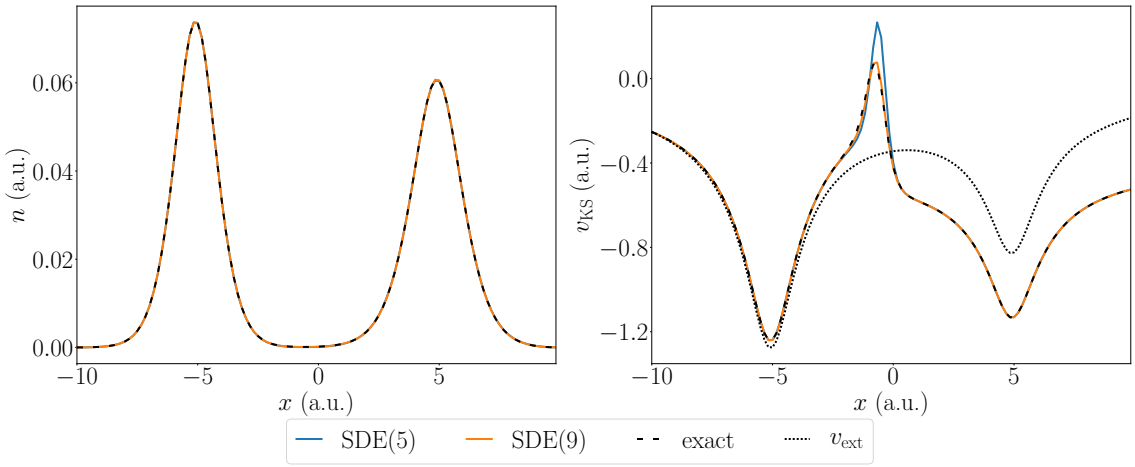

Figure 16. Bond-stretching of a heteroatomic molecule. Plotted are the density distribution $n(x)$ and the KS potential $v_{KS}(x)$ for an asymmetric external potential obtained with SDE(5) (blue solid line), SDE(9) (orange solid line) and FCI (black dashes line). Both SDE results agree with the exact solution and show expected peak and step in the KS potential. The following set of parameters has been used: $N = 120$, $L = 20$, $d = 10$, $\Delta z = 0.5$, $\alpha = 1$.

6.3 KS potential for heteroatomic molecules

As the next challenge we consider a generalization of the system studied in the previous section, namely bond stretching of heteroatomic molecules such as LiH. These systems can also be modeled by the Hamiltonian of Eq. (6.6) by considering an asymmetric external potential. The SDE results for densities and KS potentials of such systems are plotted in Fig. 16. As already in the symmetric case, we observe excellent agreement with exact results for both density and potential. We observe an asymmetric density distribution, which is mimicked by a KS potential that, in addition to the peak observed in the symmetric case in Fig. 12, has a step between the two wells. The appearance of the step and its importance in KS DFT is to this day a widely discussed issue in the literature [132–135].

Even though approximate functionals, e.g. those based on the exact-exchange approximation, do reproduce the step in the KS potential [136], to the best of our knowledge, so far there does not exist any approximate energy functional that can reproduce both peaks and steps of the exact KS potential at the same time [137]. Within the SDE approach we achieve both claims and that is why we believe that with SDE we provide a new path towards accurate KS potentials even for strongly correlated systems.

6.4 Application to two-dimensional models

Here, we continue benchmarking the performance of the SDE approach by addressing higher-dimensional systems, such as model H_2 and model heteroatomic molecule in two dimensions.

In Fig. 17, we plot the density n, the KS potential v_{KS}, the external potential v_{ext}, the Hxc potential v_{Hxc}, and deviations from the exact solution Δn and Δv_{Hxc} for the two-dimensional H_2 model. We observe a homogeneous density distribution around the two core potentials that is consistent with the external potential. The Hxc potential which mimics the interactions of the electrons as well the kinetic correlations in the interacting case, shows a peak in the middle of the molecule. Our observations are consistent with the exact solution of this problem.

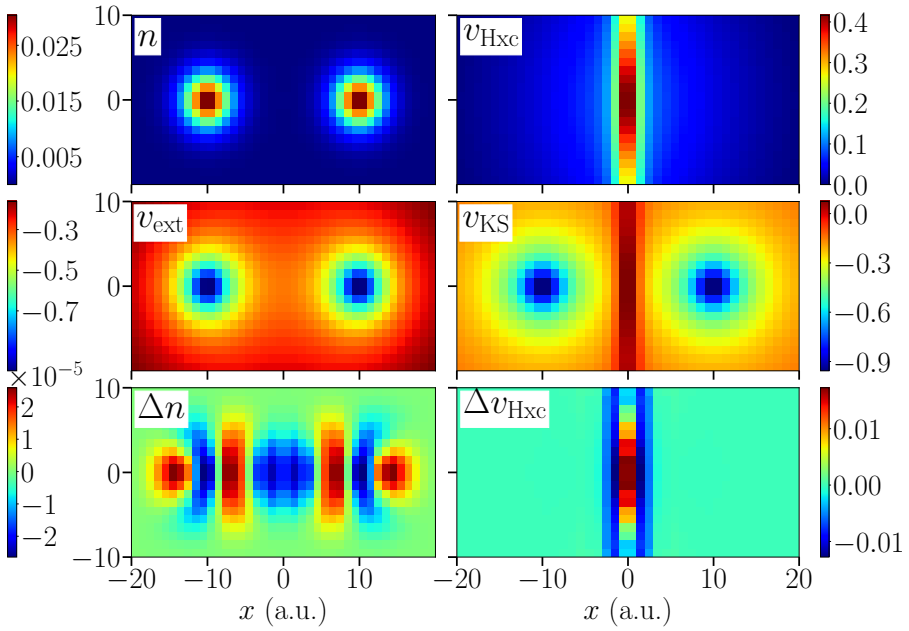

Figure 17. The H_2 molecule in two dimensions. Plotted are the density n, the Hartree-exchange-correlation potential v_{Hxc}, as well as their difference from the exact reference Δn and Δv_{Hxc}, respectively, the KS potential v_{KS}, and the external potential v_{ext} with SDE(4×4). We observe a homogeneous density consistent with the external potential. v_{Hxc} shows the peak accounting for the interactions of the two electrons. We observe good agreement with the exact reference. The following set of parameters has been used: $N_x = 40$, $N_y = 20$, $L_x = 20$, $L_y = 10$, $d = 10$, $\Delta z = 0$, $\alpha = 1$. Plot published in [88].

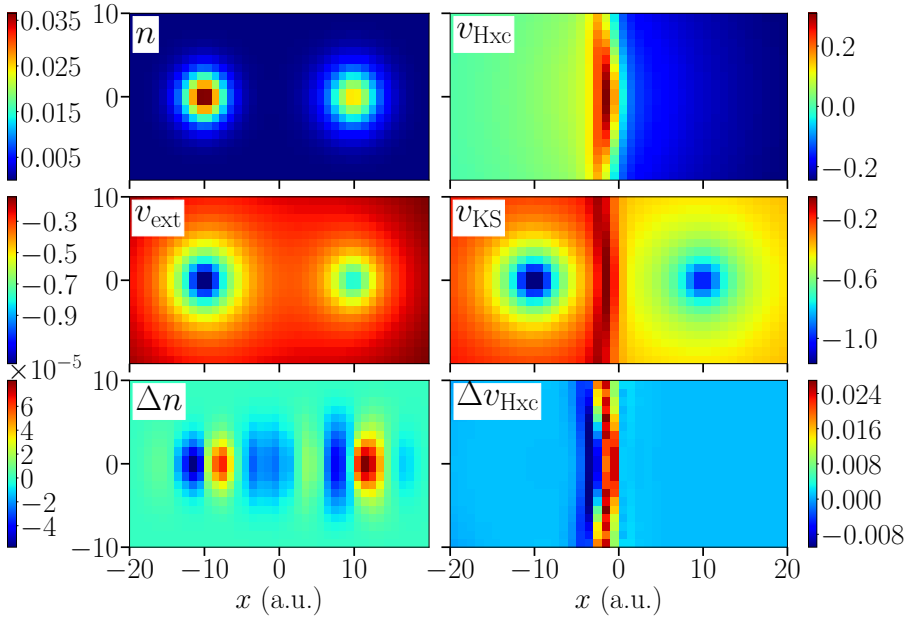

Figure 18. Heteroatomic molecule in two dimensions. Plotted are the density n, the Hartree-exchange-correlation potential v_{Hxc}, as well as their difference from the exact reference Δn and Δv_{Hxc}, respectively, the KS potential v_{KS}, and the external potential v_{ext} with SDE(4×4). We observe an asymmetric density consistent with the external potential. v_{Hxc} again shows the peak accounting for the interactions of the two electrons. Additionally, a step accounting for the asymmetric distribution of the density can be observed. Again, we observe good agreement with the exact reference. The following set of parameters has been used: $N_x = 40$, $N_y = 20$, $L_x = 20$, $L_y = 10$, $d = 10$, $\Delta z = 0.5$, $\alpha = 1$. Plot published in [88].

For a model heteroatomic molecule, we plot the same properties as for H_2 in Fig 18. The density for the heteroatomic molecule in the two-dimensional case is asymmetrically distributed between the two cores, again consistent with the external potential. In the Hartree-exchange-correlation potential, additional to the peak accounting for the interaction of the electrons, we also observe a step that accounts for the asymmetric distribution of the density.

7 Summary and future steps

With our novel self-consistent density-functional embedding, we have developed a method that leaves the realm of standard energy-functional approaches in DFT and paves the way for unconventional functional development. Instead of yet another energy functional, the method directly targets the density to potential mapping that lies at the heart of KS DFT. To this end we divide the target system into overlapping local fragments. By using a DMET-inspired projection, these fragments can then be addressed independently with exact denationalization techniques. Based on rigorous relations in DFT, local fragment properties are then used to approximate the density and the KS potential of the global system in a self-consistent manner. Through the set of the obtained correlated fragment wave functions, we additionally have a way of calculating ground-state observables of the global system that are not easily accessible with standard DFT approximations.

As a crucial step in *ab initio* method development, we have provided proof-of-principle benchmark calculations for model systems, for which a comparison with numerically exact results is accessible. To this end, we have considered two-electron systems in one- and two dimensions. For these models, SDE demonstrates results comparable in accuracy to FCI already for moderate fragment sizes. Thereby, not only we can very accurately reproduce the exact potential energy surfaces, but also all signatures of strong correlation that are present in the exact KS potentials. This makes SDE e.g. the first approximate DFT approach to exhibit both peaks and steps in the KS potential at the same time [137], which is necessary for an accurate description of molecular dissociations. Additionally, from our numerical evidence the SDE method seems to exhibit another feature that is lacking in standard DFT approaches. It appears to be systematically improvable by increasing the size of the fragments and moreover it converges to the exact solution.

An implementation of the SDE approach that would allow for calculating real 3D molecules needs to address the additional challenges, that we review in the following.

To calculate larger fragment sizes and particle numbers, more efficient solvers have to replace the simple exact diagonalization approach that we so far use to obtain the fragment wave functions. These can either be provided by more efficient exact diagonalization approaches [18, 138, 139], or accurate approximate methods such as DMRG [71, 140] (for strong correlations) and CC [141, 142] (for weaker correlations). While this might improve the computational scaling of the overall approach, the use of approximate solvers will most probably result in less accurate ground-state densities that can cause instabilities due to the subsequent density-inversion procedure, as it is very sensitive to changes in the density. Overall, a balance between computational cost and accuracy has to be maintained and additional studies are necessary to quantify this.

The exact analytic inversion scheme that we use for the update of the global KS potential from the fragment wave functions is unfortunately only valid in case of two electrons. Hence, to treat larger particle numbers with SDE, the analytic inversion scheme has to be substituted by a numeric one, as e.g. proposed in [109–113] for small atoms and molecules, or simply be replaced by a robust but less accurate optimization scheme as in conventional DMET [22]. Finding a numerically stable inversion algorithm that at the same time is accurate enough for

our purpose will probably become one of the main challenges in future developments of the method.

Both extensions outlined above will allow to treat realistic molecular systems that are discretized on a 3D real-space grid. In such situations, a vast amount of basis states is required to properly describe the molecule, which makes storage and manipulation of one- and two-electron integrals numerically demanding, but in principle still feasible, since many comparable approaches successfully employ real-space grids [143–146].

One possible strategy to avoid transformations of two-electron tensors is given by the non-interacting bath formulation of DMET [22] that circumvents the treatment of the interaction tensor for the full system altogether. Following this spirit, development of novel projection techniques that are not based on the KS Slater determinant, which is the case now, but rather on the density or the 1RDM of the global system might be a promising route for a further advancement. Such an approach would utilize the formally exact framework of DFT (or the one of the reduced density-matrix functional theory (RDMFT)) even more efficiently.

Another way to approach realistic systems is to replace the real-space basis by more suitable quantum chemistry basis sets. This, however, would require a novel strategy on how to define overlapping fragments and the related continuous partition in such a basis. In a resent work [117], Ye *et al.* proposed a generalized notion of overlapping fragments for generic *ab initio* Hamiltonians in the framework of their bootstrap embedding. The definition is based on a heuristic interaction-based metric that determines the interorbital connectivity and we believe that similar concepts can be utilized for SDE, providing another promising path for the method.

Part III:

Coupled-cluster theory for light-matter interaction

In this part of the thesis, we propose an extension of CC theory that enables accurate treatment of coupled light-matter systems. We introduce the ingredients for such an extension and develop a numerical framework to test the theory. We apply the developed *polaritonic coupled-cluster theory* to ground- and excited-state properties of simple model systems and compare the results to FCI calculations. Extension of the theory beyond simple model systems and its scaling are also discussed. This part of the thesis is based on the publication [147].

8 Method

In the following, we will discuss how the standard quantum chemical CC theory can be extended to the treatment of coupled fermion-boson, or specifically in our case, electron-photon systems. As discussed in chapter 4, Hamiltonians that we consider are fixed-nucleus molecular systems interacting with photonic fields in the non-relativistic dipole approximation. Here, using the quantum harmonic oscillator relations $\hat{q} = (2\omega_k)^{-\frac{1}{2}} \left(\hat{a}^\dagger + \hat{a}\right)$ and $\hat{p} = -i\sqrt{\omega/2}\left(\hat{a}^\dagger - \hat{a}\right)$, we slightly rewrite the Hamiltonian given in Eq. (4.50) to

$$\hat{H} = \hat{H}_\mathrm{e} + \sum_\alpha \left[\omega_\alpha \hat{a}_\alpha^\dagger \hat{a}_\alpha - \gamma_\alpha \omega_\alpha \hat{d}\left(\hat{a}_\alpha^\dagger + \hat{a}_\alpha\right) + \gamma_\alpha^2 \omega_\alpha \hat{d}^2\right]. \tag{8.1}$$

Additionally, we have summarized the mode and polarization indices $\lambda, \boldsymbol{k}$ to the index α and introduced the normalized light-matter interaction strength $\gamma_\alpha \equiv (\boldsymbol{e}_\alpha \cdot \boldsymbol{e}_{\boldsymbol{d}}) \left(\sqrt{2\omega_\alpha}\varepsilon_0 V\right)^{-1}$ [34]. The constant γ_α includes the projection of the mode polarization $\boldsymbol{e}_\alpha$ onto the direction $\boldsymbol{e}_{\boldsymbol{d}}$ of the molecular dipole moment. The molecular dipole operator $\hat{d}$ is an electronic one-body operator of a general form $\hat{d} = \sum_{i,j,\sigma} d_{ij} \hat{c}_{i\sigma}^\dagger \hat{c}_{j\sigma}$. Additionally, we omit the photonic zero-point energy $\sum_\alpha \frac{\omega_\alpha}{2}$ in Eq. (8.1) that would yield just a shift in energy.

In the following, we develop a general framework for polaritonic CC theory. We discuss how the three main ingredients – reference state, excitation operators, and cluster operator – of the standard electronic CC theory can be adapted to the new situation. For simplicity and since these are often settings utilized in cavity QED [34], we will involve only one photonic mode $\omega_\alpha = \omega_c$ into our derivation. Considerations regarding the straightforward multi-mode extension of the theory as well as its overall practicability are discussed in section 8.2.

8.1 Ingredients for polaritonic CC theory

8.1.1 Reference state

In standard purely electronic CC theory (see section 3.1.3), a single Slater determinant is used as a reference state. Usually, the HF Slater determinant $|\Phi_0\rangle = |\Phi_0^\mathrm{e}\rangle$ is chosen, as it is a mean-field solution that is energetically the closest to the actual ground-state and as it is assumed to cover the coarse electronic structure of the system.

For the coupled electron-photon system, similar considerations apply. As a reference, we choose a product state between an electronic reference $|\widetilde{\Phi}_0^\mathrm{e}\rangle$ and a photonic reference $|\widetilde{\Phi}_0^\mathrm{p}\rangle$

$$|\Phi_0\rangle = |\widetilde{\Phi}_0^\mathrm{e}\rangle \otimes |\widetilde{\Phi}_0^\mathrm{p}\rangle. \tag{8.2}$$

These components can be obtained as mean-field solutions of (single-mode) Eq. (8.1), which would mean finding mean-field solutions for the following two coupled Hamiltonians

$$\hat{H}_\mathrm{e}^\mathrm{MF} = \hat{H}_\mathrm{e} + \gamma^2\omega_c\hat{d}^2 - \gamma\omega_c\hat{d}\langle\,\hat{a}^\dagger + \hat{a}\,\rangle + \langle\hat{H}_\mathrm{p}\rangle \quad \hat{H}_\mathrm{p}^\mathrm{MF} = \omega_c\,\hat{a}^\dagger\hat{a}\;\; - \gamma\omega_c\langle\hat{d}\rangle\left(\hat{a}^\dagger + \hat{a}\right) + \langle\hat{H}_\mathrm{e}\rangle, \tag{8.3}$$

where the expectation values are built with the respective other mean-field state, e. g. $\langle\,\hat{a}^\dagger + \hat{a}\,\rangle \mathrel{\widehat{=}} \langle\widetilde{\Phi}_0^\mathrm{p}|\,\hat{a}^\dagger + \hat{a}\,|\widetilde{\Phi}_0^\mathrm{p}\rangle$ or $\langle\hat{d}\rangle \mathrel{\widehat{=}} \langle\widetilde{\Phi}_0^\mathrm{e}|\hat{d}|\widetilde{\Phi}_0^\mathrm{e}\rangle$.

The matter-dependent photonic mean-field Hamiltonian describes a shifted harmonic oscillator. Its ground state is given by the following coherent state

$$|\widetilde{\Phi}_0^{\mathrm{p}}\rangle = e^{z\hat{a}^\dagger - z\hat{a}}|0\rangle = e^{-|z|^2/2}\sum_{n=0}^{\infty}\frac{z^n}{\sqrt{n!}}|n\rangle, \tag{8.4}$$

where the displacement $z = \gamma\langle\hat{d}\rangle$ is determined by the electrons. The photonic part of the theory would then be formulated in terms of generalized coherent states, that are basically Fock-number states that are built with respect to the state defined in Eq. (8.4) instead of the bare vacuum [148].

The electronic mean-field solution would remain a HF Slater determinant, but of a new Hamiltonian

$$\hat{H}_{\mathrm{e}}^{\mathrm{MF}} = \hat{H}_{\mathrm{e}} + \gamma^2\omega_c\left(\hat{d}^2 - \hat{d}\langle\hat{d}\rangle\right) + \langle\hat{H}_{\mathrm{p}}\rangle \tag{8.5}$$

containing additional terms that result from coupling to the photonic mode. Note that $\hat{H}_{\mathrm{e}}^{\mathrm{MF}}$ depends on $|\widetilde{\Phi}_0^{\mathrm{e}}\rangle$ through the photonic shift $\gamma\langle\hat{d}\rangle$ and has to be updated at each step in the HF calculation.

In the following, we omit this step of finding the coupled mean-field solution by choosing an even simpler reference state, namely one for the zero-coupling case where the mean-field Hamiltonians are given by

$$\hat{H}_{\mathrm{e}}^{\mathrm{MF(0)}} = \hat{H}_{\mathrm{e}}, \qquad \hat{H}_{\mathrm{p}}^{\mathrm{MF(0)}} = \hat{H}_{\mathrm{p}}. \tag{8.6}$$

With these Hamitonians, the reference solution is given by a simple product of the electronic HF Slater determinant $|\Phi_0^{\mathrm{e}}\rangle$ and the photonic vacuum $|0\rangle$.

$$|\Phi_0\rangle = |\Phi_0^{\mathrm{e}}\rangle \otimes |0\rangle. \tag{8.7}$$

The above approximation is justified by the fact that the coupling usually has quite a small impact on the ground state of the coupled system (we will discuss this in section 10.3) and *a posteriori* by the excellent performance of polaritonic CC theory (see section 10.4).

8.1.2 Bosonic excitation operators

As we have discussed in section 3.1.3, the equality of the product ansatz and the exponential ansatz in standard CC theory is guaranteed, if excitation operators $\hat{\tau}^\mu$ meet the conditions of

$$\text{Commutativity:} \qquad [\hat{\tau}_\mu, \hat{\tau}_\nu] = 0; \tag{8.8}$$

$$\text{Nilpotency:} \qquad \left(\hat{\tau}_\mu\right)^2 = 0. \tag{8.9}$$

The natural excitation operator for a bosonic mode is simply the creation operator $\hat{a}^\dagger$, but the lack of nilpotency ($(\hat{a}^\dagger)^2 \neq 0$) means that a formalism based on $\hat{a}^\dagger$ would lack the simple structure of electronic CC theory. However, if the number of photons in the system is limited to a finite number n_{max}, which is anyway necessary for numerical treatment of bosons in the basis of Fock number states (see section 9.1.1 for details), it is possible to map one bosonic mode to a lattice of $n_{\mathrm{max}}+1$ sites $\{|0\rangle, |1\rangle, \ldots, |n_{\mathrm{max}}\rangle\}$, each corresponding to a Fock number state. In this case the excitation operators

$$\hat{\tau}_n = |n\rangle\langle 0| \tag{8.10}$$

clearly fulfill both the commutativity and nilpotency condition, while allowing any number state to be addressed (see Fig. 19). For a basis cut-off n_{max}, we obtain in total n_{max} excitation operators $\hat{\tau}_n$ for one bosonic mode. This framework can be understood as a *fermionization*.

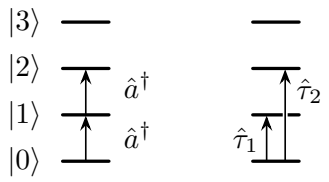

Figure 19. Two types of excitation operators for a bosonic degree of freedom. Both can be used to access any number state, and both are sets of commutative operators. Note that the operators $\hat{\tau}_n$ are additionally nilpotent, simplifying CC formulations that use this form. Graphic published in [147].

One bosonic mode is represented by *exactly one* additional fermion with some exotic spin. This particle can occupy in total $n_{\max}+1$ orbitals, but excitation operators can only excite it from the lowest orbital corresponding to $|0\rangle$.

Additionally, bosonic excitation operators defined in Eq. (8.10) can be generalized to a coherent-state basis in a straight-forward manner, if a coherent state given in Eq. (8.4) is chosen as a photonic reference (see section 8.1.1 and [148]).

8.1.3 Cluster operator

Now, to build CC theory for electron-photon systems, we introduce a more general cluster operator

$$\hat{T} = \sum_{\mu} t_\mu \hat{\tau}_\mu + \sum_{n} t_n \hat{\tau}_n + \sum_{\tilde{\mu},\tilde{n}} t_{\tilde{\mu}\tilde{n}} \hat{\tau}_{\tilde{\mu}} \hat{\tau}_{\tilde{n}} \equiv \sum_{\kappa} t_\kappa \hat{\tau}_\kappa, \tag{8.11}$$

in which the electronic terms $\hat{\tau}_\mu$ as introduced in Eq. (3.6) are supplemented by purely photonic excitations $\hat{\tau}_n$ defined in Eq. (8.10) and connected light-matter excitations $\hat{\tau}_{\tilde{\mu}}\hat{\tau}_{\tilde{n}}$. The tilde emphasizes the fact that although the coupled excitation operators are products of fermionic and photonic operators, the sum can run over a different set of values $\tilde{\mu}$ and $\tilde{n}$. Note that the set of coupled amplitudes $t_{\tilde{\mu}\tilde{n}}$ is independent of purely electronic amplitudes t_μ and purely photonic amplitudes t_n. To every operator entering the extended cluster operator in Eq. (8.11) we assign a new index κ.

To describe the truncation of each term in the cluster operator, we introduce following terminology for acronyms in polaritonic CC theory: CC–*'fermionic-excitation-level'–'photonic-excitation-level'–'connected-excitation-level'*. More specifically, in chapter 10 we will use the following acronyms:

- **CC-SD-S-0:** refers to a superposition of electronic singles $\hat{c}_a^\dagger \hat{c}_i$ and doubles $\hat{c}_b^\dagger \hat{c}_a^\dagger \hat{c}_i \hat{c}_j$, and photonic singles $|n\rangle\langle 0|$ without any coupled excitations;
- **CC-SD-S-D:** stands for electronic singles $\hat{c}_a^\dagger \hat{c}_i$ and doubles $\hat{c}_b^\dagger \hat{c}_a^\dagger \hat{c}_i \hat{c}_j$, photonic singles $|n\rangle\langle 0|$, and connected doubles $\hat{c}_a^\dagger \hat{c}_i \otimes |n\rangle\langle 0|$;
- **CC-SD-S-DT:** denotes electronic singles $\hat{c}_a^\dagger \hat{c}_i$ and doubles $\hat{c}_b^\dagger \hat{c}_a^\dagger \hat{c}_i \hat{c}_j$, photonic singles $|n\rangle\langle 0|$, connected doubles $\hat{c}_a^\dagger \hat{c}_i \otimes |n\rangle\langle 0|$ and triples $\hat{c}_b^\dagger \hat{c}_a^\dagger \hat{c}_i \hat{c}_j \otimes |n\rangle\langle 0|$.

These abbreviations reflect the fact that for single-mode problems the photonic excitation level is at most singles. Multi-photon excitations within that single mode, however, are included due to the structure of the corresponding excitation operators defined in Eq. (8.10). Also, the level of connected excitations is at least doubles as at least single electronic and single photonic excitation have to be included.

The form of the energy and amplitude equations in polaritonic CC theory remains the same as in the standard CC approach. We recall Eqs. (3.16)-(3.17)

$$\langle\Phi_0|e^{-\hat{T}}\hat{H}e^{\hat{T}}|\Phi_0\rangle = E_0, \qquad \langle\Phi_\kappa|e^{-\hat{T}}\hat{H}e^{\hat{T}}|\Phi_0\rangle = 0, \tag{8.12}$$

with the reference state defined in Eq. (8.2) or Eq. (8.7), respectively, and the extended cluster operator as introduced above. The EOM-CC approach to excited states of a system also remains unchanged by the extension to photons.

8.2 Scaling and multi-mode considerations

To complete the general introduction of the developed CC theory for light-matter interaction, we here discuss its general scaling and how a multi-mode extension can be realized.

The polynomial scaling of CC theory is attributed to the fact that usually a polynomial number of excitation operators enters $\hat{T}$ and that the Baker-Campbell-Hausdorff expansion of the ST Hamiltonian truncates at fourth order due to the form of the underlying molecular Hamiltonian (see section 3.1.3 and [61] for details). The same arguments apply to light-matter Hamiltonians, since the individual photonic creation and annihilation operators are quadratic expressions in the excitation operators

$$\hat{a} = \sum_{n=1}^{n_{\max}} \sqrt{n}\,\hat{\tau}_{n-1}\hat{\tau}^\dagger_n, \qquad \hat{a}^\dagger = \sum_{n=1}^{n_{\max}} \sqrt{n}\,\hat{\tau}_n\hat{\tau}^\dagger_{n-1}. \tag{8.13}$$

Therefore, the free-field part in the single-mode version of Eq. (10.1) becomes a one-body interaction

$$\omega_c\,\hat{a}^\dagger\hat{a} \;= \sum_{n=1}^{n_{\max}} \omega_c n\,\hat{\tau}_n\hat{\tau}^\dagger_n \tag{8.14}$$

and the light-matter part a two-body interaction

$$\sum_{i,j,\sigma} \gamma\omega_c d_{ij}\hat{c}^\dagger_{i\sigma}\hat{c}_{j\sigma}\left(\hat{a}^\dagger + \hat{a}\right) = \sum_{i,j,\sigma}\sum_{n=1}^{n_{\max}} \gamma\omega_c d_{ij}\sqrt{n}\left(\hat{c}^\dagger_{i\sigma}\hat{c}_{j\sigma}\hat{\tau}_{n-1}\hat{\tau}^\dagger_n + \hat{c}^\dagger_{i\sigma}\hat{c}_{j\sigma}\hat{\tau}_n\hat{\tau}^\dagger_{n-1}\right), \tag{8.15}$$

respectively.

Thus, the equations of e.g. polaritonic CC-SD-S-DT theory are effectively identical to a subset of the conventional CCSDT equations, but with removal of exchange diagrams and inclusion of alternative values in place of two-electron integrals. The CC energy equation (Eq. (3.20)) in CC-SD-S-DT, for instance, becomes

$$E_{\text{CC-SD-S-DT}} = \widetilde{E}_{\text{CCSD}} - \sum_{ia}\gamma\omega_c d_{ai}\left(t^a_{i,\,1} + t^a_i t_1\right). \tag{8.16}$$

Here, t^a_i is the amplitude of the electronic excitation $\hat{c}^\dagger_a\hat{c}_i$, t_1 the one of the photonic excitation $|1\rangle\langle 0|$ and $t^a_{i,\,1}$ the one of the connected excitation $\hat{c}^\dagger_a\hat{c}_i \otimes |1\rangle\langle 0|$. Note that only excitations with a maximum of one photon contribute to the energy as only one-photon excitations enter the Hamiltonian. By the tilde in $\widetilde{E}_{\text{CCSD}}$ we denote the fact that the dipole self-interaction has to be included in its evaluation.

For algebraic expressions for the CCSDT amplitude equations we refer to literature, e.g. [60]. The computationally most expensive terms included in those equations are associated with connected triple excitations like the term $\sum_{abcd}\langle ab||de\rangle\, t^{dec}_{ijk}$, that scales roughly as $N^8 \sim N^5_{\text{emp}} \cdot N^3_{\text{occ}}$. In CC-SD-S-DT this term translates to

$$\sum_{n=1}^{n_{\max}}\sum_{abcd}\left(\langle ab||de\rangle - \gamma\omega_c d_{ad}\sqrt{n}\right) t^{de}_{ij,\,n}, \tag{8.17}$$

which scales as $N^6 \cdot n_{\max}$. Usually, the photonic cut-off is much smaller than the number of electronic orbitals[1] and therefore we can argue that the scaling of CC-SD-S-DT is roughly the same as the $\mathcal{O}(N^6)$ scaling of conventional CCSD theory.

An extension of the theory to multiple photonic modes is straightforward. Photons that belong to different modes are distinguishable and therefore adding a photonic mode to a theory would simply mean having an additional *single* exotic particle that represents this mode (see discussion in section 8.1.2). The cluster operator would have to be extended accordingly, where naturally additional levels of truncation would be possible.

This multi-mode polaritonic CC theory would scale exponentially with the number of considered photonic modes, which is not a big issue, since in most cavity QED applications only few photonic modes have to be considered. A reduction to a polynomial scaling, however, should be possible e.g. by modifying the cluster operator and the set of considered excited states.

[1] The quantum character of light comes into play, when few photons are involved. For large photon numbers, a classical description of light is mostly sufficient.

9 Implementation

In this chapter, we provide step-by-step instructions for our computational realization of polaritonic CC theory. How vector-matrix representations of all involved states and operators (and therefore defining equations for CC and FCI theories) are constructed, is discussed in section 9.1. It is important to stress, that our implementation serves as a numerical proof of concept and has no claim of computational efficiency. The method, as implemented in the course of this project, scales exponentially with the system size. However, as discussed in section 8.2, this scaling can be reduced to a polynomial one using the same techniques as in standard CC theory.

An algorithm for solving the CC equations is given in section 9.2. Additionally, in section 9.3 we briefly discuss the problem of (close-to-)degenerate eigenstates of the ST Hamiltonian and develop a correction method for this issue.

9.1 Operator construction

9.1.1 Creation and annihilation operators

Fermionic operators

As discussed in section 2.2.3, for a given finite set of spin-orbitals quantum mechanics is reduced to simple linear algebra on the Fock space of the problem. Intuitively, one would start by labeling every possible basis state in the Fock space (Slater determinant as defined in Eq. (2.22))

$$|\Phi_k\rangle \rightarrow (0,\ldots,0,\underset{\substack{\uparrow\\ k\text{th position}}}{1},0,\ldots,0)^{\mathrm{T}} \tag{9.1}$$

and determine matrix representations of operators (see Eq. (2.26)) according to this labeling. This procedure becomes rather cumbersome very fast with larger basis sizes, since the labeling is completely arbitrary.

Therefore, here we use a slightly different approach. We first construct matrix representations of particle-creation and annihilation operators and then label the states according to these matrices. For fermions this can be done systematically in terms of the *Jordan-Wigner transformation* [149] as follows

$$\begin{aligned}
\hat{c}_{1\uparrow} &= \mathbb{1}\otimes\cdots\otimes\mathbb{1}\otimes\mathbb{1}\otimes\sigma_+, & \hat{c}^\dagger_{1\uparrow} &= \mathbb{1}\otimes\cdots\otimes\mathbb{1}\otimes\mathbb{1}\otimes\sigma_-,\\
\hat{c}_{1\downarrow} &= \mathbb{1}\otimes\cdots\otimes\mathbb{1}\otimes\sigma_+\otimes\sigma_z, & \hat{c}^\dagger_{1\downarrow} &= \mathbb{1}\otimes\cdots\otimes\mathbb{1}\otimes\sigma_-\otimes\sigma_z,\\
\hat{c}_{2\uparrow} &= \mathbb{1}\otimes\cdots\otimes\sigma_+\otimes\sigma_z\otimes\sigma_z, & \hat{c}^\dagger_{2\uparrow} &= \mathbb{1}\otimes\cdots\otimes\sigma_-\otimes\sigma_z\otimes\sigma_z,\\
&\vdots & &\vdots\\
\hat{c}_{N\downarrow} &= \sigma_+\otimes\cdots\otimes\sigma_z\otimes\sigma_z\otimes\sigma_z, & \hat{c}^\dagger_{N\downarrow} &= \sigma_-\otimes\cdots\otimes\sigma_z\otimes\sigma_z\otimes\sigma_z.
\end{aligned} \tag{9.2}$$

The ingredients above are

$$\sigma_+ = \begin{pmatrix} 0 & 1 \\ 0 & 0 \end{pmatrix}, \qquad \sigma_- = \begin{pmatrix} 0 & 0 \\ 1 & 0 \end{pmatrix}, \qquad \sigma_z = \begin{pmatrix} 1 & 0 \\ 0 & -1 \end{pmatrix}, \qquad \mathbb{1} = \begin{pmatrix} 1 & 0 \\ 0 & 1 \end{pmatrix}, \tag{9.3}$$

and N again denotes the number of spatial orbitals in the basis. The matrices σ_-, σ_+ play the role of creation and annihilation operators for a single spin-orbital and σ_z ensures that the matrices obey the necessary fermionic anti-commutator relations introduced in Eq. (2.34).

Note that here operator indices are assigned arbitrarily. This indexing, however, now determines the labeling of basis states $|\Phi_k\rangle$ in the Fock space. The vacuum in this scenario is given by $|0\rangle \mathrel{\hat{=}} (1,0,\cdots,0)^{\mathrm{T}}$ and each Slater determinant consisting of a set of spin orbitals $\{(i,\sigma)\}$ can be constructed as

$$|\Phi_{\{(i,\sigma)\}}\rangle = \sum_{\{(i,\sigma)\}} \hat{c}^\dagger_{i,\sigma}|0\rangle \mathrel{\hat{=}} (0,\ldots,0,\underset{\substack{\uparrow \\ \{(i,\sigma)\} \mapsto k}}{1},0,\ldots,0)^{\mathrm{T}} \mathrel{\hat{=}} |\Phi_k\rangle \tag{9.4}$$

with the bijective mapping $\{(i,\sigma)\} \mapsto k$. The explicit knowledge of this mapping is mostly of no practical use, since we are usually not interested in the explicit expansion of a wave function in terms of Slater determinants but rather in observables, which all can be expressed in terms of particle creation and annihilation operators as discussed in section 2.3.

However, it proves to be useful to reorder the basis states according to their particle number. The particle-number operator is given by a diagonal matrix

$$\sum_\sigma \sum_{k=1}^{N} \hat{c}^\dagger_{i,\sigma}\hat{c}_{i,\sigma} \mathrel{\hat{=}} \begin{pmatrix} 0 & & \\ & \ddots & \\ & & n_i \\ & & & \ddots \end{pmatrix}, \qquad \text{with } n_i \in \{0,\ldots,2N\}. \tag{9.5}$$

The frequency of occurrence of every n_i is given by the size of the corresponding fermionic n_i-particle Hilbert space, namely $\binom{2N}{n_i}$ (see Eq. (2.20) and corresponding discussion). Per construction, the order in which the numbers n_i occur is somewhat arbitrary. Therefore, we introduce a (symmetric) permutation matrix $P = P^T$ that reorders the diagonal entries of the particle-number operator in ascending order

$$P \begin{pmatrix} 0 & & \\ & \ddots & \\ & & n_i \\ & & & \ddots \end{pmatrix} P = \begin{pmatrix} 0 & & & & & & \\ & 1 & & & & & \\ & & 1 & & & & \\ & & & \ddots & & & \\ & & & & 2 & & \\ & & & & & 2 & \\ & & & & & & \ddots \\ & & & & & & & 2N-1 & \\ & & & & & & & & 2N \end{pmatrix}. \tag{9.6}$$

This permutation is equivalent to reordering the basis states $|\Phi_k\rangle$ with respect to their particle number. Creation and annihilation operators defined in Eq. (9.2) have to be transformed accordingly

$$\hat{c}_{i,\sigma} \to P\hat{c}_{i,\sigma}P, \qquad \hat{c}^\dagger_{i,\sigma} \to P\hat{c}^\dagger_{i,\sigma}P. \tag{9.7}$$

After this transformation, all matrices exhibit a particular block structure, which is shown exemplary for $N = 4$ spatial orbitals in Fig. 20. Operators that conserve the number of particles in the system have non-zero entries only *within* a block-diagonal. The individual blocks in this diagonal are of square shape and their sizes are given by the size of the corresponding n_i-electron Hilbert space (Eq. (2.19)).

Creation and annihilation operators build the *first upper* ($\hat{c}$) and the *first lower* ($\hat{c}^\dagger$) block diagonals, such that they connect states that differ by one particle. This consideration, which is

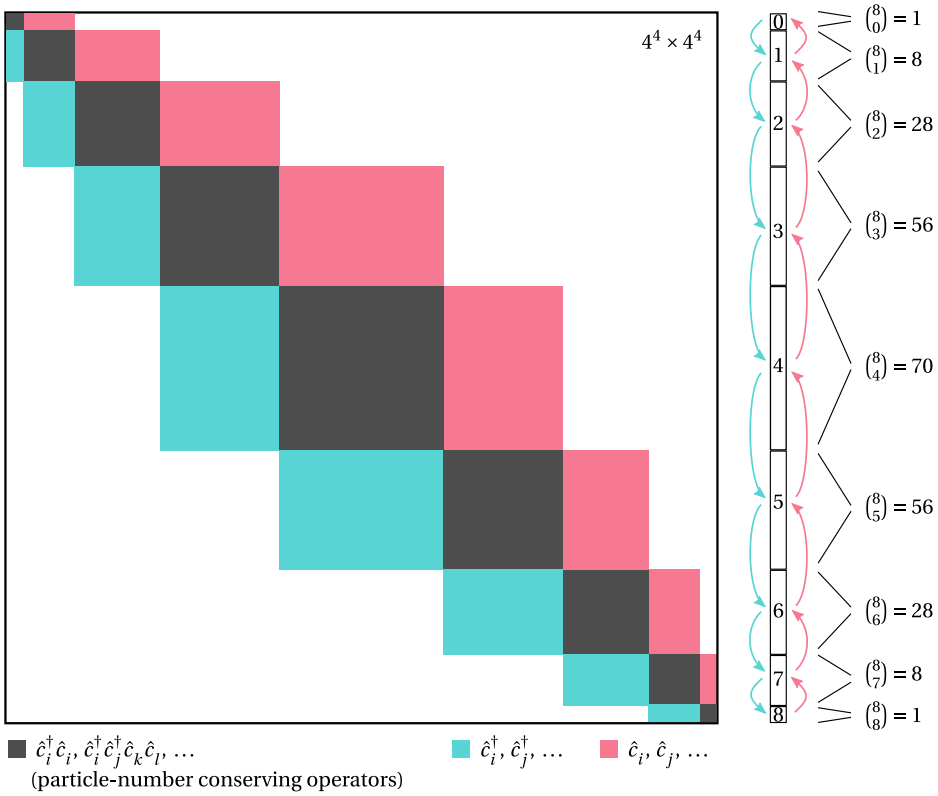

Figure 20. Visualization of a state (vector) and an operator (matrix) in the full fermionic Fock space built from $N = 4$ spatial orbitals in a vector-matrix representation. The diagonal blocks, which are depicted in gray, correspond to non-vanishing matrix elements of particle-number conserving operators. Blocks that contain non-zero matrix elements of creation and annihilation operators are depicted in turquoise and pink, respectively. They connect all neighboring particle-number blocks. Block sizes are determined by binomial coefficients (see Eq. (2.20)).

also visualized in Fig. 20, illustrates the following important fact: while particle creation and annhilation operators are obliged to be constructed in the full Fock space, particle-number conserving operators, such as electronic Hamiltonians considered in this thesis, can be represented by the individual particle-number blocks. This significantly reduces the dimensionality of the problem, in the example shown in Fig. 20 from $4^4 = 256$ states in the Fock space to maximum of 70 states in the subspace of 4 electrons.

In a similar manner, other symmetries of the electronic Hamiltonian, such as the total spin of the system, can be used for an additional block-diagonalization of its matrix representation.

Bosonic operators

Matrix representations of bosonic operators are constructed as follows. For a single mode we assign a unit vector to every Fock-number state $|n\rangle$ in ascending order, starting with the vacuum state

$$|0\rangle \mathrel{\widehat{=}} (1, 0, \cdots, 0)^{\mathrm{T}}. \tag{9.8}$$

Matrix representations of bosonic creation and annihilation operators then simply follow from Eq. (4.28) and are given by

$$\hat{a} = \begin{pmatrix} 0 & \sqrt{1} & 0 & 0 & \cdots \\ 0 & 0 & \sqrt{2} & 0 & \cdots \\ 0 & 0 & 0 & \sqrt{3} & \ddots \\ \vdots & \vdots & \vdots & \ddots & \ddots \end{pmatrix}, \qquad \hat{a}^\dagger = \begin{pmatrix} 0 & 0 & 0 & \cdots \\ \sqrt{1} & 0 & 0 & \cdots \\ 0 & \sqrt{2} & 0 & \cdots \\ 0 & 0 & \sqrt{3} & \ddots \\ \vdots & \vdots & \ddots & \ddots \end{pmatrix}. \tag{9.9}$$

These matrices are in principle infinite, since a bosonic mode can be occupied by any number of particles. In practice, however, these matrices have to be truncated after some number of photons $n_{\max}$ and their dimension then reduces to $n_{\max}+1$.

This truncation of the photonic Fock space leads to a violation of the following bosonic commutator relation

$$[\hat{a}\ , \hat{a}^\dagger] = \hat{a}\,\hat{a}^\dagger - \hat{a}^\dagger\hat{a}\ \neq \mathbb{1}, \tag{9.10}$$

which is caused by a wrong matrix representation of the first term

$$\hat{a}\,\hat{a}^\dagger = \begin{pmatrix} 1 & & \\ & \ddots & \\ & & n_{\max} \end{pmatrix} \neq \begin{pmatrix} 1 & & \\ & \ddots & \\ & & n_{\max} \end{pmatrix}, \tag{9.11}$$

The particle number operator $\hat{a}^\dagger\hat{a}$, on the contrary, has the correct structure

$$\hat{a}^\dagger\hat{a}\ = \begin{pmatrix} 0 & & \\ & \ddots & \\ & & n_{\max} \end{pmatrix}. \tag{9.12}$$

Therefore, the impact of the outlined issue can be minimized by always maintaining the *normal ordering* of bosonic operators. This means that all creation operators have to be placed to the left of all annihilation operators in every product of operators. Regardless of the above, convergence of the results with respect to the photon number cut-off $n_{\max}$ has to be checked.

I think in addition, still convergence of the results with respect to the number of included basis states has to be checked.

Matrix representations of bosonic excitation operators defined in Eq. (8.10) are given by

$$\hat{\tau}_1 = \begin{pmatrix} 0 & 0 & \cdots & 0 \\ 1 & 0 & \cdots & 0 \\ 0 & 0 & \cdots & 0 \\ \vdots & \vdots & \ddots & \vdots \\ 0 & 0 & \cdots & 0 \end{pmatrix}, \quad \hat{\tau}_2 = \begin{pmatrix} 0 & 0 & \cdots & 0 \\ 0 & 0 & \cdots & 0 \\ 1 & 0 & \cdots & 0 \\ \vdots & \vdots & \ddots & \vdots \\ 0 & 0 & \cdots & 0 \end{pmatrix}, \quad \cdots, \quad \hat{\tau}_{n_{\max}} = \begin{pmatrix} 0 & 0 & \cdots & 0 \\ 0 & 0 & \cdots & 0 \\ \vdots & \vdots & \ddots & \vdots \\ 0 & 0 & \cdots & 0 \\ 1 & 0 & \cdots & 0 \end{pmatrix}. \tag{9.13}$$

If required, an extension to a multi-mode case for all bosonic operators is straight-forward and we will briefly outline it in the following. Similar to the electronic case in Eq. (9.2), matrix representations of bosonic creation and annihilation operators for M modes are given by

$$\begin{aligned} \hat{a}_1 &= \mathbb{1}\otimes\cdots\otimes\mathbb{1}\otimes\mathbb{1}\otimes\hat{a}, & \hat{a}_1^\dagger &= \mathbb{1}\ \otimes\cdots\otimes\mathbb{1}\otimes\mathbb{1}\ \otimes\hat{a}^\dagger, \\ \hat{a}_2 &= \mathbb{1}\otimes\cdots\otimes\mathbb{1}\otimes\hat{a}\otimes\mathbb{1}, & \hat{a}_2^\dagger &= \mathbb{1}\ \otimes\cdots\otimes\mathbb{1}\otimes\hat{a}^\dagger\otimes\mathbb{1}\ , \\ &\vdots & &\vdots \\ \hat{a}_M &= \hat{a}\otimes\cdots\otimes\mathbb{1}\otimes\mathbb{1}\otimes\mathbb{1}, & \hat{a}_M^\dagger &= \hat{a}^\dagger\otimes\cdots\otimes\mathbb{1}\otimes\mathbb{1}\ \otimes\mathbb{1}\ . \end{aligned} \tag{9.14}$$

Here, fermionic ladder operators σ_+ and σ_- have been replaced by their bosonic analogs $\hat{a}$ and $\hat{a}^\dagger$ and the fermionic matrix σ_z is replaced by an identity matrix $\mathbb{1}$ of the same dimension as a and $a^\dagger$ to ensure commutativity of the resulting operators. Photonic cut-offs and therefore matrix dimensions can be chosen individually for each mode. Bosonic excitation operators can be extended to the multi-mode case in the same manner.

9.1.2 Hamiltonian matrix and FCI reference solution

The Hilbert space of the full problem denoted by $\mathscr{H}^{\mathrm{QED}}$ is a product space between the electronic and the photonic Hilbert spaces. As discussed in the previous section, there is not need for us to use the full electronic Fock space, since all operators that enter $\hat{H}_{\mathrm{e}}$ conserve the number of particles in the system and are therefore block-diagonal. Hence, it is sufficient to consider only the N_{e}-electron Hilbert space $\mathscr{H}_{-}^{(N_{\mathrm{e}})}$. In our implementation this is realized as follows, fermionic operators are first constructed in the full fermionic Fock space according to Eq. (9.2) and then restricted to the N_{e}-particle subspace. We will use the same notation (e.g. $\hat{c}_i^\dagger \hat{c}_j$) for these operators, but hereafter we will always mean the restricted domain $\mathscr{H}_{-}^{(N_{\mathrm{e}})}$ and not the full Fock space, when talking about particle-number conserving fermionic operators.

For photons, on the contrary, we have to keep the full (in practice truncated) Fock space $\mathscr{F}^{\mathrm{p}}$, since the light-matter interaction term in Eq. (8.1) contains the particle-number non-conserving operator $(\hat{a}^\dagger + \hat{a}\ )$.

Hence, the Hilbert space of the full problem is given by

$$\mathscr{H}^{\mathrm{QED}} = \mathscr{H}_{-}^{(N_{\mathrm{e}})} \otimes \mathscr{F}^{\mathrm{p}}, \tag{9.15}$$

Operators are constructed in this joint space as

$$\hat{c}_i^\dagger \hat{c}_j, \qquad \hat{c}_i^\dagger \hat{c}_j^\dagger \hat{c}_l \hat{c}_k, \qquad \ldots \qquad \rightarrow \qquad \hat{c}_i^\dagger \hat{c}_j \otimes \mathbb{1}^{\mathrm{p}}, \qquad \hat{c}_i^\dagger \hat{c}_j^\dagger \hat{c}_l \hat{c}_k \otimes \mathbb{1}^{\mathrm{p}}, \qquad \ldots \tag{9.16}$$

$$\hat{a}\ , \qquad \hat{a}^\dagger \qquad \rightarrow \qquad \mathbb{1}^{\mathrm{e}} \otimes \hat{a}\ , \qquad \mathbb{1}^{\mathrm{e}} \otimes \hat{a}^\dagger, \tag{9.17}$$

where $\mathbb{1}^{\mathrm{e}}$ and $\mathbb{1}^{\mathrm{p}}$ are identity matrices (corresponding to identity operators) on either of the two spaces with corresponding sizes

$$\dim \mathbb{1}^{\mathrm{e}} = \dim \mathscr{H}_{-}^{(N_{\mathrm{e}})} = \binom{2N}{N_{\mathrm{e}}}, \qquad \dim \mathbb{1}^{\mathrm{p}} = \dim \mathscr{F}^{\mathrm{p}} = (n_{\max} + 1). \tag{9.18}$$

With these consideration, we are now able to construct a matrix representation of a coupled electron-photon Hamiltonian given in Eq. (8.1). For a FCI reference solution, the Hamiltonian matrix is diagonalized numerically using the built-in routine from the Python NumPy library [150]. Additionally, other observables of interest can be constructed as matrices on $\mathscr{H}^{\mathrm{QED}}$ in the outlined manner.

9.1.3 Construction of CC equations

The non-linear set of CC amplitude equations given in Eq. (8.12) can be constructed using the individual ingredients introduced so far. We begin with the photonic contribution: matrix representations of photonic excitation operators are built from their matrix representation given in Eq. (9.13) following the same prescription as creation and annihilation operators in Eq. (9.17); the photonic portion of the reference state defined in Eq. (8.7) is the vacuum, whose vector representation is given in Eq. (9.8).

The electronic part of the reference wave function in Eq. (8.7) is given by the HF solution of H_{e}. Therefore, the HF scheme is implemented as described in section 3.1.1 with an additional simplification: we optimize only the spatial parts $|\varphi_i\rangle$ of the HF-spin orbitals $|\psi_i^\sigma\rangle = |\varphi_i\rangle|\sigma\rangle$. The HF Slater determinant is obtained by occupying each of the lowest $N_{\mathrm{e}}/2$ spatial orbitals with two electrons of opposite spin

$$|\Phi_0^{\mathrm{e}}\rangle = |\psi_1^\uparrow \psi_1^\downarrow \cdots \psi_{N_{\mathrm{e}}/2}^\uparrow \psi_{N_{\mathrm{e}}/2}^\downarrow\rangle^-. \tag{9.19}$$

This approximation is known as (closed-shell) restricted HF [5].

HF orbitals are obtained in terms of the original (spatial) basis that we denote by $\{|l\rangle\}$

$$|\varphi_i\rangle = \sum_{l=1}^{N} \langle l|\varphi_i\rangle |l\rangle = \sum_{l=1}^{N} \varphi_i(l)|l\rangle. \tag{9.20}$$

The numbers $\varphi_i(l)$ can be understood as entries of a basis-transformation matrix that rotates the original orbitals into the HF orbitals. This gives us a prescription for creation and annihilation operators of particles in HF orbitals

$$\hat{c}_{i,\sigma} = \sum_{l=1}^{N} \varphi_i(l)\hat{c}_{l,\sigma}, \qquad \hat{c}^\dagger_{i,\sigma} = \sum_{l=1}^{N} \varphi^*_i(l)\hat{c}^\dagger_{l,\sigma}. \tag{9.21}$$

where $\hat{c}_{l,\sigma}$ and $\hat{c}^\dagger_{l,\sigma}$ are constructed following Eq. (9.2) and Eq. (9.7).

With this, we can now build the fermionic (and therefore also the coupled) reference state

$$|\Phi^{\mathrm{e}}_0\rangle = \sum_{i=1}^{N_{\mathrm{e}}/2} \hat{c}^\dagger_{i\downarrow}\hat{c}^\dagger_{i\uparrow}|0\rangle \tag{9.22}$$

as well as fermionic excitation operators $\hat{\tau}_\mu$, where we have e.g. singles

$$\hat{c}^\dagger_{a,\sigma}\hat{c}_{i,\sigma}, \qquad \text{with } i \in \{1,\dots,N_{\mathrm{e}}/2\},\ a \in \{(N_{\mathrm{e}}/2+1),\dots,N\}, \tag{9.23}$$

and doubles

$$\hat{c}^\dagger_{b,\sigma'}\hat{c}^\dagger_{a,\sigma}\hat{c}_{i,\sigma}\hat{c}_{j,\sigma'}, \quad \text{with } i \in \{1,\dots,N_{\mathrm{e}}/2\},\ j \in \{i,\dots,N_{\mathrm{e}}/2\},\ a \in \{(N_{\mathrm{e}}/2+1),\dots,N\},\ b \in \{a,\dots,N\}. \tag{9.24}$$

These operators are then transformed into $\mathscr{H}^{\mathrm{QED}}$ as given in Eq. (9.16).

The cluster operator $\hat{T}$ can be constructed following Eq. (8.11) for any given set of amplitudes $\boldsymbol{t}$. With the set of all considered excited references $\langle\Phi_\kappa| = \left(\hat{\tau}_\kappa|\Phi_0\rangle\right)^\dagger$, we obtain a vector valued function with entries

$$\Omega_\kappa(\mathbf{t}) = \langle\Phi_\kappa|e^{-\hat{T}(\mathbf{t})}\hat{H}e^{\hat{T}(\mathbf{t})}|\Phi_0\rangle, \tag{9.25}$$

where $\hat{H}$ is the full Hamiltonian matrix that has been built in the course of section 9.1.2. The vector function $\boldsymbol{\Omega}(\mathbf{t})$ becomes zero for the optimal set of CC amplitudes.

9.2 Iterative solution of CC equations

Roots of Eq. (9.25) can be found by employing the multi-dimensional Newton's method. It is an iterative technique where, starting with a close-enough initial guess $\boldsymbol{t}_0$, the vector function for the iteration step n is approximated as [151]

$$\boldsymbol{\Omega}(\mathbf{t}^{(n)} + \Delta\mathbf{t}) \approx \boldsymbol{\Omega}(\mathbf{t}^{(n)}) + \boldsymbol{\Omega}^{(1)}(\mathbf{t}^{(n)})\Delta\mathbf{t}. \tag{9.26}$$

Here, $\boldsymbol{\Omega}^{(1)}(\mathbf{t})$ is the Jacobian matrix, whose entries are given by

$$\Omega^{(1)}_{\kappa\lambda}(\mathbf{t}) = \frac{\partial}{\partial t_\lambda}\langle\Phi_\kappa|e^{-\hat{T}(\mathbf{t})}\hat{H}e^{\hat{T}(\mathbf{t})}|\Phi_0\rangle = \langle\Phi_\kappa|e^{-\hat{T}(\mathbf{t})}\left[\hat{H},\hat{\tau}_\lambda\right]e^{\hat{T}(\mathbf{t})}|\Phi_0\rangle. \tag{9.27}$$

By solving

$$\boldsymbol{\Omega}(\mathbf{t}^{(n)} + \Delta\mathbf{t}) \stackrel{!}{=} \mathbf{0} \qquad \Rightarrow \qquad \boldsymbol{\Omega}^{(1)}(\mathbf{t}^{(n)})\Delta\mathbf{t} = -\boldsymbol{\Omega}^{(0)}(\mathbf{t}^{(n)}), \tag{9.28}$$

we obtain a new estimate for the root of $\mathbf{\Omega}(\mathbf{t})$ as

$$\mathbf{t}^{(n+1)} = \mathbf{t}^{(n)} + \Delta\mathbf{t}. \tag{9.29}$$

and the procedure is repeated until the required accuracy is reached.

To avoid the need of solving Eq. (9.28) at each step, the Jacobian in Eq. (9.27) is often approximated by its diagonal contribution [151]

$$\Omega^{(1)}_{\kappa\lambda}(\mathbf{t}) = \Delta\epsilon_\kappa \delta_{\kappa\lambda}, \tag{9.30}$$

where

$$\begin{aligned}\Omega^{(1)}_{\kappa\kappa}(\mathbf{t}) &= \langle\Phi_\kappa|e^{-\hat{T}(\mathbf{t})}\left[\hat{H},\hat{\tau}_\kappa\right]e^{\hat{T}(\mathbf{t})}|\Phi_0\rangle = \langle\Phi_\kappa|\bar{H}(\mathbf{t})\hat{\tau}_\kappa|\Phi_0\rangle - \langle\Phi_\kappa|\hat{\tau}_\kappa\bar{H}(\mathbf{t})|\Phi_0\rangle \\ &= \underbrace{\langle\Phi_\kappa|\bar{H}(\mathbf{t})|\Phi_\kappa\rangle}_{E_\kappa(\mathbf{t})} - \underbrace{\langle\Phi_0|\bar{H}(\mathbf{t})|\Phi_0\rangle}_{E_0(\mathbf{t})} \equiv \Delta E_\kappa(\mathbf{t}) \approx \Delta\epsilon_\kappa.\end{aligned} \tag{9.31}$$

Here, for all $\mathbf{t}$, we approximate the energy difference ΔE_κ by the following mean-field estimates

$$\Delta\epsilon_\kappa = \begin{cases} \varepsilon_a - \varepsilon_i, & \text{if } \hat{\tau}_\kappa = \hat{c}^\dagger_{a,\sigma}\hat{c}_{i,\sigma}\,, \\ \varepsilon_a + \varepsilon_b - \varepsilon_i - \varepsilon_j, & \text{if } \hat{\tau}_\kappa = \hat{c}^\dagger_{b,\sigma'}\hat{c}^\dagger_{a,\sigma}\hat{c}_{i,\sigma}\hat{c}_{j,\sigma'}\,, \\ n\cdot\omega_c, & \text{if } \hat{\tau}_\kappa = |n\rangle\langle 0|, \\ \varepsilon_a - \varepsilon_i + n\cdot\omega_c, & \text{if } \hat{\tau}_\kappa = \hat{c}^\dagger_{a,\sigma}\hat{c}_{i,\sigma}\otimes|n\rangle\langle 0|, \\ \varepsilon_a + \varepsilon_b - \varepsilon_i - \varepsilon_j + n\cdot\omega_c, & \text{if } \hat{\tau}_\kappa = \hat{c}^\dagger_{b,\sigma'}\hat{c}^\dagger_{a,\sigma}\hat{c}_{i,\sigma}\hat{c}_{j,\sigma}\otimes|n\rangle\langle 0|, \end{cases} \tag{9.32}$$

where $\varepsilon_{i,j}$ are one-particle HF energies (see Eq. (3.2)) of occupied HF orbitals, $\varepsilon_{a,b}$ are energies of empty HF orbitals, into which the electrons are excited, and ω_c is the photon energy.

This approximation of the Jacobian significantly simplifies Eq. (9.28), which now for every individual amplitude reads

$$\Delta t_\kappa = -\frac{\Omega^{(0)}_\kappa(\mathbf{t}^{(n)})}{\epsilon_\kappa}. \tag{9.33}$$

The resulting approach is called *quasi-Newton method.* It performs well, when the mean-field spectrum is close enough to the targeted solution.

9.3 Correction method for close-lying excited states in CC theory

After the ground-state CC equations have been solved, the excited-state properties of a system can be calculated by employing the EOM-CC method introduced in the last part of section 3.1.3. Since we have constructed the full Hamiltonian matrix, performing EOM-CC boils down to diagonalizing the ST Hamiltonian that is projected onto a subspace spanned by the reference state and all considered excited references. Therefore, the matrix elements of the ST Hamiltonian are given by

$$\bar{H}_{\kappa\lambda} = \langle\Phi_\kappa|e^{-\hat{T}}\hat{H}e^{\hat{T}}|\Phi_\lambda\rangle, \qquad \bar{H}_{0\lambda} = \langle\Phi_0|e^{-\hat{T}}\hat{H}e^{\hat{T}}|\Phi_\lambda\rangle, \qquad \bar{H}_{\kappa 0} = 0. \tag{9.34}$$

As seen in the above equations, $\bar{H}$ is not symmetric and EOM-CC is therefore a non-hermitian theory. This is not a problem, when the full space $\mathscr{H}^{\mathrm{QED}}$ is considered. In this case, $\bar{H}$ would have exactly the *same* eigenvalues (even though different eigenstates) as the original Hamiltonian $\hat{H}$. Polynomial scaling of the theory, however, comes with the price of considering only a subset of states in $\mathscr{H}^{\mathrm{QED}}$. There, non-hermicity of $\bar{H}$ often leads to difficulties for energetically close eigenstates. This is a well-known problem in standard CC theory [152, 153], that often

occurs at conical intersections of excited BO potential energy surfaces in molecules. There, the different surfaces cross e.g. when inter-atomic distances are varied. In our case, we will observe such intersections by modifying the cavity frequency.

In the following, we analyze these issues following Köhn and Tajti [152] and introduce a correction scheme, which is also based on [152]. Eigenvalues E_κ of the similarity-transformed Hamiltonian $\bar{H}$ are associated with a set of left ($\langle\widetilde{\Psi}_\kappa|$) and right eigenvectors ($|\Psi_\kappa\rangle$) that fulfill the bi-orthogonality condition (see Eqs. (3.28)-(3.30))

$$\langle\widetilde{\Psi}_\kappa|\Psi_\lambda\rangle = \delta_{\kappa\lambda}. \tag{9.35}$$

The right eigenvectors are conventionally normalized, but generally non-orthgonal. The elements of the corresponding metric matrix $\mathbf{S}$ are $S_{\kappa\lambda} = \langle\Psi_\kappa|\Psi_\lambda\rangle$, so we have $S_{\kappa\kappa} = 1$ and $S_{\kappa\lambda} \neq 0$ with $\kappa \neq \lambda$. The left and right eigenvectors are related via

$$|\widetilde{\Psi}_\kappa\rangle = \sum_\lambda |\Psi_\lambda\rangle \left[\boldsymbol{S}^{-1}\right]_{\lambda\kappa} . \tag{9.36}$$

This metric matrix is directly related to the asymmetry of $\bar{H}$. To quantify this relation, let us consider the matrix form of $\bar{H}$ in a subspace of two close-lying eigenstates

$$\bar{H}|\Psi_1\rangle = E_1|\Psi_1\rangle, \qquad \bar{H}|\Psi_2\rangle = E_2|\Psi_2\rangle \tag{9.37}$$

and additionally shift it by their mean energy $(E_1 + E_2)/2$. The eigenstates are gauged such that their overlap $S = \langle\Psi_1|\Psi_2\rangle$ becomes real, which is achieved by applying the following gauge-transformation

$$|\Psi_2\rangle \to e^{i\theta}|\Psi_2\rangle, \qquad \theta = \arctan\left(\frac{\mathrm{Im}\, S}{\mathrm{Re}\, S}\right). \tag{9.38}$$

The matrix $\bar{H}$ can be transformed such that it takes the following asymmetric form[1]

$$\bar{H} = \begin{pmatrix} -\Delta & X+Y \\ X-Y & \Delta \end{pmatrix}. \tag{9.39}$$

We call Y the antisymmetric coupling. Eigenvalues of $\bar{H}$ are given by

$$\Lambda_\pm = \pm\frac{E_2 - E_1}{2} = \pm\sqrt{\Delta^2 + X^2 - Y^2}. \tag{9.40}$$

Now, the following scenarios are possible:

- $Y^2 < \Delta^2 + X^2$, meaning that we have distinct real eigenvalues $\Lambda_\pm$;
- $Y^2 = \Delta^2 + X^2$, meaning that the eigenvalue splitting vanishes;
- $Y^2 > \Delta^2 + X^2$, meaning that we have imaginary eigenvalues.

The last scenario is unphysical and has to be compensated for. Now, the value of Y can be related to the overlap S as follows [152]

$$|Y| = \widetilde{S}\sqrt{\Delta^2 + X^2} = \begin{cases} |S|\sqrt{\Delta^2 + X^2}, & \text{if } \Lambda \text{ real} \\ \frac{1}{|S|}\sqrt{\Delta^2 + X^2}, & \text{if } \Lambda \text{ imaginary.} \end{cases} \tag{9.41}$$

Here, we introduced the non-normalized overlap $\widetilde{S}$, whose behavior reflects the transition between real and imaginary regimes for the splitting Λ.

[1] The corresponding new basis is called *crude diabatic basis* in literature [152].

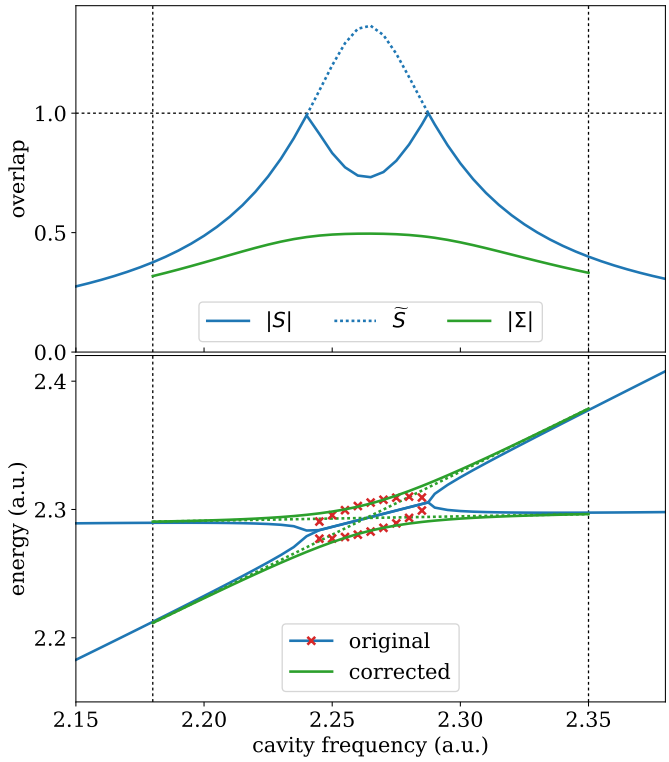

Figure 21. Visualization of the correction method for close-lying excited states. The upper plot shows the original overlap of the states S (solid blue line), the non-normalized overlap $\widetilde{S}$ (dotted blue line) and the new overlap Σ (solid green line). As opposed to the original values, Σ is both, smooth and does not exceed a given threshold of $\Sigma_{\max} = 0.5$. The lower plot shows the corresponding original and corrected energies. If applicable, the imaginary part of a value is depicted as an offset from the real part (red crosses). The corrected energies are real and, even though they build a narrow avoided crossing, they approximate the true conical intersection (dotted green line) well enough. The exemplary system is described by the Hamiltonian given in Eq. (10.1), with parameters: $t_0 = 0.5$, $U = 1.0$, $d = [-1.5, -0.5, 0.5, 1.5]$, $n_{\max} = 4$. The level of truncation is CC-SD-S-0.

In Fig. 21, we plot the overlaps $|S|$ and $\widetilde{S}$ (upper plot) as well as the corresponding energies (lower plot) as functions of the cavity frequency for an exemplary system (parameters are given in the caption of Fig. 21). We observe an increase in both overlaps as the energies get closer until, at point of energetic degeneracy, $S = \widetilde{S} = 1$ is reached. After that, around the point of the true conical intersection, the energies come in pairs of complex numbers that are complex conjugates of each other (imaginary Λ). The non-normalized overlap $\widetilde{S}$ takes on values larger then one in this region, while S decreases again since it is bounded from above by construction.

Now, the idea behind the correction method employed in this thesis is to rotate the close-lying eigenstates within their subspace such that their non-normalized overlap does not exceed a certain threshold value, such that the implications described above become less pronounced. The eigenvalues are also corrected according to the new overlap.

For the two right eigenstates of interest $|\Psi_1\rangle$, $|\Psi_2\rangle$, we write the metric matrix as

$$\boldsymbol{S} = \begin{pmatrix} \langle\Psi_1|\Psi_1\rangle & \langle\Psi_1|\Psi_2\rangle \\ \langle\Psi_2|\Psi_1\rangle & \langle\Psi_2|\Psi_2\rangle \end{pmatrix} = \begin{pmatrix} 1 & S \\ S & 1 \end{pmatrix} = \begin{pmatrix} 1 & \cos\varphi \\ \cos\varphi & 1 \end{pmatrix}, \tag{9.42}$$

where φ is the enclosed angle between the two states.

The states $|\Psi_1\rangle$ and $|\Psi_2\rangle$ can be othogonalized by multiplying them with

$$\boldsymbol{S}^{-1/2} = \frac{1}{2|\sin\varphi|} \begin{pmatrix} \sqrt{1-\cos\varphi} + \sqrt{1+\cos\varphi} & -\sqrt{1-\cos\varphi} + \sqrt{1+\cos\varphi} \\ -\sqrt{1-\cos\varphi} + \sqrt{1+\cos\varphi} & \sqrt{1-\cos\varphi} + \sqrt{1+\cos\varphi} \end{pmatrix}. \tag{9.43}$$

We then choose a new smaller overlap Σ (with the corresponding new angle $\vartheta = \arccos\Sigma$), which is defined as a function of the old overlap $\widetilde{S}$. We further impose the condition that it has to mirror the behavior of $\widetilde{S}$ and be bounded from below by 0 and from above by a maximum value $\Sigma_{\max}$. The specific form of the function is not that important and we take the functional form used in [152]

$$\Sigma = \text{sign}(S) \cdot \Sigma_{\max} \cdot \tanh\left(\widetilde{S}/\Sigma_{\max}\right) \tag{9.44}$$

The new overlap Σ is also plotted in Fig 21 for a chosen region and it shows the required behavior.

The orthogonalized eigenstates are then rotated again, this time to have the new overlap $\Sigma = \cos\vartheta$. The corresponding rotation matrix reads

$$\mathbf{\Sigma}^{1/2} = \frac{1}{2|\sin\vartheta|}\begin{pmatrix} \sqrt{1-\cos\vartheta}+\sqrt{1+\cos\vartheta} & \sqrt{1-\cos\vartheta}-\sqrt{1+\cos\vartheta} \\ \sqrt{1-\cos\vartheta}-\sqrt{1+\cos\vartheta} & \sqrt{1-\cos\vartheta}+\sqrt{1+\cos\vartheta} \end{pmatrix}. \tag{9.45}$$

Hence, the modified eigenstates are obtained via

$$\begin{pmatrix} |\Psi_1\rangle \\ |\Psi_2\rangle \end{pmatrix}_{\text{corr}} = \mathbf{\Sigma}^{1/2}\boldsymbol{S}^{-1/2}\begin{pmatrix} |\Psi_1\rangle \\ |\Psi_2\rangle \end{pmatrix}. \tag{9.46}$$

Additionally, the vectors $|\Psi_1\rangle, |\Psi_2\rangle$ have to be normalized and the left eigenvectors have to be transformed accordingly such that Eq. (9.35) holds.

Energy eigenvalues also have to be adapted with respect to the new overlap. Using the relation between eigenvalue splitting Λ and the antisymmetric coupling Y Eq. (9.40) as well as the relation between Y and the overlap, we obtain

$$\Lambda_{\text{corr}} = \pm\Lambda\frac{\sqrt{1-\Sigma^2}}{\sqrt{1-\widetilde{S}^2}}. \tag{9.47}$$

The corrected eigenvalues are then given by

$$E_{1,\text{corr}} = E_1 + \Lambda - \Lambda_{\text{corr}}, \qquad E_{2,\text{corr}} = E_2 - \Lambda + \Lambda_{\text{corr}}. \tag{9.48}$$

They are plotted in the lower part of Fig 21. We observe that the corrected values build an avoided crossing with a small splitting. This behavior is not ideal, but, since we are for now not particularly interested in describing conical intersections in cavity QED, but rather in stability of the overall method, this result is good enough, especially since we know that describing conical intersections correctly is a notorious issue in CC theory [152, 153].

Numerically, problems not only occur for complex values of Λ but also for $S \to 1$. In these cases, the norm of the corresponding left eigenvectors diverges and for $S = 1$ the inverse of $\mathbf{S}$ simply does not exist, as the right vectors $|\Psi_i\rangle$ do not span the full space anymore. Therefore we will apply the correction methods in cases where Λ and S fall under a certain threshold value. In Fig. 21, this region is determined by $S > 0.3$.

10 Application

In this chapter we benchmark the developed polaritonic CC theory against FCI for a suitable model system. The model system is introduced in section 10.1 and a set of observables that we use to characterize it is discussed in section 10.2. In section 10.3, we then discuss some of the exact properties of the model system. Finally, we show results calculated with polaritonic CC theory, compare them to their FCI analogs and discuss the quality of the method in section 10.4.

10.1 Few-sites Hubbard model in a quantum cavity

In order to test the eligibility of our approach, we choose a model systems, which on the one hand is simple enough to be treated with FCI and on the other hand is large enough such that the CC approach is indeed an approximation. In the purely electronic case, CCSD is exact for two particles and we hence want to choose a model with a richer electronic structure than the two-level and two-electron models that are often used as a benchmark in quantum optics and QED chemistry [36]. This is covered by the following model that has been discussed in the community [154]. For the matter part we choose a one-dimensional Hubbard model with four sites, four electrons and zero-boundary conditions. It is a simple model for correlated electrons, where the kinetic energy is given by nearest-neighbor hopping with amplitude t_0 and the electron-electron interaction is mimicked by an on-site repulsion of strength U. Additionally, a dipole moment $\vec{d}$ is assigned to the chain of electrons, which then couples to one cavity mode with frequency ω_c. The model is visualized in Fig. 22. The dipole operator is given by $\hat{d} = \sum_\sigma \sum_{i=1}^{4} d_i \hat{c}^\dagger_{i,\sigma} \hat{c}_{i,\sigma}$ and the corresponding Hamiltonian reads

$$\hat{H} = -t_0 \sum_\sigma \sum_{i=1}^{3} \left(\hat{c}^\dagger_{i+1,\sigma} \hat{c}_{i,\sigma} + \hat{c}^\dagger_{i,\sigma} \hat{c}_{i+1,\sigma} \right) + U \sum_{i=1}^{4} \hat{c}^\dagger_{i\uparrow} \hat{c}^\dagger_{i\downarrow} \hat{c}_{i\downarrow} \hat{c}_{i\uparrow} + \omega_c \hat{a}^\dagger \hat{a} \; - \gamma \omega_c \hat{d} \left(\hat{a} + \hat{a}^\dagger \right) + \gamma^2 \omega_c \hat{d}^2. \tag{10.1}$$

In the following, we consider three different regimes for the light-matter coupling strength – *weak*, *strong* and *ultra-strong* – with corresponding values for γ. The characterization of different regimes can vary depending on the underlying experiment or the theoretical model. We briefly discuss our choice of parameters below and refer the interested reader comprehensive discussions in literature [34, 155].

In cavity QED, the coupling is usually considered to be strong, when the prefactor $\gamma\omega_c$ in Eq. (10.1) is large compared to losses in the cavity. In this case, the losses are so small that the molecule (or any other emitter) can absorb and emit cavity photons before they are radiated into the environment. These interaction processes are called Rabi oscillations. The resulting excited-state spectrum of the coupled system differs significantly from the one of the bare molecule. Formation of hybrid light-matter states, *polaritons*, is characteristic for this regime. Since cavity losses are not explicitly included into our model, we use energy gaps between polaritonic states, their (Rabi) splittings, as measure for the coupling strength. The system is considered to be in the strong-coupling regime, when the Rabi splitting takes the value

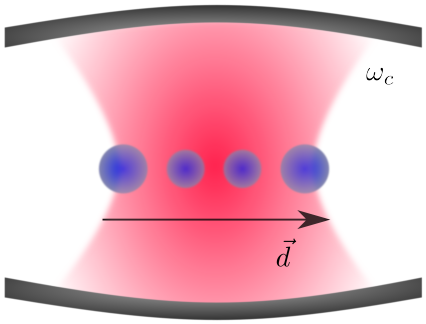

Figure 22. A four-site Hubbard chain in half-filling serving as a model molecule. The molecule has a dipole moment $\vec{d}$, which is strongly coupled to the cavity mode with frequency ω_c. Figure published in [147].

of a non-negligible fraction of the underlying bare excitation and is therefore clearly visible. As we show in section 10.3, $\gamma = 0.07$ is a reasonable choice for the strong-coupling regime. The weak-coupling regime is represented by $\gamma = 0.01$.

Following [34], we consider systems with $\gamma = 0.2$ to be in the ultra-strong coupling regime. This regime is mainly characterized by a breakdown of the rotating-wave approximation, which is widely used in quantum optics [156], which e.g. results in a modification of the system's ground-state. The impact of the cavity on the molecular ground-state for weaker couplings is, on the contrary, rather small [45, 157, 158].

10.2 Observables

In the course of this chapter, we discuss the following properties of our model system:

- **Energy spectrum $E_\kappa = \omega_\kappa$[1]:** This is the first target for every wave-function method. We also obtain the corresponding eigenstates $|\Psi_\kappa\rangle$, from which additional observables are calculated. In the following, we use the index κ for electron-photon states and the index k for purely electronic states ($\in \mathscr{H}_-^{(N_e)}$).

- **Mode occupation $\langle \hat{n}_p \rangle$:** This observable

$$\langle \hat{n}_p \rangle = \langle \Psi_\kappa | \hat{a}^\dagger \hat{a} | \Psi_\kappa \rangle \tag{10.2}$$

  provides a simple and intuitive measure of the photonic contribution to the coupled light-matter state.

- **Purity of subsystem's RDMs Γ_κ:** It is a simple measure for correlation between the electronic and the photonic subsystem [45]. Estimating light-matter correlation on the FCI level will help us understand how good a single-reference method, such as CC theory, can perform in these situations.

  The purity of a subsystem's RDM is defined as

$$\Gamma_\kappa = \mathrm{Tr}\left[\hat{\rho}_e^2\right] = \mathrm{Tr}\left[\left(\mathrm{Tr}_p |\Psi_\kappa\rangle\langle\Psi_\kappa|\right)^2\right], \tag{10.3a}$$

$$= \mathrm{Tr}\left[\hat{\rho}_p^2\right] = \mathrm{Tr}\left[\left(\mathrm{Tr}_e |\Psi_\kappa\rangle\langle\Psi_\kappa|\right)^2\right]. \tag{10.3b}$$

[1] Quick reminder that we use atomic units, where $\hbar = 1$.

Per construction, it is equal for the electronic and the photonic subsystem and we use Eq. (10.3a) in our calculation. The purity is equal to 1 for a pure state, which is a product state between an electronic and a photonic state and it is equals to 0.5 if the underlying state is an equally weighted superposition of two product states.

- **Absorption cross section $\sigma(\omega)$:** This observable provides an excellent way to monitor changes in the system caused by strong light-matter coupling in a way that can be also directly accessed experimentally, as it is trivially related to the ground-state absorption spectrum of the system [32, 159]. The absorption cross section describes the response of the system to an external perturbation in form of a probe light field with frequency ω via

$$\sigma(\omega) = 4\pi\frac{\omega}{c}\mathrm{Im}\left[\sum_k \frac{\left|\langle\Psi_\kappa|\hat{d}|\Psi_0\rangle\right|^2}{(\omega_\kappa-\omega_0)-\omega-i\eta}\right]. \tag{10.4}$$

Here η is a small broadening parameter that accounts for the finite lifetime of excited states.

10.3 Preliminary FCI studies of the model system

Structure of optical spectra and convergence with photon-number cut-off

Here, we discuss the absorption cross-section of the coupled system for a cavity in resonance to the first optically active electronic transition ($\omega_c = \omega_k - \omega_0^e$ and $|\langle\Psi_k|\hat{d}|\Psi_0\rangle| > 0$) and examine its convergence with the photon-number cut-off $n_{\max}$.

The cross sections are plotted in Fig. 23 for weak, strong and ultra-strong coupling to the cavity as well as for the bare molecule (upper plot). The splitting of the first absorption peak into two polaritonic peaks can be observed for strong and ultra-strong coupling, whereas in the weak coupling case it cannot be clearly resolved. This Rabi splitting becomes more pronounced with increasing coupling strength. Moreover we see additional peaks in all coupled spectra compared to the bare spectrum, whose height differs significantly between weak coupling regime (very small) on the one hand and strong and ultra-strong coupling regimes (same order of magnitude as the bare peaks) on the other hand. Off resonance, these lines can be understood as replica of bare electronic states resulting from additional photons in the system. Not only the size, but also the amount of additional peaks varies significantly between the different regimes. While, in the strong-coupling case we still can recognize the original bare spectrum, it is not possible in ultra-strong coupling, since there many states with different photon numbers are involved.

A spectrum is considered as converged with the photon-number cut-off as soon as it does not change anymore for growing $n_{\max}$. From Fig. 23, we obtain the following values: $n_{\max} = 1$ for weak, $n_{\max} = 4$ for strong, and $n_{\max} = 7$ for ultra-strong coupling. These cut-offs are used in all remaining calculations in this chapter.

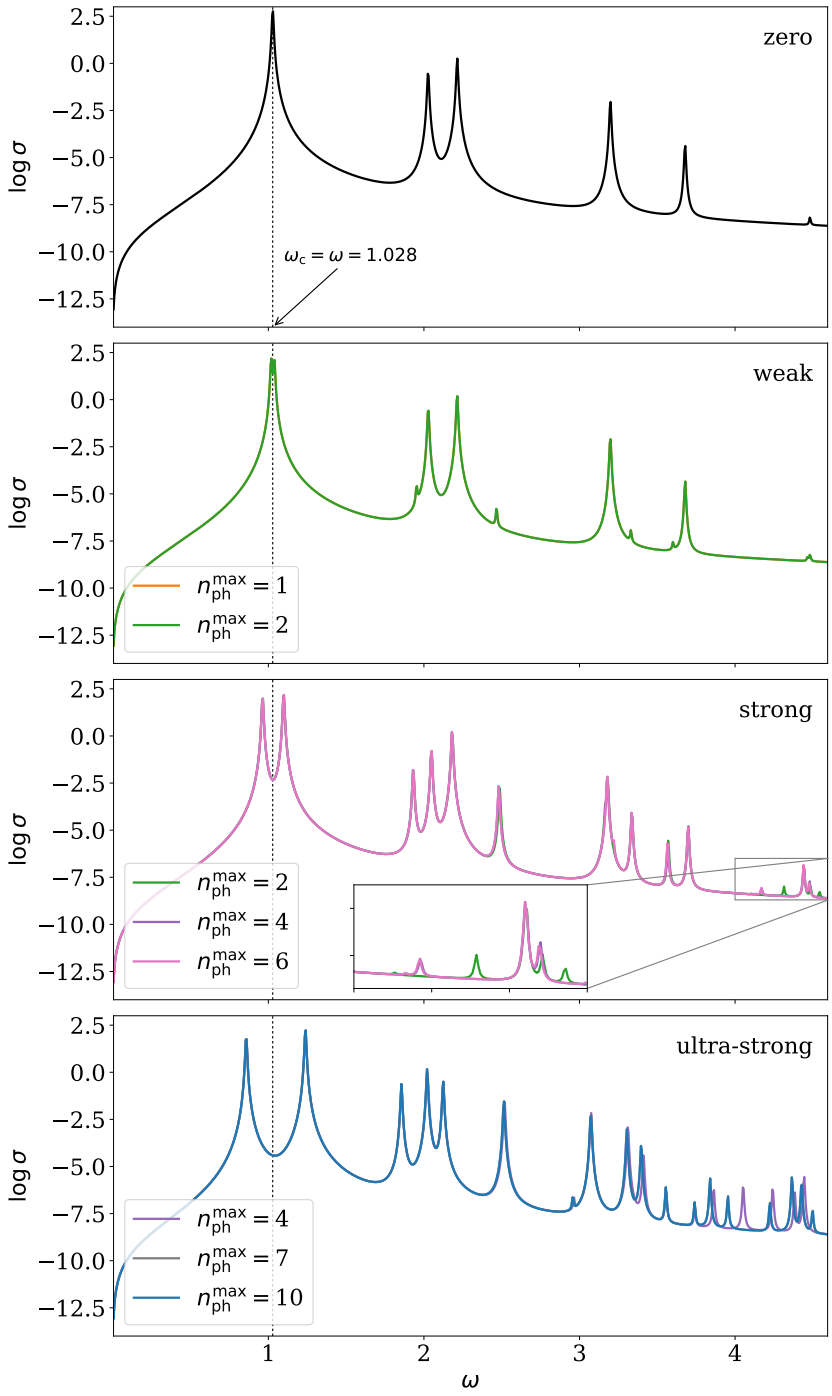

Figure 23. Absorption cross section $\sigma(\omega)$ (logarithmic scale) of the bare 4-site Hubbard chain and of the same system coupled to a cavity in weak ($\gamma = 0.01$), strong ($\gamma = 0.07$) and ultra-strong ($\gamma = 0.2$) coupling regimes for different photon-number cut-offs. The cavity is resonant to the first absorption peak of the bare electronic system. A Rabi splitting of the first peak occurs for strong and ultra-strong coupling. The spectra converge for $n_{\max} = 1$ (weak), $n_{\max} = 4$ (strong) and $n_{\max} = 7$ (ultra-strong) coupling. The following parameters have been used: $\omega_c = 1.028$, $t_0 = 0.5$, $U = 1.0$, $d = [-1.5, -0.5, 0.5, 1.5]$, $\eta = 0.005$.

Polaritonic-state properties

Here, we briefly discuss properties of the polaritionic states that are formed due to strong light-matter interaction. In Fig. 24, we plot energy, mode occupation and purity for the states involved in the Rabi splitting discussed above: ground state $|\Psi_0\rangle$ and the first two optically active

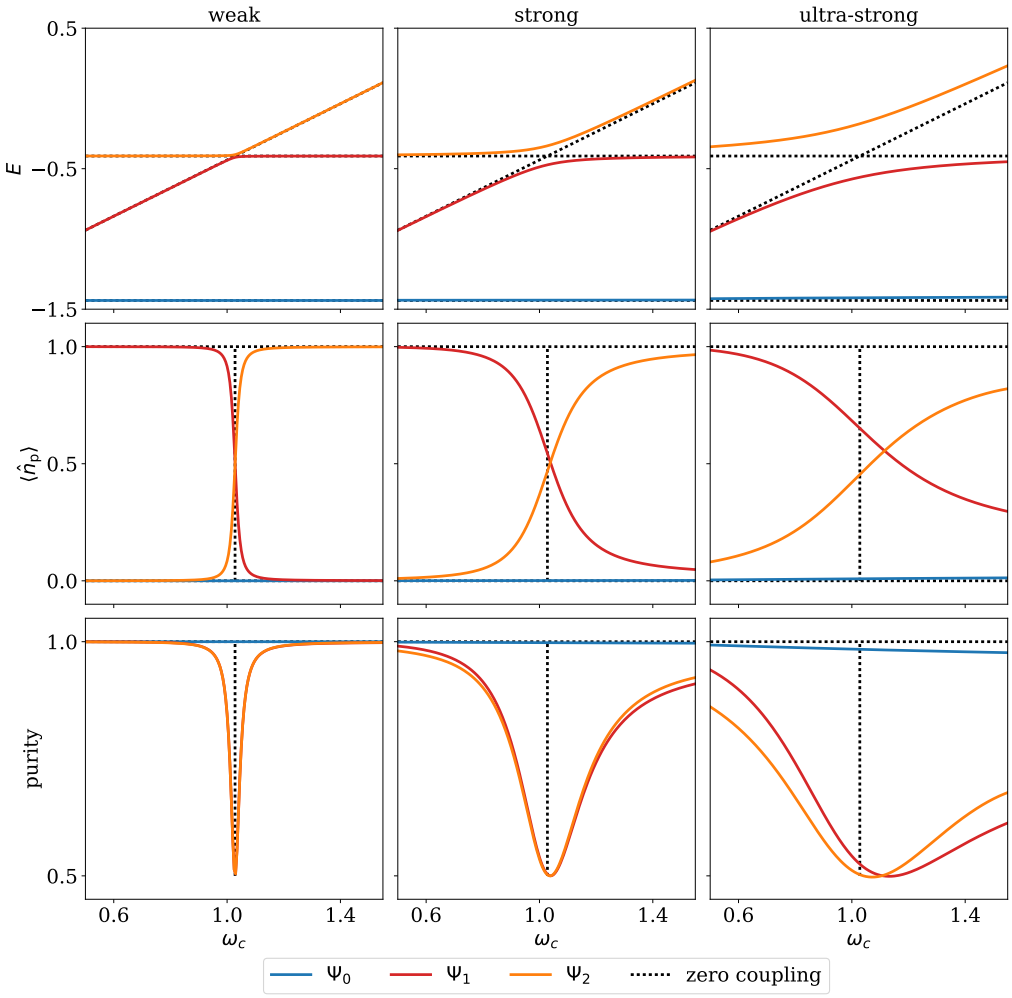

Figure 24. Energy, mode occupation and purity of the ground state $|\Psi_0\rangle$ (blue) and the first two optically active excited states $|\Psi_1\rangle$ (red) and $|\Psi_2\rangle$ (orange) of the coupled light-matter system in weak ($\gamma = 0.01$), strong ($\gamma = 0.07$) and ultra-strong ($\gamma = 0.2$) coupling are plotted as functions of the cavity frequency ω_c. Properties of bare molecular ground and first excited states, as well as of bare molecular ground state plus one cavity photon (black dotted lines) are shown as references. At the crossing of the later two, the considered molecular transition is in resonance with the cavity. The state $|\Psi_1\rangle$ (red) asymptotically corresponds to the bare molecular ground state with one photon for small cavity frequencies and to the bare molecular first excited state and photonic vacuum for large cavity frequencies; to $|\Psi_2\rangle$ (orange) the opposite applies. Avoided crossings of $|\Psi_1\rangle$ and $|\Psi_1\rangle$ appear around resonance and these signatures of polaritonic state formation become more pronounced with growing coupling strength. We further observe an increase in correlation between light and matter subsystems as the combined system enters the ultra-strong coupling regime.

excited states $|\Psi_1\rangle$ and $|\Psi_2\rangle$ of the coupled system. These properties are plotted as functions of cavity frequency ω_c around resonance. Additionally, corresponding bare properties – molecular ground state, molecular first excited state, and molecular ground state with an additional cavity photon – are shown.

In the week coupling case (left panel), properties closely mirror those of the uncoupled case. At resonance $|\Psi_1\rangle$ and $|\Psi_2\rangle$ become nearly degenerate, which results in a narrow dip in purities and an almost step-like behavior of mode occupations.

For strong coupling case (middle panel), hybridization of the excited states becomes much more pronounced and we observe an avoided crossing in energy. The step-like shape of mode occupation curves for excited states is softened significantly. As already in the weak coupling

case, they cross at $\langle \hat{n}_\mathrm{p} \rangle = 0.5$. Their zero- and one-photon character, however, is not restored as quickly as before. A similar behavior can be observed for the purity: excited states of the coupled systems do not exhibit a product-state character ($\Gamma \approx 1$) in most parts of the considered region. The described behavior clearly shows that hybrid light-matter states are formed in the strong-coupling regime.

The formation of the two polaritonic states can also be monitored in case of ultra-strong coupling (right panel). Additionally, we observe a clear signature of this regime: modification of the molecular ground state. This effect is most pronounced in decreasing purity of the state. Moreover, as opposed to the strong-coupling regime, the purity curves of the excited states do not (almost) coincide, which signalizes the fact that in this regime more than just two states hybridize to form a new light-matter state.

When considering changes in the ground state, we perceive that not even ultra-strong light-matter interaction leads to strong correlation between the electronic and the photonic subsystem, which means that CC theory should be successfully applicable to such situations[2]. Correlated excited states can be successfully described with EOM-CC theory [66] and this should not change when photons are included in the theory.

10.4 CC results for the model system

10.4.1 Ground state properties

The polaritonic CC results for the ground-state energy E_0 and photonic mode occupation $\langle \hat{n}_\mathrm{p} \rangle$ in the system are summarized in Table 1 for the different coupling regimes. We show results for the following levels of truncation: CC-SD-S-0, CC-SD-S-D, CC-SD-S-DT (see section 8.1.3 for definition). Note that, since we have only one photonic mode, the level of photonic excitation is at most singles and all possible photonic excitations are included on this level. The polaritonic CC results are compared to FCI results for the coupled system and to FCI and CCSD results in the limit of vanishing electron-photon coupling, FCI(0) and CCSD(0), respectively.

We observe an increasing impact of the cavity on the ground-state properties of the system for

Table 1. Ground-state energy E_0 and mode occupation $\langle \hat{n}_\mathrm{p} \rangle$ of the four-site Hubbard chain strongly coupled to one cavity mode with selected coupling strengths for different levels of CC theory compared with FCI as well as with FCI and CCSD for no electron-photon coupling (FCI(0) and CCSD(0)). We observe excellent agreement of CC results with FCI. By including more excitations in the CC description the ground-state energy is improved. Further, purely photonic observables like mode occupation become accessible. The following parameters have been used: $\omega_c = 1.028$, $t_0 = 0.5$, $U = 1.0$, $d = [-1.5, -0.5, 0.5, 1.5]$, $n_\mathrm{max} = 1$ (weak) $n_\mathrm{max} = 4$ (strong) and $n_\mathrm{max} = 7$ (ultra-strong).

	weak coupling $\gamma = 0.01$		strong coupling $\gamma = 0.07$		ultra-strong coupling $\gamma = 0.2$	
	E_0	$\langle \hat{n}_\mathrm{p} \rangle$	E_0	$\langle \hat{n}_\mathrm{p} \rangle$	E_0	$\langle \hat{n}_\mathrm{p} \rangle$
FCI(0)	−1.43797	—	−1.43797	—	−1.43797	—
CCSD(0)	−1.43801	—	−1.43801	—	−1.43801	—
CC-SD-S-0	−1.43791	0	−1.43335	0	−1.40227	0
CC-SD-S-D	−1.43795	$2.14 \cdot 10^{-5}$	−1.43551	$1.04 \cdot 10^{-3}$	−1.41745	$7.75 \cdot 10^{-3}$
CC-SD-S-DT	−1.43796	$2.24 \cdot 10^{-5}$	−1.43561	$1.09 \cdot 10^{-3}$	−1.41873	$8.57 \cdot 10^{-3}$
FCI	−1.43792	$2.27 \cdot 10^{-5}$	−1.43557	$1.11 \cdot 10^{-3}$	−1.41864	$8.69 \cdot 10^{-3}$

[2] This is different for purely electronic systems, where strong electron-electron interactions usually causes strongly correlated ground states, for which CC does not provide good results.

growing coupling strengths. For instance, the gap between CC-SD-S-0 and CCSD(0) energies widens due to increasing importance of the dipole self-interaction term. The photon-mode occupation, which is now accessible with CC theory, however, is zero for CC-SD-S-0 for all coupling strength, which shows the intrinsic mean-field character of the CC-SD-S-0 approximation. The photon-mode occupation is captured well as soon as coupled excitation are included, namely with CC-SD-S-D and CC-SD-S-DT approximations.

Also for the energy, we observe a very good agreement between CC and FCI results for all coupling strength, when coupled excitations are included in the description. This agreement improves when higher excitations are taken into account and is best for CC-SD-S-DT as was to be expected. However, here we encounter one of the main drawbacks of the CC approach – its non-variational character. In most cases shown in Table 1, the ground-state energy is predicted too low with CC theory.

However, as already discussed in section 10.3, the impact of the cavity on ground-state properties of the system is rather small not only for weak, but also for strong light-matter coupling. A considerable effect is observed only in the ultra-strong coupling regime, which is captured well with CC theories that include coupled excitations. The power of CC theory therefore also lies in the treatment of excited states.

10.4.2 Absorption spectra

We begin our discussion with the case of weak coupling ($\gamma = 0.01$) between light and matter. The corresponding absorption cross sections are plotted as functions of cavity frequency ω_c (x-axis) and frequency ω of the incoming light field (y-axis) in Fig. 25. For reference, the panels at either end show the bare matter FCI spectrum (left) and the full coupled light-matter FCI spectrum (right). In between we show the results of EOM-CC calculations with various levels of truncation of the cluster operator.

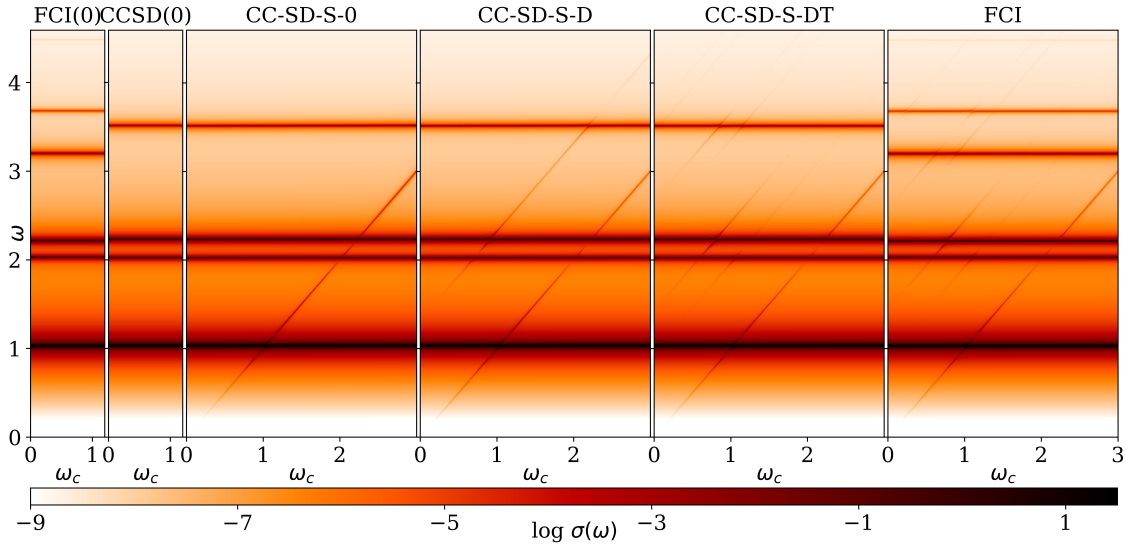

Figure 25. Ground-state absorption cross section $\sigma(\omega)$ of the half-filled four-site Hubbard chain in a cavity as a function of cavity frequency ω_c in the weak-coupling regime $\gamma = 0.01$ for different levels of CC theory compared with FCI results (right-hand side) and zero-coupling limit (FCI(0), left-hand side). We observe the usual non-dispersive matter absorption lines and additionally some low-intensity linear dispersive branches for one-photon processes. No multi-photon processes or significant Rabi splittings occur, meaning that treating the photon field pertubatively would be sufficient in this regime of light-matter coupling. Parameters: $t_0 = 0.5$, $U = 1.0$, $d = [-1.5, -0.5, 0.5, 1.5]$, $n_{\max} = 1$, $\eta = 0.005$. The figure is published in [147].

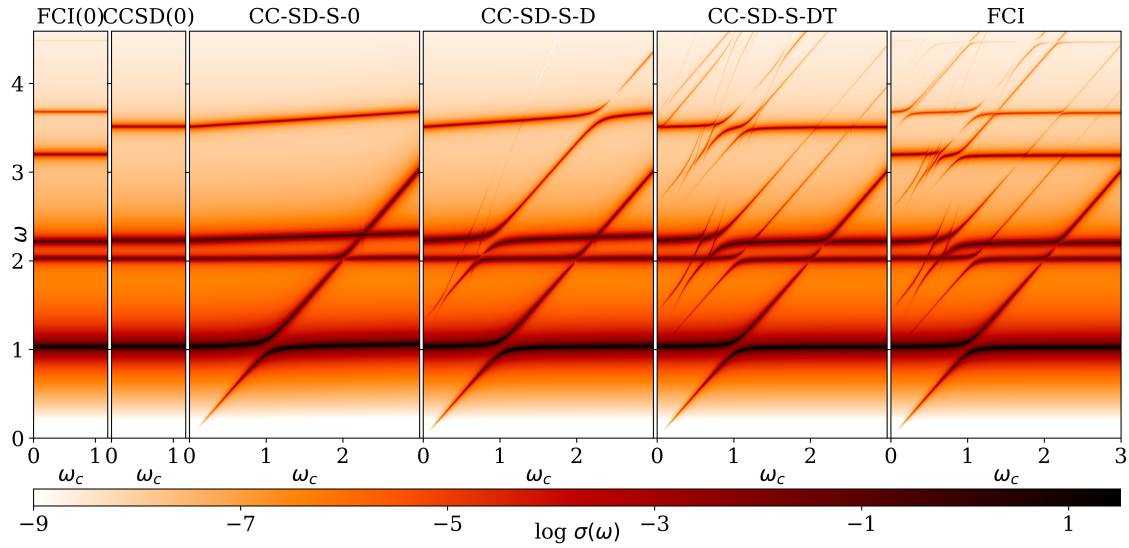

Figure 26. Ground-state absorption cross section $\sigma(\omega)$ of the half-filled four-site Hubbard chain in a cavity as a function of cavity frequency ω_c in the strong-coupling regime $\gamma = 0.07$ for different levels of CC theory compared with FCI results (right-hand side) and zero-coupling limit (FCI(0), left-hand side). We clearly observe the formation of polaritons in various regions of the spectrum, which is accurately captured with CC theory. Parameters: $t_0 = 0.5$, $U = 1.0$, $d = [-1.5, -0.5, 0.5, 1.5]$, $n_{\max} = 4$, $\eta = 0.005$. The figure is published in [147].

The bare electronic spectra (FCI(0) and CCSD(0)) feature horizontal non-dispersive absorption lines; as expected, approximate EOM-CC accurately reproduces low-energy features in the bare spectrum. When coupled to a cavity, the spectrum includes matter absorption lines and additional linear dispersive branches for one-photon processes (lines where $\omega = \omega_c$). The intensity of these one-photon lines is very weak and avoided crossings cannot (or almost cannot) be resolved. While overestimated in CC-SD-S-0, the intensity of the lowest one-photon line is captured well in CC-SD-S-D and CC-SD-S-DT. And, while completely missing in CC-SD-S-0, higher lying photon lines appear one after another with increasing amount of incorporated excitations in CC-SD-S-D and CC-SD-S-DT. We observe excellent agreement for CC-SD-S-DT and remaining deviations from FCI are largely caused by the truncation of the electronic part of the cluster operator.

We continue with the case of strong light-matter coupling of $\gamma = 0.07$. Here, we again can identify molecular absorption lines, although here (in CC-SD-S-0 and CC-SD-S-D) we observe a slight dispersion of these lines, which is caused by the dipole self-interaction. This dispersion, however, is compensated in the more accurate calculations (CC-SD-S-DT and FCI). Further, we observe linear-dispersing photon lines, whose intensity is now of the same order of magnitude as the molecular lines. Additionally to one-photon branches, we can identify many-photon processes with two and three photons, $\omega = 2\omega_c$ and $\omega = 3\omega_c$, respectively. In regions where molecular excitations are resonant with the cavity mode, we observe the famous strong-coupling behavior – signature Rabi splitting of the absorption lines due to formation of polaritons. These features can be clearly seen in various regions of the FCI spectrum, and are well captured by the EOM-CC approximation that includes coupled excitations. We observe that CC-SD-S-DT does a much better job than CC-SD-S-D in capturing the high-energy details of the spectrum. Those parts that are missing in CC-SD-S-D can be attributed to cavity-induced replica of those bare electronic states that include doubly excited determinants to a significant extent. The systematic improvement in the CC treatment as the cluster operator is extended is therefore evident, and remaining deviations from FCI are, as already in the weak-coupling case, largely caused by the truncation of the electronic part of the cluster operator.

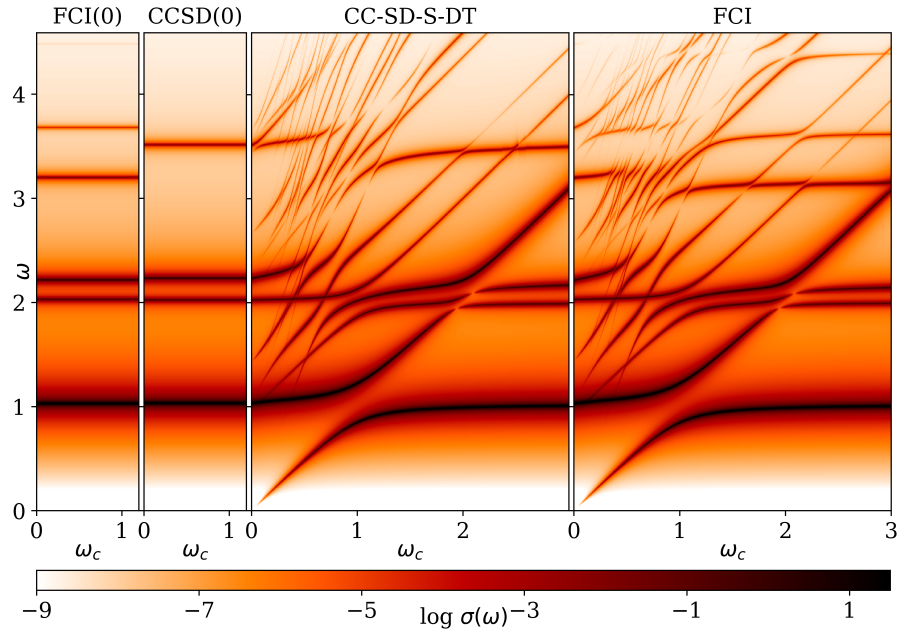

Figure 27. Ground-state absorption cross section $\sigma(\omega)$ of the half-filled four-site Hubbard chain in a cavity as a function of cavity frequency ω_c in the ultra-strong-coupling regime $\gamma = 0.2$ for different levels of CC theory compared with FCI results (right-hand side) and zero-coupling limit (FCI(0), left-hand side). Parameters: $t_0 = 0.5$, $U = 1.0$, $d = [-1.5, -0.5, 0.5, 1.5]$, $n_{\max} = 7$, $\eta = 0.005$. The figure is published in [147].

In Fig. 27 we plot absorption spectra for the remaining ultra-strong coupling case. Here, we omit the CC-SD-S-0 and CC-SD-S-D approximations, since we have discussed their performance already for the other coupling regimes and learned that they miss parts of the spectrum. The exact (FCI) spectrum in the ultra-strong case exhibits a very complicated structure. Additional features appear beyond the simple combination of non-dispersive matter lines and linear dispersive photon lines with Rabi splittings. These include induced transparencies in regions of crossings of various absorption lines with the lowest one-photon line, and complicated structures in the high energy part of the spectrum where many multi-photon processes overlap in the spectrum. The CC-SD-S-DT calculation captures much of this complex structure, with remaining deviations again mainly caused by the truncation of the electronic cluster operator. The low-energy part of the spectrum is reproduced extremely accurately, including the induced transparencies. The qualitative features of the high-energy part of the spectrum are also captured.

11 Summary and outlook

In this part of the thesis, we have extended the framework of CC theory to coupled electron-photon systems thus providing a promising tool for high-accuracy *ab initio* calculations in cavity QED. To this end, we introduced an extended set of excitation operators including novel fermionized photonic operators that enable a rather straightforward extension of the theory.

For the four-site Hubbard model coupled to a quantum cavity, we have shown that signatures of strong and even ultra-strong light-matter interactions such as modifications in the molecular ground-state, formation of polaritons, or multi-photon absorption can be captured very accurately in the framework of polaritonic CC theory.

Although this work has focused on model systems, extension to real *ab initio* Hamiltonians is straightforward, since the method itself does not depend on particular one- and two-electron integrals entering the electronic Hamiltonian. We have also shown that, if the bare molecule is suitable for standard CC theory, it is reasonable to assume that CC will perform excellent for the same system put in a cavity.

In this work we have built the CC equations using the full Hilbert space of the problem, a framework that comes with exponential scaling with the system size. However, we argued that polaritonic CC equations are equivalent to a subset of the conventional CCSDT equations and the theory, at least in the single mode case, scales roughly the same as the $\mathcal{O}(N^6)$ scaling of conventional CCSD theory. Therefore, affordable polynomial scaling implementations of polaritonic CC theory are feasible in the very near future, as they will very closely mirror standard electronic CC codes.

Possible improvements of the theory include employment of alternative CC approaches for excited states, such as CC linear response theory [67], which ensure size-extensivity of the full theory. Additionally, for a more accurate description of appearing conical intersections, another recently introduced method [153] can be utilized.

Furthermore, the formalism developed here can be extended to CC theories for coupling of electrons to polarization modes, phonons or thermal reservoirs, including coupling to multiple boson modes and boson-boson interactions. With the aforementioned extension, wavefunction based *ab-initio* treatment of correlated electron-nuclear-photon systems becomes feasible, paving the way for high-accuracy modeling and interpretation of experiments in these regimes.

Part IV:

Conclusion

12 Conclusion and prospects

On the way towards predictive modeling of quantum effects in nature, we have developed two promising methods in the course of this thesis.

The first challenge that we have addressed is posed by limitations of standard energy-functional approximations in DFT, such as its struggle with strong static correlations or the lack of a direct access to observables other than the energy. These issues of the otherwise very successful method are so notorious that they require radically new strategies in functional development [13]. In part II of the thesis, we have met this claim by proposing our new self-consistent density-functional embedding (SDE) approach. The fundamental novelty of this method is that it leaves behind the necessity of an energy functional by approximating directly the density-potential mapping in Kohn-Sham DFT. To this end, a formally exact self-consistent embedding algorithm, based on the density-matrix embedding theory, has been proposed such that the full system is approximately described by a set of interacting wave functions. The method benefits from the accuracy of wave-function approaches and from rigorous relations in DFT, allowing for an accurate construction of the density and the Kohn-Sham potential of the full system. Moreover, the fragment wave functions provide a direct access to any other observable of the full system. The method has been benchmarked for notoriously difficult situations of molecular bond-stretching in 1D and 2D model systems, showing excellent quantitative agreement with the numerically exact reference calculations. Furthermore, SDE seems to overcome the intrinsic systematic-improvability issue of standard DFT by displaying accuracy that scales with the fragment size. Therefore, we have demonstrated that the SDE approach indeed provides a new pathway for functional development.

Even though the method has been formulated in a general way, its application to more realistic systems requires additional developments. The methodologically rather straightforward extensions will include the substitute of the simple exact-diagonalization scheme employed in the algorithm by more advanced wave-function methods [71, 140–142] and the replacement of the analytic density-inversion scheme by a numeric one [109–113]. The resulting accuracy and numerical stability of such an implementation has to be balanced with the computational cost and this will become one major challenge for the future development. One promising route for an advancement of the method is given by the development of novel projectors for the embedded fragments. Especially those based on the density or the one-body reduced density matrix of the global system rather then the Kohn-Sham Slater determinant would benefit from the formally exact framework of DFT or RDMFT, respectively.

From a more fundamental perspective, we can identify another intriguing range of applications for the SDE approach. The exact KS potential is only known for systems with one or two electrons, which makes benchmarking of approximate methods beyond the two-electron case difficult. Moreover, we obviously cannot know whether there are any additional features present in the exact functional that we are missing so far due to the outlined limitations. We can imagine that SDE will close this gap by providing, if not exact, still very accurate Kohn-Sham potentials for systems with more than two electrons.

We believe that density-functional embedding strategies can provide a promising route for advances in extended density-functional theories, such as current-DFT [160] or quantum elec-

trodynamical DFT (QEDFT)[35–37, 161, 162], which do not have a wide range of approximate functionals at their disposal. The latter extends the scope of DFT to cavity QED applications by including photons into the theory. DMET, which has inspired our density-functional embedding scheme, has recently been extended to fermion-boson systems [92] and we therefore believe that similar paths can be taken for a density-functional embedding approach to QEDFT.

QEDFT is of particular importance as it is one of the few approaches that aims at describing molecular systems strongly coupled to quantized light from first principles. The broad interest in describing such coupled molecular-photon systems beyond simplified effective models is driven by the tremendous experimental progress in the field, which demonstrated e.g. that formation of polaritons can substantially change chemical and physical properties of molecular systems [25–28]. These groundbreaking insight show great promise for future quantum technologies.

In this spirit, we have developed polaritonic CC theory in part III of this thesis, a wave-function approach to cavity QED that combines accuracy with computational feasibility. The method extends standard CC theory, which is one of the most accurate methods in conventional quantum chemistry, to coupled electron-photon problems by introducing novel excitation operators for the coupled light-matter system. For molecular models in optical cavities we have demonstrated that our CC approach is able to accurately reproduce all key features present in the exact reference absorption spectra. These include not only Rabi-splittings of absorption peaks but also multi-photon processes that, to the best of our knowledge, other *ab initio* methods so far fail to describe.

The next step for polaritonic CC theory is to achieve the claimed polynomial scaling in practice. Due to the proposed fermion-like incorporation of photons into the theory, we do not expect any major difficulties for its efficient implementation, since the underlying equations are basically those of standard CCSDT theory. Quite the opposite, the new polaritonic CC theory will benefit from the progress standard CC theory made over the last decades [15, 163]. Therefore, we believe that the method will become a high-accuracy computational tool in QED chemistry in the very near future, providing very accurate predictions for properties of small to intermediate size molecules in cavity experiments. Therefore, polaritonic CC theory will also serve as a benchmark for other computational methods that are being developed in the field of polaritonic chemistry, just like CCSD(T) in conventional quantum chemistry.

The developed CC formalism is not limited in its application only to electron-photon systems and can be extended to other coupled fermion-boson setups, such as electron-phonon and the subsequent electron-phonon-photon problems. Addressing the later is necessary for understanding intriguing phenomena that have been observed in regimes of vibrational strong coupling [27, 30], since in these regimes the BO approximation breaks down [36, 39] and molecular motion has to be considered explicitly in terms of phonons.

On a larger scale, polaritonic CC can be combined with embedding approaches to enable first-principle calculations of large systems, such as molecular ensembles, interacting strongly with cavity modes [164, 165].

Appendix

A

A.1 Technical details of our SDE implementation

Here, we will discuss technical details of our implementation of the self-consistent density embedding algorithm that we have developed in part II of the thesis. Some of the parts are valid for the special case of two electrons and some are more general. We will address the points as they appear in the algorithm in Fig. 9.

A.1.1 Indexing and partitioning in 2D systems

We begin by addressing the 2D Hamiltonian in Eq. (6.11), which is quite impractical in this form. In practice, we assign one index k to each pair (i_x, i_y). In this way, we map the 2D system onto an effective 1D system, which has some long-range hopping depending on how the index is assigned. There is no unique way of mapping a double index (i_x, i_y) onto a single index k, and also no optimal way of doing it, since we are going to partition the system into different fragments.

We choose a particular index mapping, which we show in Fig. 28 exemplary for an 8×8-grid with fragments of size 4×4. To each site we therefore assign an index $k \in \{1, \ldots, 64\}$, where the mapping follows the partition into the first set of patches.

Further, instead of only the middle site, which is not possible to define here, we keep the inner square of 2×2 sites for the description of the global properties. We still consider this partition

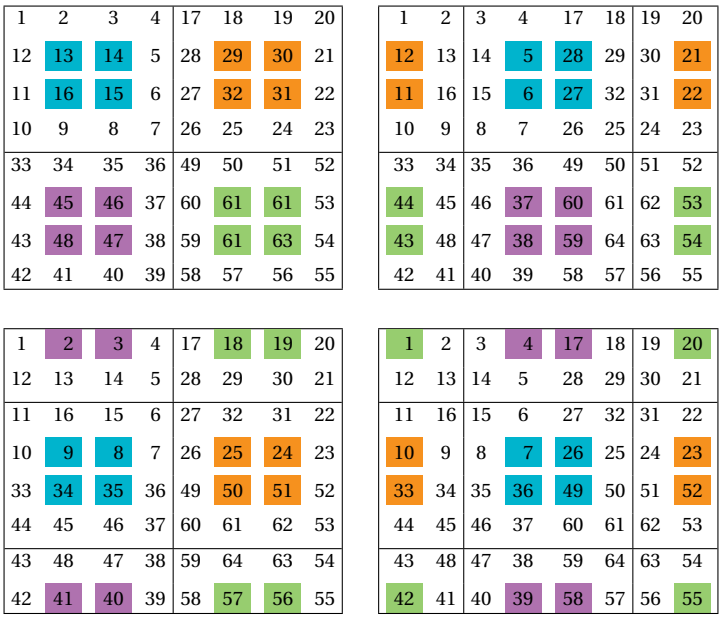

Figure 28. Visualization of our 2D-to-1D mapping and patching for a 8×8-grid with $N_{\text{frag}} = 4 \times 4$. There are in total 16 fragments that have to be considered in order to describe the full system. The middle 2×2 parts of each fragment that are used to put together the full system are marked with different colors.

as continuous (see section 5.2.1). This type of partition results in having 16 fragments, all of which are depicted in Fig. 28.

A.1.2 Exact diagonalization for two electrons

As introduced in section 3.3.2, for each fragment we obtain an embedding Hamiltonian of the form (see Eq. (3.69))

$$\hat{H}_{\text{emb}} = \hat{h}_{\text{emb}} + \hat{W}_{\text{emb}} = \sum_{a,b=1}^{2N_{\text{frag}}} \sum_{\sigma} h^{\text{emb}}_{ab} \hat{c}^{\dagger}_{a\sigma} \hat{c}_{b\sigma} + \frac{1}{2} \sum_{i,j,k,l=1}^{2N_{\text{frag}}} \sum_{\sigma,\sigma'} W^{\text{emb}}_{abcd} \hat{c}^{\dagger}_{a\sigma} \hat{c}^{\dagger}_{b\sigma'} \hat{c}_{d\sigma'} \hat{c}_{c\sigma} \,, \tag{A.1}$$

by employing the corresponding single-particle projection. Here, we have omitted the index i for simplicity.

For the two-electron case that we consider here, we represent this Hamiltonian as a matrix in the two-particle Hilbert space $\mathscr{H}^{(2)}$, which does not include particle-exchange symmetry explicitly (see Eq. (2.19) and the subsequent discussion). We can further decompose $\mathscr{H}^{(2)}$ into a spatial and a spin part

$$\mathscr{H}^{(2)} = \mathscr{H}^{(2)}_{\text{space}} \otimes \begin{pmatrix} |\text{singlet}\rangle & 0 \\ 0 & |\text{triplet}\rangle \end{pmatrix}, \tag{A.2}$$

where possible spin states are given by

$$|\text{singlet}\rangle = \frac{1}{\sqrt{2}} \left(|\uparrow\downarrow\rangle - |\downarrow\uparrow\rangle \right), \tag{A.3}$$

$$|\text{triplet}\rangle \in \left\{ |\uparrow\uparrow\rangle; \, |\downarrow\downarrow\rangle; \, \frac{1}{\sqrt{2}} \left(|\uparrow\downarrow\rangle + |\downarrow\uparrow\rangle \right) \right\}. \tag{A.4}$$

The space $\mathscr{H}^{(2)}_{\text{space}}$ is spanned by products of spatial CAS orbitals

$$\Phi_{ab}(r_1, r_2) = \varphi^{\text{CAS}}_a(r_1) \varphi^{\text{CAS}}_b(r_2). \tag{A.5}$$

The one-body part of the Hamiltonian matrix in $\mathscr{H}^{(2)}_{\text{space}}$ is given by

$$h^{(2)}_{\text{emb}} = h^{\text{emb}} \otimes \mathbb{1}_{2N_{\text{frag}} \times 2N_{\text{frag}}} + \mathbb{1}_{2N_{\text{frag}} \times 2N_{\text{frag}}} \otimes h^{\text{emb}} \tag{A.6}$$

with matrix elements of h^{emb} defined in Eq. (3.70).

The construction of the two-body matrix results from the following reformulation of the interaction tensor

$$W^{\text{emb}}_{abcd} \hat{c}^{\dagger}_{a\sigma} \hat{c}^{\dagger}_{b\sigma'} \hat{c}_{d\sigma'} \hat{c}_{c\sigma} = \left(W^{\text{emb}}_{ac} \hat{c}^{\dagger}_{a\sigma} \hat{c}_{c\sigma} \right) \cdot \left(W^{\text{emb}}_{bd} \hat{c}^{\dagger}_{b\sigma'} \hat{c}_{d\sigma'} \right). \tag{A.7}$$

The introduced decomposition of tensor elements W^{emb}_{abcd} into matrix products $W_{ac} \cdot W_{bd}$ is based on symmetry properties of the interaction tensor [5]. The corresponding part of the Hamiltonian matrix on $\mathscr{H}^{(2)}_{\text{space}}$ is constructed from these matrices similar to the one-body part in Eq. (A.6), namely

$$W^{(2)}_{\text{emb}} = W^{\text{emb}} \otimes W^{\text{emb}} + W^{\text{emb}} \otimes W^{\text{emb}} = 2W \otimes W. \tag{A.8}$$

In practice, the matrix $W^{(2)}_{\text{emb}}$ is built via a simple reshape of the interaction tensor W^{emb}, which we illustrate for the simplest case of $N_{\text{frag}} = 1$

$$W^{\text{emb}} = \left\{ \left[\begin{pmatrix} W_{1111} & W_{1112} \\ W_{1121} & W_{1122} \end{pmatrix}, \begin{pmatrix} W_{1211} & W_{1212} \\ W_{1221} & W_{1222} \end{pmatrix} \right], \left[\begin{pmatrix} W_{2111} & W_{2112} \\ W_{2121} & W_{2122} \end{pmatrix}, \begin{pmatrix} W_{2211} & W_{2212} \\ W_{2221} & W_{2222} \end{pmatrix} \right] \right\} \tag{A.9}$$

$$\rightarrow W^{(2)}_{\text{emb}} = 2 \begin{pmatrix} W_{1111} & W_{1112} & W_{1211} & W_{1212} \\ W_{1121} & W_{1122} & W_{1221} & W_{1222} \\ W_{1211} & W_{1212} & W_{2111} & W_{2112} \\ W_{1221} & W_{1222} & W_{2221} & W_{2222} \end{pmatrix}. \tag{A.10}$$

The full Hamiltonian on $\mathscr{H}^{(2)}_{\text{space}}$ is then given by the matrix

$$H^{(2)}_{\text{emb}} = h^{(2)}_{\text{emb}} + \frac{1}{2} W^{(2)}_{\text{emb}}, \tag{A.11}$$

which can be diagonalized by a built-in routine from the Python NumPy library [150].

The eigenvectors of $H^{(2)}_{\text{emb}}$ are either symmetric ($\Psi(r_1, r_2) = \Psi(r_2, r_1)$)) or anti-symmetric ($\Psi(r_1, r_2) = -\Psi(r_2, r_1)$). The former belong to spin-singlet states and the later to spin-triplets. The ground state of $H^{(2)}_{\text{emb}}$ is always a singlet state and therefore has a symmetric spatial part $\Psi(r_1, r_2)$.

The corresponding ground-state 1RDM and 2RDM are calculated as

$$\gamma^{\text{emb}}_{ab} = \sum_k 2\Psi^*_{ak}\Psi_{kb}, \qquad \Gamma^{\text{emb}}_{abcd} = 2\Psi^*_{da}\Psi_{bc}, \tag{A.12}$$

with $\Psi_{ab} = \Psi(r_{1_a}, r_{2_b}) = \Psi(r_{1_b}, r_{2_a}) = \Psi_{ba}$. These embedding density matrices can then be used to calculate observables as given in Eq. (5.5). Note that, since with two electrons in the system we do not have any occupied core orbitals, all full-system properties in Eqs. (5.5)-(5.7) such as the wave-function $|\Psi\rangle^i$ can be replaced by the embedding properties ($|\Psi_{\text{emb}}\rangle^i$ in this example).

A.1.3 Exact inversion for two electrons

One reason for choosing a problem that only includes two electrons is that for this example we can analytically invert the density n of the interacting problem to yield the potential $v_{\text{S}}[n]$ of the auxiliary non-interacting system that has the same density. Here, we follow the derivation in [119], but generalize the real-space equations to more general set of orbitals, in our case the CAS orbitals. This can be done, since there is a one-to-one correspondence between density and potential for general quantum lattice systems [166].

We formulate the KS equations on our CAS as (see Eq. (3.38) for their real-space version)

$$\left(\hat{h}_{\text{emb}} + \hat{v}_{\text{emb,Hxc}}\right) \varphi^{\text{KS}}_j = \varepsilon_j \varphi^{\text{KS}}_j, \tag{A.13}$$

where all operators and orbitals φ^{KS}_j are expressed in terms of CAS orbitals $\varphi^{\text{CAS}}_a(x_i)$. Here, the external potential is absorbed in $\hat{h}_{\text{emb}}$ and we therefore have $\hat{v}_{\text{emb,Hxc}}$ instead of $\hat{v}_{\text{emb,KS}}$ in the equation.

Since the ground-state of a two-electron problem is always a singlet-state, the ground-state density of the system is obtained by taking into account only the lowest KS orbital

$$n^{\text{CAS}} = 2\left|\varphi^{\text{KS}}_0\right|^2. \tag{A.14}$$

By assuming a real-valued ground state orbital, which can always be met, and inserting n^{KS} into Eq. (A.13) we obtain

$$\hat{v}_{\text{Hxc}}[n] = \frac{\hat{h}_{\text{emb}}\sqrt{n^{\text{CAS}}}}{\sqrt{n^{\text{CAS}}}} + \varepsilon_0. \tag{A.15}$$

A.1.4 Optimization of the chemical potential

For the optimization of the chemical potential that we introduced in section 5.2.3 and, more specifically, in Eq. (5.9) we use the secant method, which is a simple robust root-finding algorithm. The root x_0 of a function f is approximated through the following recurrence relation

$$x_0^{(n+1)} = x_0^{(n)} - f\left(x_0^{(n)}\right) \frac{x_0^{(n)} - x_0^{(n-1)}}{f\left(x_0^{(n)}\right) - f\left(x_0^{(n-1)}\right)}. \tag{A.16}$$

It requires two initial values $x^{(0)}$ and $x^{(1)}$ and in our code these values are $x_0^{(0)} = 0$ and $x_0^{(1)} = \langle \hat{N}_\mathrm{e} \rangle - N_\mathrm{e}$.

We do not optimize the chemical potential at every step of the algorithm, since it would involve unnecessary high numerical cost. The optimization is performed once in the beginning of the cycle, more precisely in the second iteration step, to ensure at least a roughly correct particle number for the whole procedure and then at each iteration step k *after* the difference of the Hxc potentials

$$\Delta v_\mathrm{KS}^{(k)} = \sum_i \left| v_\mathrm{KS}^{(k)}(x_i) - v_\mathrm{KS}^{(k-1)}(x_i) \right| \cdot \Delta x < \xi_\mu \tag{A.17}$$

falls below a certain threshold ξ_μ, meaning after a certain precision has been achieved in the self-consistence cycle. In our implementation, this threshold value is chosen as $\xi_\mu = 10^{-4}$.

A.1.5 Potential update

In section 5.2.4, we have established the connection between the set of local KS potentials and the global KS potential. In this section, we briefly specify some additional implementational details for the potential update in the SDE self-consistency cycle.

Initial value

Every self-consistency cycle requires an initial value. Here, we choose the simplest initial potential $v_\mathrm{KS} = v_\mathrm{ext}$ or equivalently $v_\mathrm{Hxc} = 0$. This means that our initial guess does not include any correlations or interactions.

Potential gauge

All potentials have a certain gauge freedom, meaning that they are defined up to a constant. Same holds for v_Hxc. This means that, in order to obtain a self-consistent solution, we need to fix the gauge at every step. In our algorithm, we choose the gauge such that v_Hxc vanishes at the left boundary $v_\mathrm{Hxc}(x_1) \stackrel{!}{=} 0$.

Potential mixing

As in standard DFT [167], we include a potential mixing into our self-consistency cycle in order to stabilize the algorithm. The update for the Hxc potential is constructed as

$$\tilde{v}_\mathrm{Hxc}^{(k)} = \eta\, v_\mathrm{Hxc}^{(k)} + (1-\eta)\, \tilde{v}_\mathrm{Hxc}^{(k-1)}, \tag{A.18}$$

where $v_\mathrm{Hxc}^{(k)}$ is the potential that is built from local potentials of the fragments after the kth iteration. In our implementation $\eta = 0.9$ is chosen.

Acronyms

1RDM	one-body Reduced Density Matrix
2RDM	two-body Reduced Density Matrix
BCH	Baker-Campbell-Hausdorff
BO	Born-Oppenheimer
CAS	Complete Active Space
CC	Coupled Cluster
CCD	Coupled Cluster Doubles
CCSD	Coupled Cluster Singles Doubles
CCSD(T)	Coupled Cluster Singles Doubles perturbative Triples
CCSDT	Coupled Cluster Singles Doubles Triples
CC-SD-S-0	Coupled Cluster - electronic Singles Doubles - photonic Singles
CC-SD-S-D	Coupled Cluster - electronic Singles Doubles - photonic Singles - coupled Doubles
CC-SD-S-DT	Coupled Cluster - electronic Singles Doubles - photonic Singles - coupled Doubles Triples
CI	Configuration Interaction
CID	Configuration Interaction Doubles
CISD	Configuration Interaction Singles Doubles
DFT	Density Functional Theory
DMET	Density-Matrix Embedding Theory
DMFT	Dynamical Mean-Field Theory
ED	Exact Diagonalization
EOM-CC	Equation-Of-Motion Coupled-Cluster
FCI	Full Configuration Interaction
GGA	General Gradient Approximation
HF	Hartree-Fock
HK	Hohenberg-Kohn

Hxc	Hartree exchange-correlation
KS	Kohn-Sham
LDA	Local Density Approximation
QED	Quantum Electrodynamics
QEDFT	Quantum Electrodynamical Density Functional Theory
RDMFT	Reduced Density-Matrix Functional Theory
RPA	Random Phase Approximation
SCF	Self-Consistent Field
ST	Similarity Transformed
SVD	Singular Value Decomposition
xc	exchange-correlation

Bibliography

[1] P. A. M. Dirac, *Quantum mechanics of many-electron systems*, Proc. R. Soc. Lond. A **123**, 714 (1929).

[2] E. Schrödinger, *Quantisierung als Eigenwertproblem*, Ann. Phys. **384**, 361 (1926).

[3] W. Heitler and F. London, *Wechselwirkung neutraler Atome und homöopolare Bindung nach der Quantenmechanik*, Z. Phys. **44**, 455 (1927).

[4] J. A. Pople, *Nobel lecture: Quantum chemical models*, Rev. Mod. Phys. **71**, 1267 (1999).

[5] A. Szabo and N. S. Ostlund, *Modern Quantum Chemistry: Introduction to Advanced Electronic Structure Theory*, Courier Corporation (2012), ISBN: 978-0-486-69186-2.

[6] H. Larsen, J. Olsen, P. Jørgensen, and J. Gauss, *Comparison of full-configuration interaction and coupled-cluster harmonic and fundamental frequencies for BH and HF*, Chem. Phys. Lett. **342**, 200 (2001).

[7] H. M. Senn and W. Thiel, *QM/MM methods for biomolecular systems*, Angew. Chem. Int. Ed. **48**, 1198 (2009).

[8] P. Hohenberg and W. Kohn, *Inhomogeneous Electron Gas*, Phys. Rev. **136**, B864 (1964).

[9] W. Kohn and L. J. Sham, *Self-Consistent Equations Including Exchange and Correlation Effects*, Phys. Rev. **140**, A1133 (1965).

[10] J. P. Perdew, K. Burke, and M. Ernzerhof, *Generalized Gradient Approximation Made Simple*, Phys. Rev. Lett. **77**, 3865 (1996).

[11] M. A. Marques, M. J. Oliveira, and T. Burnus, *Libxc: A library of exchange and correlation functionals for density functional theory*, Comput. Phys. Comm. **183**, 2272 (2012).

[12] M. G. Medvedev, I. S. Bushmarinov, J. Sun, J. P. Perdew, and K. A. Lyssenko, *Density functional theory is straying from the path toward the exact functional*, Science **355**, 49 (2017).

[13] A. J. Cohen, P. Mori-Sánchez, and W. Yang, *Challenges for density functional theory*, Chem. Rev. **112**, 289 (2011).

[14] C. D. Sherrill and H. F. Schaefer III, *The configuration interaction method: Advances in highly correlated approaches*, Adv. Quantum Chem. **34**, 143 (1999).

[15] R. J. Bartlett and M. Musiał, *Coupled-cluster theory in quantum chemistry*, Rev. Mod. Phys. **79**, 291 (2007).

[16] U. Schollwoeck, *The density-matrix renormalization group*, Rev. Mod. Phys. **77**, 259 (2005).

[17] A. Georges, G. Kotliar, W. Krauth, and M. J. Rozenberg, *Dynamical mean-field theory of strongly correlated fermion systems and the limit of infinite dimensions*, Rev. Mod. Phys. **68**, 13 (1996).

[18] G. Kotliar, S. Y. Savrasov, K. Haule, V. S. Oudovenko, O. Parcollet, and C. A. Marianetti, *Electronic structure calculations with dynamical mean-field theory*, Rev. Mod. Phys. **78**, 865 (2006).

[19] K. Held, *Electronic structure calculations using dynamical mean field theory*, Adv. Phys. **56**, 829 (2007).

[20] G. Knizia and G. K.-L. Chan, *Density Matrix Embedding: A Simple Alternative to Dynamical Mean-Field Theory*, Phys. Rev. Lett. **109** (2012).

[21] G. Knizia and G. K.-L. Chan, *Density matrix embedding: A strong-coupling quantum embedding theory*, J. Chem. Theory Comput. **9**, 1428 (2013).

[22] S. Wouters, C. A. Jiménez-Hoyos, Q. Sun, and G. K.-L. Chan, *A Practical Guide to Density Matrix Embedding Theory in Quantum Chemistry*, J. Chem. Theory Comput. **12**, 2706 (2016).

[23] T. W. Ebbesen, *Hybrid Light–Matter States in a Molecular and Material Science Perspective*, Acc. Chem. Res. **49**, 2403 (2016).

[24] R. Chikkaraddy, B. De Nijs, F. Benz, S. J. Barrow, O. A. Scherman, E. Rosta, A. Demetriadou, P. Fox, O. Hess, and J. J. Baumberg, *Single-molecule strong coupling at room temperature in plasmonic nanocavities*, Nature **535**, 127 (2016).

[25] S. Kéna-Cohen and S. Forrest, *Room-temperature polariton lasing in an organic single-crystal microcavity*, Nat. Photonics **4**, 371 (2010).

[26] J. A. Hutchison, T. Schwartz, C. Genet, E. Devaux, and T. W. Ebbesen, *Modifying Chemical Landscapes by Coupling to Vacuum Fields*, Angew. Chem. Int. Ed. **51**, 1592 (2012).

[27] D. M. Coles, Y. Yang, Y. Wang, R. T. Grant, R. A. Taylor, S. K. Saikin, A. Aspuru-Guzik, D. G. Lidzey, J. K.-H. Tang, and J. M. Smith, *Strong coupling between chlorosomes of photosynthetic bacteria and a confined optical cavity mode*, Nat. Commun. **5**, 5561 (2014).

[28] M. Sukharev and A. Nitzan, *Optics of exciton-plasmon nanomaterials*, J. Phys. Condens. Matter **29**, 443003 (2017).

[29] A. Thomas, J. George, A. Shalabney, M. Dryzhakov, S. J. Varma, J. Moran, T. Chervy, X. Zhong, E. Devaux, C. Genet, J. A. Hutchison, and T. W. Ebbesen, *Ground-State Chemical Reactivity under Vibrational Coupling to the Vacuum Electromagnetic Field*, Angew. Chem. Int. Ed. **55**, 11462 (2016).

[30] J. Lather, P. Bhatt, A. Thomas, T. W. Ebbesen, and J. George, *Cavity Catalysis by Cooperative Vibrational Strong Coupling of Reactant and Solvent Molecules*, Angew. Chem. Int. Ed. (2019).

[31] K. Stranius, M. Hertzog, and K. Börjesson, *Selective manipulation of electronically excited states through strong light–matter interactions*, Nat. Commun. **9**, 2273 (2018).

[32] M. Ruggenthaler, N. Tancogne-Dejean, J. Flick, H. Appel, and A. Rubio, *From a quantum-electrodynamical light–matter description to novel spectroscopies*, Nat. Rev. Chem. **2**, 0118 (2018).

[33] R. F. Ribeiro, L. A. Martínez-Martínez, M. Du, J. Campos-Gonzalez-Angulo, and J. Yuen-Zhou, *Polariton chemistry: controlling molecular dynamics with optical cavities*, Chem. Sci. **9**, 6325 (2018).

[34] A. F. Kockum, A. Miranowicz, S. De Liberato, S. Savasta, and F. Nori, *Ultrastrong coupling between light and matter*, Nat. Rev. Phys. **1**, 19 (2019).

[35] M. Ruggenthaler, J. Flick, C. Pellegrini, H. Appel, I. V. Tokatly, and A. Rubio, *Quantum-electrodynamical density-functional theory: Bridging quantum optics and electronic-structure theory*, Phys. Rev. A **90**, 012508 (2014).

[36] J. Flick, M. Ruggenthaler, H. Appel, and A. Rubio, *Atoms and molecules in cavities, from weak to strong coupling in quantum-electrodynamics (QED) chemistry*, Proc. Natl. Acad. Sci. USA **114**, 3026 (2017).

[37] J. Flick, D. M. Welakuh, M. Ruggenthaler, H. Appel, and A. Rubio, *Light-matter response functions in quantum-electrodynamical density-functional theory: modifications of spectra and of the maxwell equations*, arXiv:1803.02519 (2018).

[38] J. Flick, H. Appel, M. Ruggenthaler, and A. Rubio, *Cavity Born–Oppenheimer approximation for correlated electron–nuclear-photon systems*, J. Chem. Theory Comput. **13**, 1616 (2017).

[39] J. Galego, F. J. Garcia-Vidal, and J. Feist, *Cavity-Induced Modifications of Molecular Structure in the Strong-Coupling Regime*, Phys. Rev. X **5**, 041022 (2015).

[40] M. Kowalewski, K. Bennett, and S. Mukamel, *Non-adiabatic dynamics of molecules in optical cavities*, J. Chem. Phys. **144**, 054309 (2016).

[41] P. M. M. de Melo and A. Marini, *Unified theory of quantized electrons, phonons, and photons out of equilibrium: A simplified ab initio approach based on the generalized Baym-Kadanoff ansatz*, Phys. Rev. B **93**, 155102 (2016).

[42] O. Vendrell, *Collective Jahn-Teller interactions through light-matter coupling in a cavity*, Phys. Rev. Lett. **121**, 253001 (2018).

[43] D. Karlsson and R. v. Leeuwen, *Non-equilibrium Green's Functions for Coupled Fermion-Boson Systems*, in: *Handbook of Materials Modeling: Methods: Theory and Modeling*, Springer, Cham (2018), ISBN: 978-3-319-42913-7.

[44] J. del Pino, F. A. Y. N. Schröder, A. W. Chin, J. Feist, and F. J. Garcia-Vidal, *Tensor Network Simulation of Non-Markovian Dynamics in Organic Polaritons*, Phys. Rev. Lett. **121**, 227401 (2018).

[45] C. Schäfer, M. Ruggenthaler, H. Appel, and A. Rubio, *Modification of excitation and charge transfer in cavity quantum-electrodynamical chemistry*, Proc. Natl. Acad. Sci. USA **116**, 4883 (2019).

[46] O. Christiansen, *Vibrational coupled cluster theory*, J. Chem. Phys. **120**, 2149 (2004).

[47] W. Nolting, *Grundkurs Theoretische Physik 5/1: Quantenmechanik - Grundlagen*, 6th ed., Springer, Berlin, Heidelberg, (2006), ISBN: 978-3-540-40071-0.

[48] D. Werner, *Funktionalanalysis*, 7th ed., Springer, Berlin, Heidelberg (2011), ISBN: 978-3-642-21016-7.

[49] J. R. Shewell, *On the Formation of Quantum-Mechanical Operators*, Am. J. Phys **27**, 16 (1959).

[50] P. A. M. Dirac, *The principles of quantum mechanics*, 4th ed., Oxford University Press (1981), ISBN: 978-0-19-852011-5.

[51] R. L. Bishop and S. I. Goldberg, *Tensor analysis on manifolds*, Courier Corporation (2012), ISBN: 978-0-486-13923-4.

[52] M. Born and R. Oppenheimer, *Zur Quantentheorie der Molekeln*, Ann. Phys. **389**, 457 (1927).

[53] J. M. Combes, P. Duclos, and R. Seiler, *The Born-Oppenheimer Approximation*, in *Rigorous Atomic and Molecular Physics*, Vol. 74, Springer, Boston, MA (1981), ISBN: 978-1-4613-3350-0.

[54] C. Huang, M. Pavone, and E. A. Carter, *Quantum mechanical embedding theory based on a unique embedding potential*, J. Chem. Phys. **134**, 154110.

[55] Q. Sun and G. K.-L. Chan, *Quantum Embedding Theories*, Acc. Chem. Res. **49**, 2705 (2016).

[56] V. Fock, *„Selfconsistent field" mit Austausch für Natrium*, Z. Phys. **62**, 795 (1930).

[57] D. R. Hartree and W. Hartree, *Self-Consistent Field, with Exchange, for Beryllium*, Proc. R. Soc. Lond. A **150**, 9 (1935).

[58] F. Jensen, *Introduction to computational chemistry*, 2nd ed., John Wiley & Sons, Ltd. (2007), ISBN: 978-0-470-01186-7.

[59] E. Schwegler and M. Challacombe, *Linear scaling computation of the Hartree–Fock exchange matrix*, J. Chem. Phys. **105**, 2726 (1996).

[60] I. Shavitt and R. J. Bartlett, *Many-body methods in chemistry and physics: MBPT and coupled-cluster theory*, Cambridge University Press (2009), ISBN: 978-0-521-81832-2.

[61] T. D. Crawford and H. F. Schaefer III, *An introduction to coupled cluster theory for computational chemists*, Rev. Comput. Chem. **14**, 33 (2000).

[62] H. F. Baker, *Alternants and continuous groups*, Proc. London Math. Soc. **3**, 24 (1905).

[63] J. E. Campbell, *On a Law of Combination of Operators bearing on the Theory of Continuous Transformation Groups*, Proc. London Math. Soc. **28**, 381 (1897).

[64] F. Hausdorff, *Die symbolische Exponentialformel in der Gruppentheorie*, Leipz. Ber. **58**, 19 (1906).

[65] J. F. Stanton and R. J. Bartlett, *The equation of motion coupled-cluster method. A systematic biorthogonal approach to molecular excitation energies, transition probabilities, and excited state properties*, J. Chem. Phys. **98**, 7029 (1993).

[66] A. I. Krylov, *Equation-of-motion coupled-cluster methods for open-shell and electronically excited species: The hitchhiker's guide to Fock space*, Annu. Rev. Phys. Chem. **59**, 433 (2008).

[67] H. Koch, R. Kobayashi, A. Sanchez de Merás, and P. Jørgensen, *Calculation of size-intensive transition moments from the coupled cluster singles and doubles linear response function*, J. Chem. Phys. **100**, 4393 (1994).

[68] C. F. Fischer, *A multi-configuration Hartree-Fock program*, Comput. Phys. Commun. **1**, 151 (1970).

[69] R. J. Buenker and S. D. Peyerimhoff, *Individualized configuration selection in CI calculations with subsequent energy extrapolation*, Theoret. Chim. Acta **35**, 33 (1974).

[70] J. Hubbard, *Electron correlations in narrow energy bands*, Proc. R. Soc. Lond. A **276**, 238 (1963).

[71] G. K.-L. Chan and S. Sharma, *The density matrix renormalization group in quantum chemistry*, Annu. Rev. Phys. Chem **62**, 465 (2011).

[72] C. Fiolhais, F. Nogueira, and M. A. Marques, *A primer in density functional theory*, Vol. 620, Springer, Berlin, Heidelberg (2003), ISBN: 978-3-540-37072-7.

[73] V. L. Lignères and E. A. Carter, *An Introduction to Orbital-Free Density Functional Theory*, in: *Handbook of Materials Modeling: Methods*, Springer, Dordrecht (2005), ISBN: 978-1-4020-3286-8.

[74] J. P. Perdew and K. Schmidt, *Jacob's ladder of density functional approximations for the exchange-correlation energy*, AIP Conf. Proc **577**, 1 (2001).

[75] A. D. Becke, *Density-functional exchange-energy approximation with correct asymptotic behavior*, Phys. Rev. A **38**, 3098 (1988).

[76] T. Van Voorhis and G. E. Scuseria, *A novel form for the exchange-correlation energy functional*, J. Chem. Phys. **109**, 400 (1998).

[77] J. P. Perdew, S. Kurth, A. Zupan, and P. Blaha, *Accurate Density Functional with Correct Formal Properties: A Step Beyond the Generalized Gradient Approximation*, Phys. Rev. Lett. **82**, 2544 (1999).

[78] A. D. Becke, *Density-functional thermochemistry. III. The role of exact exchange*, J. Chem. Phys. **98**, 5648 (1993).

[79] C. Lee, W. Yang, and R. G. Parr, *Development of the Colle-Salvetti correlation-energy formula into a functional of the electron density*, Phys. Rev. B **37**, 785 (1988).

[80] C. Adamo and V. Barone, *Toward reliable density functional methods without adjustable parameters: The PBE0 model*, J. Chem. Phys. **110**, 6158 (1999).

[81] S. Kümmel and L. Kronik, *Orbital-dependent density functionals: Theory and applications*, Rev. Mod. Phys. **80**, 3 (2008).

[82] P. E. Lammert, *Differentiability of Lieb functional in electronic density functional theory*, Int. J. Quantum Chem. **107**, 1943 (2007).

[83] M. Penz, A. Laestadius, E. I. Tellgren, and M. Ruggenthaler, *Guaranteed convergence of a regularized Kohn-Sham iteration in finite dimensions*, arXiv:1903.09579 (2019).

[84] P. Cortona, *Self-consistently determined properties of solids without band-structure calculations*, Phys. Rev. B **44**, 8454 (1991).

[85] P. Fulde, *Electron correlations in molecules and solids*, Vol. 100, Springer, Berlin, Heidelberg (1993), ISBN: 978-3-642-57809-0.

[86] F. R. Manby, M. Stella, J. D. Goodpaster, and T. F. Miller III, *A simple, exact density-functional-theory embedding scheme*, J. Chem. Theory Comput. **8**, 2564 (2012).

[87] C. R. Jacob and J. Neugebauer, *Subsystem density-functional theory*, Wiley Interdiscip. Rev. Comput. Mol. Sci. **4**, 325 (2014).

[88] U. Mordovina, T. E. Reinhard, I. Theophilou, H. Appel, and A. Rubio, *Self-Consistent Density-Functional Embedding: a Novel Approach for Density-Functional Approximations*, J. Chem. Theory Comput. **15**, 5209 (2019).

[89] I. Theophilou, T. E. Reinhard, M. Ruggenthaler, and A. Rubio, *Foundations of Density Matrix Embedding Theory revisited: a Density Matrix Functional perspective*, in preparation .

[90] I. W. Bulik, W. Chen, and G. E. Scuseria, *Electron correlation in solids via density embedding theory*, J. Chem. Phys. **141**, 054113 (2014).

[91] T. E. Reinhard, *Density Matrix Embedding Theory: Foundations, Applications and Connection to Functional Theories*, Ph.D. thesis, Universtät Hamburg (2019).

[92] T. E. Reinhard, U. Mordovina, C. Hubig, J. S. Kretchmer, U. Schollwöck, H. Appel, M. A. Sentef, and A. Rubio, *Density-Matrix Embedding Theory Study of the One-Dimensional Hubbard–Holstein Model*, J. Chem. Theory Comput. **15**, 2221 (2019).

[93] M. Welborn, T. Tsuchimochi, and T. Van Voorhis, *Bootstrap embedding: An internally consistent fragment-based method*, J. Chem. Phys. **145**, 074102 (2016).

[94] M. E. Peskin, *An introduction to quantum field theory*, Avalon Publishing (1995) ISBN: 978-0-201-50397-5.

[95] R. P. Feynman, *QED: The strange theory of light and matter*, Princeton University Press (2006), ISBN: 978-0-691-12575-6.

[96] D. P. Craig and T. Thirunamachandran, *Molecular quantum electrodynamics: an introduction to radiation-molecule interactions*, Dover Publications Inc. (1998), ISBN: 978-0-486-40214-7.

[97] H. Spohn, *Dynamics of charged particles and their radiation field*, Cambridge University Press (2004), ISBN: 978-0-521-03707-5.

[98] J. D. Jackson, *Classical electrodynamics*, 3rd ed., Wiley (1998), ISBN: 978-0-471-30932-1.

[99] G. B. Arfken and H. J. Weber, *Mathematical Methods for Physicists, 4th ed.* Am. J. Phys **67**, 165 (1999).

[100] C. Gerry, P. Knight, and P. L. Knight, *Introductory quantum optics*, Cambridge University Press (2005), ISBN: 978-0-521-52735-4.

[101] J. Baez and J. P. Muniain, *Gauge fields, knots and gravity*, Vol. 4, World Scientific Publishing Company (1994), ISBN: 978-9-810-22034-1.

[102] C. Schäfer, M. Ruggenthaler, V. Rokaj, and A. Rubio, *Relevance of the quadratic diamagnetic and self-polarization terms in cavity quantum electrodynamics*, arXiv:1911.08427 (2019).

[103] R. G. Woolley, *Gauge invariant wave mechanics and the Power-Zienau-Woolley transformation*, J. Phys. A **13**, 2795 (1980).

[104] M. Babiker and R. Loudon, *Derivation of the Power-Zienau-Woolley Hamiltonian in quantum electrodynamics by gauge transformation*, Proc. Royal Soc. Lond. A **385**, 439 (1983).

[105] V. Rokaj, D. M. Welakuh, M. Ruggenthaler, and A. Rubio, *Light–matter interaction in the long-wavelength limit: no ground-state without dipole self-energy*, J. Phys. B **51**, 034005 (2018).

[106] F. H. Faisal, *Theory of multiphoton processes*, Plenum Press (1987), ISBN: 0-306-42317-0.

[107] A. Vukics, T. Grießer, and P. Domokos, *Elimination of the a-square problem from cavity QED*, Phys. Rev. Lett. **112**, 073601 (2014).

[108] M. Ruggenthaler, M. Penz, and R. van Leeuwen, *Existence, uniqueness, and construction of the density-potential mapping in time-dependent density-functional theory*, J. Phys.: Condens. Matter **27**, 203202 (2015).

[109] O. V. Gritsenko, R. van Leeuwen, and E. J. Baerends, *Molecular Kohn-Sham exchange-correlation potential from the correlated ab initio electron density*, Phys. Rev. A **52**, 1870 (1995).

[110] A. A. Kananenka, S. V. Kohut, A. P. Gaiduk, I. G. Ryabinkin, and V. N. Staroverov, *Efficient construction of exchange and correlation potentials by inverting the Kohn–Sham equations*, J. Chem. Phys. **139**, 074112 (2013).

[111] D. S. Jensen and A. Wasserman, *Numerical methods for the inverse problem of density functional theory*, Int. J. Quantum Chem. **118**, e25425 (2017).

[112] S. E. B. Nielsen, M. Ruggenthaler, and R. van Leeuwen, *Numerical construction of the density-potential mapping*, Eur. Phys. J. B **91**, 235 (2018).

[113] B. Kanungo, P. M. Zimmerman, and V. Gavini, *Exact exchange-correlation potentials from ground-state electron densities*, Nat. Commun. **10**, 1 (2019).

[114] P. Elliott, K. Burke, M. H. Cohen, and A. Wasserman, *Partition density-functional theory*, Phys. Rev. A **82**, 024501 (2010).

[115] J. Nafziger and A. Wasserman, *Density-based partitioning methods for ground-state molecular calculations*, J. Phys. Chem. A **118**, 7623 (2014).

[116] X. Wu, Z.-H. Cui, Y. Tong, M. Lindsey, G. K.-L. Chan, and L. Lin, *Projected density matrix embedding theory with applications to the two-dimensional Hubbard model*, J. Chem. Phys. **151**, 064108 (2019).

[117] H.-Z. Ye, N. D. Ricke, H. K. Tran, and T. Van Voorhis, *Bootstrap Embedding for Molecules*, J. Chem. Theory Comput. **15**, 4497 (2019).

[118] J. MacDonald, *Successive approximations by the Rayleigh-Ritz variation method*, Phys. Rev. **43**, 830 (1933).

[119] N. Helbig, I. V. Tokatly, and A. Rubio, *Exact Kohn-Sham potential of strongly correlated finite systems*, J. Chem. Phys. **131**, 224105 (2009).

[120] I. W. Bulik, G. E. Scuseria, and J. Dukelsky, *Density matrix embedding from broken symmetry lattice mean fields*, Phys. Rev. B **89** (2014).

[121] H. Prautzsch, W. Boehm, and M. Paluszny, *Bézier and B-spline techniques*, Springer, Berlin, Heidelberg (2002), ISBN: 978-3-662-04919-8.

[122] L. O. Wagner, E. Stoudenmire, K. Burke, and S. R. White, *Reference electronic structure calculations in one dimension*, Phys. Chem. Chem. Phys. **14**, 8581 (2012).

[123] T. Kato, *On the eigenfunctions of many-particle systems in quantum mechanics*, Comm. Pure Appl. Math. **10**, 151 (1957).

[124] A. Gordon, R. Santra, and F. X. Kärtner, *Role of the Coulomb singularity in high-order harmonic generation*, Phys. Rev. A **72**, 063411 (2005).

[125] A. J. Cohen, P. Mori-Sánchez, and W. Yang, *Insights into current limitations of density functional theory*, Science **321**, 792 (2008).

[126] S. Vuckovic, L. O. Wagner, A. Mirtschink, and P. Gori-Giorgi, *Hydrogen Molecule Dissociation Curve with Functionals Based on the Strictly Correlated Regime*, J. Chem. Theory Comput. **11**, 3153 (2015).

[127] A. Heßelmann and A. Görling, *Correct Description of the Bond Dissociation Limit without Breaking Spin Symmetry by a Random-Phase-Approximation Correlation Functional*, Phys. Rev. Lett. **106** (2011).

[128] M. Fuchs, Y.-M. Niquet, X. Gonze, and K. Burke, *Describing static correlation in bond dissociation by Kohn–Sham density functional theory*, J. Chem. Phys. **122**, 094116 (2005).

[129] M. Hellgren, F. Caruso, D. R. Rohr, X. Ren, A. Rubio, M. Scheffler, and P. Rinke, *Static correlation and electron localization in molecular dimers from the self-consistent RPA and GW approximation*, Phys. Rev. B **91**, 165110 (2015).

[130] R. van Leeuwen and E. J. Baerends, *Exchange-correlation potential with correct asymptotic behavior*, Phys. Rev. A **49**, 2421 (1994).

[131] N. Helbig, J. I. Fuks, M. Casula, M. J. Verstraete, M. A. L. Marques, I. V. Tokatly, and A. Rubio, *Density functional theory beyond the linear regime: Validating an adiabatic local density approximation*, Phys. Rev. A **83** (2011).

[132] P. Elliott, J. I. Fuks, A. Rubio, and N. T. Maitra, *Universal dynamical steps in the exact time-dependent exchange-correlation potential*, Phys. Rev. Lett. **109**, 266404 (2012).

[133] K. Luo, P. Elliott, and N. T. Maitra, *Absence of dynamical steps in the exact correlation potential in the linear response regime*, Phys. Rev. A **88**, 042508 (2013).

[134] M. Hodgson, J. Ramsden, and R. Godby, *Origin of static and dynamic steps in exact Kohn-Sham potentials*, Phys. Rev. B **93**, 155146 (2016).

[135] M. J. Hodgson, E. Kraisler, A. Schild, and E. K. Gross, *How interatomic steps in the exact Kohn–Sham potential relate to derivative discontinuities of the energy*, J. Phys. Chem. Lett. **8**, 5974 (2017).

[136] K. Schonhammer and O. Gunnarsson, *Discontinuity of the exchange-correlation potential in density functional theory*, J. Phys. C: Solid State Phys. **20**, 3675 (1987).

[137] M. Hellgren and T. Gould, *Strong Correlation and Charge Localization in Kohn-Sham Theories with Fractional Orbital Occupations: The Role of the Potential*, chemrxiv.8141912.v1 (2019).

[138] M. Capone, L. de' Medici, and A. Georges, *Solving the dynamical mean-field theory at very low temperatures using the Lanczos exact diagonalization*, Phys. Rev. B **76**, 245116 (2007).

[139] F. A. Wolf, A. Go, I. P. McCulloch, A. J. Millis, and U. Schollwöck, *Imaginary-time matrix product state impurity solver for dynamical mean-field theory*, Phys. Rev. X **5**, 041032 (2015).

[140] C. Hubig, *Symmetry-protected tensor networks*, Ph.D. thesis, Ludwig-Maximilians-Universität München (2017).

[141] H.-J. Werner, P. J. Knowles, G. Knizia, F. R. Manby, and M. Schütz, *Molpro: a general-purpose quantum chemistry program package*, Wiley Interdiscip. Rev. Comput. Mol. Sci. **2**, 242 (2012).

[142] Q. Sun, T. C. Berkelbach, N. S. Blunt, G. H. Booth, S. Guo, Z. Li, J. Liu, J. D. McClain, E. R. Sayfutyarova, S. Sharma, S. Wouters, and G. K.-L. Chan, *PySCF: the Python-based simulations of chemistry framework*, Wiley Interdiscip. Rev. Comput. Mol. Sci. **8**, e1340 (2018) .

[143] V. Khoromskaia and B. N. Khoromskij, *Tensor numerical methods in quantum chemistry: from Hartree–Fock to excitation energies*, Phys. Chem. Chem. Phys. **17**, 31491 (2015).

[144] Griebel, Michael and Hamaekers, Jan, *Sparse grids for the Schrödinger equation*, ESAIM: M2AN **41**, 215 (2007).

[145] X. Andrade, D. Strubbe, U. De Giovannini, A. H. Larsen, M. J. T. Oliveira, J. Alberdi-Rodriguez, A. Varas, I. Theophilou, N. Helbig, M. J. Verstraete, L. Stella, F. Nogueira, A. Aspuru-Guzik, A. Castro, M. A. L. Marques, and A. Rubio, *Real-space grids and the Octopus code as tools for the development of new simulation approaches for electronic systems*, Phys. Chem. Chem. Phys. **17**, 31371 (2015).

[146] P. Parkkinen, S. A. Losilla, E. Solala, E. A. Toivanen, W.-H. Xu, and D. Sundholm, *A Generalized Grid-Based Fast Multipole Method for Integrating Helmholtz Kernels*, J. Chem. Theory Comput. **13**, 654 (2017).

[147] U. Mordovina, C. Bungey, H. Appel, P. J. Knowles, A. Rubio, and F. R. Manby, *Polaritonic Coupled-Cluster Theory*, arXiv:1909.02401 (2019).

[148] T. Philbin, *Generalized coherent states*, Am. J. Phys. **82**, 742 (2014).

[149] P. Jordan and E. P. Wigner, *Über das paulische Äquivalenzverbot*, in *The Collected Works of Eugene Paul Wigner*, Springer (1993), ISBN: 978-3-662-07791-7.

[150] T. Oliphant, *NumPy: A guide to NumPy*, USA: Trelgol Publishing (2006–), [Online; accessed 11/7/2019].

[151] T. Helgaker, P. Jørgensen, and J. Olsen, *Molecular electronic-structure theory*, John Wiley & Sons (2014), ISBN: 978-1-119-01955-8.

[152] A. Köhn and A. Tajti, *Can coupled-cluster theory treat conical intersections?* J. Chem. Phys. **127**, 044105 (2007).

[153] E. F. Kjønstad and H. Koch, *An orbital invariant similarity constrained coupled cluster model*, J. Chem. Theory Comput. **15**, 5386 (2019).

[154] T. Dimitrov, J. Flick, M. Ruggenthaler, and A. Rubio, *Exact functionals for correlated electron-photon systems*, New J. Phys. **19**, 113036 (2017).

[155] J. Flick, N. Rivera, and P. Narang, *Strong light-matter coupling in quantum chemistry and quantum photonics*, Nanophotonics **7**, 1479 (2018).

[156] E. T. Jaynes and F. W. Cummings, *Comparison of quantum and semiclassical radiation theories with application to the beam maser*, Proc. IEEE **51**, 89 (1963).

[157] J. Flick, C. Schäfer, M. Ruggenthaler, H. Appel, and A. Rubio, *Ab Initio Optimized Effective Potentials for Real Molecules in Optical Cavities: Photon Contributions to the Molecular Ground State*, ACS Photonics **5**, 992 (2018).

[158] C. Schäfer, M. Ruggenthaler, and A. Rubio, *Ab initio nonrelativistic quantum electrodynamics: Bridging quantum chemistry and quantum optics from weak to strong coupling*, Phys. Rev. A **98**, 043801 (2018).

[159] T. N. Rescigno and V. McKoy, *Rigorous method for computing photoabsorption cross sections from a basis-set expansion*, Phys. Rev. A **12**, 522 (1975).

[160] G. Vignale, *Current Density Functional Theory*, in: *Time-Dependent Density Functional Theory*, Springer, Berlin, Heidelberg (2006), ISBN: 978-3-540-35426-0.

[161] C. Pellegrini, J. Flick, I. V. Tokatly, H. Appel, and A. Rubio, *Optimized effective potential for quantum electrodynamical time-dependent density functional theory*, Phys. Rev. Lett. **115**, 093001 (2015).

[162] J. Flick, M. Ruggenthaler, H. Appel, and A. Rubio, *Kohn–Sham approach to quantum electrodynamical density-functional theory: Exact time-dependent effective potentials in real space*, Proc. Natl. Acad. Sci. USA **112**, 15285 (2015).

[163] C. Riplinger and F. Neese, *An efficient and near linear scaling pair natural orbital based local coupled cluster method*, J. Chem. Phys. **138**, 034106 (2013).

[164] E. Orgiu, J. George, J. Hutchison, E. Devaux, J. Dayen, B. Doudin, F. Stellacci, C. Genet, J. Schachenmayer, C. Genes, *et al.*, *Conductivity in organic semiconductors hybridized with the vacuum field*, Nat. Mater. **14**, 1123 (2015).

[165] A. Shalabney, J. George, J. a. Hutchison, G. Pupillo, C. Genet, and T. W. Ebbesen, *Coherent coupling of molecular resonators with a microcavity mode*, Nat. Commun. **6**, 5981 (2015).

[166] J. T. Chayes, L. Chayes, and M. B. Ruskai, *Density functional approach to quantum lattice systems*, J. Stat. Phys. **38**, 497 (1985).

[167] W. Andreoni and S. Yip, *Handbook of Materials Modeling: Methods: Theory and Modeling*, Springer, Cham (2018), ISBN: 978-3-319-42913-7.

Acknowledgments

I would like to thank Angel Rubio for giving me the great opportunity to work as part of his research team in an excellent scientific environment, for giving me the freedom to pursue my research ideas, and for his valuable council.

I am grateful to Heiko Appel for being my supervisor, for sharing his ideas, and for his encouragement.

I also wish to thank to Daniela Pfannkuche for evaluating this thesis, for taking interest in my research, and for her patience.

Thanks to the whole MPSD theory group for creating a nice and productive working atmosphere as well as the non-scientific staff of the MPSD and CFEL for all their support.

During my time at the University of Bristol I had the pleasure to work on the exciting coupled-cluster project with Fred Manby, whom I would like to thank for sharing his expertise on quantum chemistry and coding. A big thank you goes out also to his group for all the coffee breaks and tea times that made me feel very welcome.

A special gratitude goes to Iris Theophilou for her intensive support during my last research year, for the help in refining the embedding ideas and in improving the SDE paper, and for guiding me to the finish line.

I am deeply grateful to Michael Ruggenthaler for always having my back and, especially, for always showing me the positive side of things, not to mention all the times I profited from his valuable QED expertise and his exceptional phrasing talent.

I am greatly indebted to Teresa Reinhard for being my scientific partner in crime, for the roller coaster of desperate and enlightening moments during our discussions, for all the wine we drank during our kitchen-philosophy sessions, and for all the help she manages to provide even while being hundreds of kilometers away.

A big thank you goes out to Christian Schäfer for the scientific discussions, for always making the right comment, for great time spent in our office, and for the even greater time spent together outside.

Thanks to Alexandra Göbel for the final touches to my thesis, for always offering sweets and for the vital breaks that helped me getting my mind off work.

In this spirit, I would also like to thank Florian Buchholz, Lars-Hendrik Frahm, and Christian Schäfer for the great time we spent together organizing the ETSF YRM 2018.

I consider myself extremely fortunate to be surrounded by love, understanding and support from all my family and friends, for which I am deeply grateful.

Finally, my gratitude goes to Yusuf Mohammed for helping me get through the difficult times, for his scientific advice, for his constant encouragement – simply for being the best partner I could ever wish for.

Eidesstattliche Versicherung

Hiermit versichere ich an Eides statt, die vorliegende Dissertationsschrift selbst verfasst und keine anderen als die angegebenen Hilfsmittel und Quellen benutzt zu haben.

Die eingereichte schriftliche Fassung entspricht der auf dem elektronischen Speichermedium.

Die Dissertation wurde in der vorgelegten oder einer ähnlichen Form nicht schon einmal in einem früheren Promotionsverfahren angenommen oder als ungenügend beurteilt.

Hamburg, den 10.01.2020

Uliana Mordovina